MECHANICAL AND TRIBOLOGICAL PROPERTIES OF CARBON NANOFIBER REINFORCED HIGH DENSITY POLYETHYLENE

A Dissertation
Submitted to the Graduate Faculty
of the
North Dakota State University
of Agriculture and Applied Science

By

Songbo Xu

In Partial Fulfillment
for the Degree of
DOCTOR OF PHILOSOPHY

Major Department:
Mechanical Engineering

July 2014

Fargo, North Dakota

North Dakota State University
Graduate School

Title

Mechanical and Tribological Properties of Carbon Nanofiber Reinforced High Density Polyethylene

By

Songbo Xu

The Supervisory Committee certifies that this ***disquisition*** complies with North Dakota State University's regulations and meets the accepted standards for the degree of

DOCTOR OF PHILOSOPHY

SUPERVISORY COMMITTEE:

Dr. Xiangqing Tangpong
Chair

Dr. Iskander Akhatov

Dr. Chad Ulven

Dr. Xinnan Wang

Dr. Andriy Voronov

Approved:

7/10/2014
Date

Dr. Alan Kallmeyer
Department Chair

ABSTRACT

High density polyethylene (HDPE) is widely used as a bearing material in industrial application because of its low friction and high wear resistance. Reinforcing polymers with the appropriate nanofillers is an effective way to obtain a variety of enhanced material properties. Carbon nanofibers (CNFs) with silane coatings (two thicknesses: 2.8 nm and 46 nm) were added into high density polyethylene (HDPE) to improve the tribological properties of the nanocomposite material. The goal of the present study is to investigate how the mechanical, thermal, and wear behavior of HDPE can be altered by the addition of either pristine or silane treated CNFs at different loading levels (0.5 wt.%, 1 wt.%, and 3 wt.%) and to model the wear of the HDPE/CNF nanocomposites under both dry and lubricated conditions.

In this study, the wear and friction tests are performed on a pin-on-disc tribometer under dry, bovine serum, and phosphate buffered saline lubricated conditions. The thermal, mechanical, properties, and biocompatibility of HDPE/CNF nanocomposites are characterized and compared with those of the neat HDPE. The correlations of the wear and factors such as work of fracture, thermal conductivity, and friction force are explored. An energy-based wear model is proposed for the dry sliding condition in which a thermal analysis is derived to trace the friction energy loss in the wear process. A wear model for the lubricated condition is developed with incorporation of elastohydrodynamic lubrication theory and Reye's wear model to predict the long term wear.

ACKNOWLEDGMENTS

I would like to thank my advisor, Dr. Tangpong, one of the most important people in my life, for supporting me during the past four years. She gave me the opportunity to work at North Dakota State University. She has been a constant source of guidance, support and encouragement both in my professional and personal lives. She also has trained me valuable skills for mechanical research, paper and grant writing, and conference presentation, all of which make for a recipe of success in my area of specialization. Words are inadequate to express my heartfelt thanks.

I would also like to express my great gratitude to my co-advisor, Dr. Akhatov. I especially appreciate the in-depth explanation of fundamental principles and insightful discussions about the research. In addition, I also would like to thank the other members of my Ph.D. committee, Dr. Voronov, Dr. Ulven, and Dr. Wang, for their assistance, guidance, and time contributions to my dissertation.

I am also thankful to Aydar Akchurin and Ihor Tarnavchyk, who worked with me closely, for their helping, giving, and sharing in our research team. I would also like to thank Shannon Viestenz, the mechanic staff in Department of Mechanical Engineering, for the very friendly lab and equipment help. I also thank my friends in both America and China for providing the support, encouragement and friendship that I needed.

DEDICATION

I dedicate this dissertation to my family:

to my wife, Ting, for her constant love, understanding, and support;

to my sons, Allen and Aydar, for the fun time playing with them and their encouragement for me to work harder;

to my loving parents, Chunsheng Xu and Caixia Li, who have sacrificed their lives a lot for me and provided unconditional love and support;

to my grandma for her encouragement and care.

I love you all dearly.

TABLE OF CONTENTS

LIST OF TABLES

LIST OF FIGURES

LIST OF ABBREVIATIONS

BS……Bovine Serum

CNF…….Carbon Nanofiber

CNT…….Carbon Nanotube

COF…….Coefficient of Friction

EHL…….Elastohydrodynamic lubrication

GNP…….Graphite nanoparticles

HA……...Hyaluronic acid

HDPE……..High Density Polyethylene

LDPE……...Low Density Polyethylene

MMT……...Montmorillonite

MWCNT…….Multi-Walled Carbon Nanotube

PE……Polyethylene

PMMA……Poly(methyl methacrylate)

PP……Polypropylene

PS……Polystyrene

PTFE…….. Polytetrafluoroethylene

SEE…….Standard errors of estimate

SEM……Scanning electron microscope

SPSS……...Statistical package for the social sciences

SWR…….. Specific wear rate

UHMWPE……..Ultra High Molecular Weight Polyethylene

LIST OF APPENDIX FIGURES

CHAPTER 1. BACKGROUND AND OBJECTIVES

Tribology refers to the science and technology of friction, lubrication, and wear. Tribological performance related to the reliability, accuracy, and precision, and therefore, it affects the efficiency and life of all mechanical systems. Friction is an important resource for energy loss in industry, mining, and agriculture. It has been estimated that more than a quarter of the energy loss can be prevented by tribological technology improvement [1]. Wear sometimes is inevitable due to the nature of friction. Wear of automotive and industrial machines, air jet engine, rail, road, etc. all requires vast investment for repair and replacement. Therefore, to decrease these negative effects of friction and wear, tribological studies are becoming more and more important in modern civilization.

The research and applications of polymer in tribology can be traced back to hundreds of years ago when rubbers and elastomers were used as important engineering materials in modern automotive industry. Nowadays, polymer such as high density polyethylene (HDPE), ultra high molecular weight polyethylene (UHMWPE) and their composites are increasingly applied in some tribological applications such as low speed gears and bearing, seals, and artificial joints due to their low cost, easy manufacturability, superior self-lubrication, and excellent corrosion resistance and lower density [2]. To further reduce wear, efforts have been made through the incorporation of glass fibers [3], carbon fibers [4], and even nano-reinforcements such as carbon nanotubes (CNTs) [2] and carbon nanofibers (CNFs) [5, 6] into these polymers. In particular, this research is focused on understanding the tribological behavior of CNF reinforced HDPE nanocomposites. As the tribological behavior of polymers depend on many factors such as mechanical properties, thermal properties, and lubrication conditions, the effects of these factors on the wear of HDPE/CNF nanocomposites are investigated both experimentally and theoretically in this dissertation.

1.1. Tribological studies of materials

1.1.1. Friction

If two solid bodies in contact are made to slide relative to one another, there is always a force resisting the sliding motion called friction. Friction phenomena are desirable in some instances, for example, soles of shoes, brakes operation, and self-locking joints. However, in many other cases, we try to decrease the friction due to energy consumption, although it can never be eliminated entirely.

The well-accepted laws of friction (under dry condition) can be summarized as follows [7]:

- *Amonton's first law*: Friction force is proportional to the normal load;
- *Amonton's second law*: Friction force is independent of the apparent area of contact.

A third law that "kinetic friction is nearly independent of the sliding speed" proposed by Coulomb [8] is known to be invalid [1]. Most modern theories consider that friction force in metals' contact results from three sources [1]: (1) the force necessary to shear adhesive joint between the real contacted asperities; (2) the deformation force due to the asperities of the harder metal ploughing through the asperities of the softer one; and (3) asperity deformation, which is mainly related to the static coefficient of friction.

The common measure of friction is the coefficient of friction (COF), which is often symbolized as a dimensionless scalar, μ, and is defined as the ratio of the force of friction between two bodies and the normal force pressing them together. Therefore, COF is greater than zero and less than one. The coefficient of friction is dependent on the materials used; for example, ice skates on ice has a low COF, while rubber tire on pavement has a high COF. Generally, two types of COF are quoted: the coefficient of static friction, which applies to surfaces at rest relative to each other, and the coefficient of kinetic friction, which applies to

surfaces in relative motion. In most cases, the value of former is higher than the latter. As friction is a result of stochastic interaction between the contact asperities, the friction force in all friction tests is not very stable in nature and the COF is often taken as an average value through the entire friction test.

Friction energy, defined as the work done by friction force, is expressed as:

$$\Delta E = \int_0^L F(x)dx = NV\int_0^t \mu(t)\,dt \approx \bar{F}L \approx NV\bar{\mu}t \tag{1.1}$$

where L is the sliding distance, F is friction force, N is the normal load, and V is constant speed, t is the time, and μ is the coefficient of friction. $\bar{F}$ and $\bar{\mu}$ are the average friction force and coefficient of friction, respectively. Based on the law of conservation of energy, energy is not destroyed or stored due to friction. Therefore, friction energy needs to be transformed into other forms. Ramalho [9] concluded that the friction energy in the sliding contact can be dissipated mainly through three processes: heat generation, wear particle generation, and other entropy changes associated with material transformation at the interface. Figure 1.1 further illustrates that the amount of heat generated was reported to be around 80-90% of the work done by the friction force when a titanium part slid on a steel part [9]. It looks feasible to set up thermal analysis to calculate the heat generation energy from given friction energy input, once the geometry and thermal characteristics of the sliding body are known. Assuming the friction energy is only dissipated into wear and heat, it is possible to define wear damage in terms of energy consumption by subtracting the energy going into heat generation from the total friction energy. This idea will be fully developed in Chapter 5.

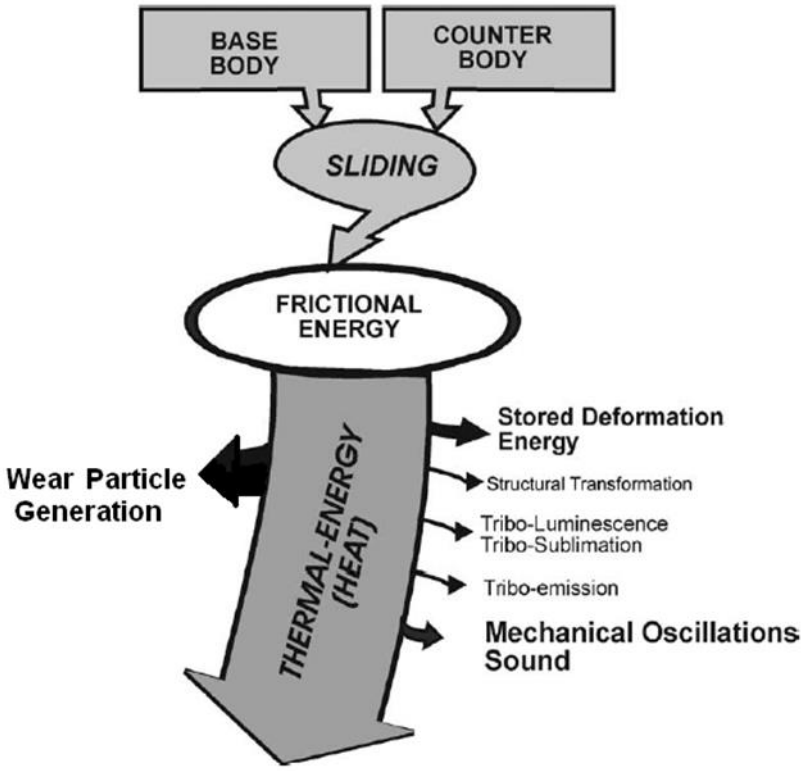

Figure 1.1: Friction energy dissipation mechanisms (reprinted with permission from Ref. [9]).

1.1.2. Lubrication

Lubrication is the process, or technique used to reduce/prevent wear and lower friction. As mentioned in Section 1.1.1., the classic laws of friction only give a basic understanding of non-lubricated contacts. However, many mechanical systems in engineering application are under lubricated conditions. The behavior of sliding surfaces is strongly modified with the involvement of a lubricant between them. The Stribeck curve is used to categorize the friction properties of two lubricated surfaces and define different lubrication regimes, as shown in Figure 1.2.

We can find that at large Stribeck number, the COF is low and proportionally increases with the increase of the Stribeck number. This regime is referred to as thick film lubrication (also called as elastohydrodynamic lubrication) in which the surfaces are completely separated

by the pressure buildup in the lubricant. This type of lubrication has small COF and strongly depends on viscosity of lubricatant. Upon decrease of the Stribeck number, COF obtains a minimum value. The range around the minimum point is the mixed-lubrication regime. In this regime, both asperity contact and the lubricant support the contact load. The COF now depends on the surface roughness, material properties of the surfaces, and the material properties of the lubricant. For even smaller values of the Stribeck number, the COF increases rapidly, because the lubricant film is negligible and the contact load is transmitted mainly by mechanical contact between the asperities. This regime is called boundary lubrication. However, in practice, it is hard to identify the lubrication mechanism by experiments and the fundamental understanding on the relationship between lubrication and wear is not fully known.

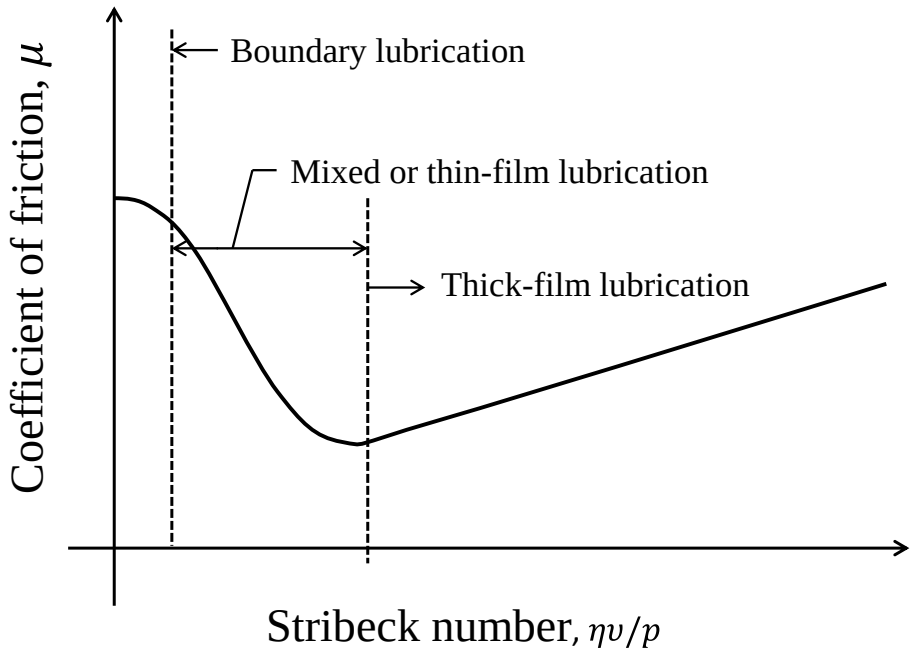

Figure 1.2: Schematic diagram of Stribeck curve for lubrication regimes; η is viscosity of lubricant, v is sliding speed, and p is pressure.

1.1.3. Wear

Wear is the material loss from a solid surface as associated with sliding against another material [10]. Wear is almost inevitable when two solid surfaces in contact slide against each other. Wear is very complex and largely empirical depending on the material properties of the contact surface, the environment, the running condition, etc. The wear rate of a material is conventionally defined as the volume or mass lost from the material per unit of sliding distance.

Wear depends on many factors generally including COF, normal load, sliding distance, and material properties like hardness, toughness, ultimate strength and strain. The roughness indirectly affecting the COF and pressure distribution is also an important factor. For the lubricated condition, the friction properties (COF) of two surfaces are strongly dependent on the Stribeck number (Figure 1.2), which refers to viscosity of lubricate, sliding velocity, and the pressure that lubricant supports. Thus, these parameters also affect the wear of the material under lubricated conditions. In addition, wear is also dependent on the tribological system. To characterize the wear loss of materials, many testers have been used including the pin-on-disk, cylinder-on-plane, as well as ball-on-prism testers. Therefore, to compare wear resistance of a material, the type of wear test and test conditions like ambient temperature need to be specified. For some specific case, the wear is also influenced by the corrosive effect and the participation of the erosion particles.

With the application of polymers for tribological applications increasing, much research has been carried out on the tribology of polymers and their application in various industries [11]. Most polymers exhibit lower COF at high normal load than metals in unlubricated condition [12]. When a polymer is sliding on metal, almost all the deformation is elastic without plastic flow. For a given roughness, the plastic index for polymers is an order lower compared to metals. Therefore, the low friction of polymers may potentially decrease due to less plastic deformation of polymer which is considered as one of the friction resource.

Polymers generally have lower thermal conductivities and melting points than traditional metallic bearing materials such as tool steel. Therefore, when it is applied to high speed component, the surface layers may melt. However, when it is applied in low speed component, like low speed gear, it will exhibit excellent wear resistance. The low wear rate of polymers may also result from the formation of polymeric wear debris transfer film [13]. When dry sliding begins, some debris of polymers is torn from the polymer's surface by local shear stresses. If some of them are not removed effectively, they will become attached to the substrate due to the high normal stress in interface of sliding motion, and then a polymeric wear debris transfer film forms at the interface of the two rubbing solid bodies. Another important feature of polymer is that most polymers have viscoelastic property. The friction properties at the initial stage and after the formation of a transfer film between contact areas are believed to be strongly associated with the viscoelasticity of polymer [11].

In the polymer family, semicrystalline polymers, for example, polytetrafluoroethylene (PTFE), nylons, and polyethylene including HDPE and UHMWPE, have been very extensively studied on their wear properties due to their wide tribological application. PTFE is a good choice for bearings and compressor piston seals [14]. Nylon is used commonly in automobile bearing and polyvinylidenefluoride in electrical shielding[15]. The HDPE and UHMWPE, in particular, are considered to be very popular in automobile industry and orthopedic replacement, which will be further introduced in the next section.

1.2. Polyethylene

1.2.1. Polyethylene structure

Polyethylene is the most common plastic consisting of linear chains with repeat unit "-CH_2-". Based on its molecular weight, density, and degree of branching, polyethylene is classified into several different categories, the most important polyethylene grades are HDPE,

low density polyethylene (LDPE) and UHMWPE. HDPE is defined by a density range of 0.93–0.97 g/cm^3, while density of LDPE ranges from 0.91–0.94 g/cm^3. The difference in high-density polyethylene and low-density polyethylene is mainly from their degrees of branching. Figure 1.3 contains schematics depicting the structures of HDPE and LDPE.

(a) A macromolecular of HDPE (linear polyethylene)

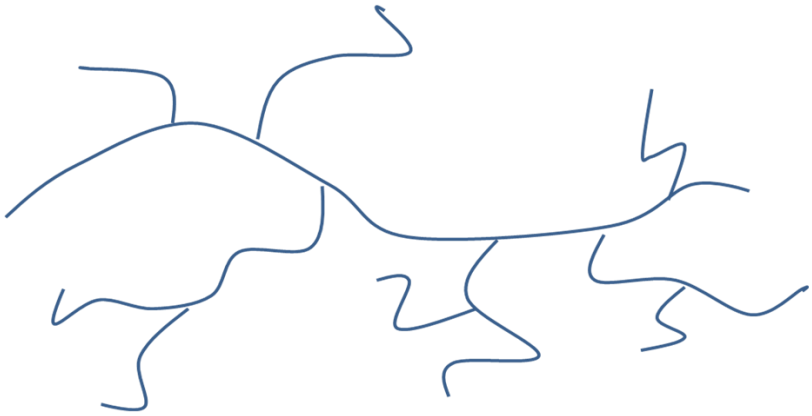

(b) A macromolecular of LDPE (branched polyethylene)

Figure 1.3: Idealized schematic of polyethylene macromoleculares: (a) high density polyethylene; (b) low density polyethylene.

HDPE consists of long, linear chains of polymerized ethylene and has higher tensile strength than LDPE. The improvement of strength exceeds the difference in density, giving HDPE a higher specific strength compared to LDPE. The lack of chiral centers and the linearity of the chain make HDPE easily and rapidly form a highly crystalline structure when below the melting point.

UHMWPE is defined as a PE that has a molecular weight greater than 3.1 million g/mol. The molecular weight of HDPE ranges between 30,000 and 200,000 g/mol. UHMWPE has the same chemical structure as HDPE, differing primarily in molecular weight. UHMWPE

molecules typically have 100,000 to 250,000 monomer units per molecule each compared to HDPE's 700 to 1,800 monomers. Although the molecular structure of linear polyethylene is simple, polyethylene as a semicrystalline polymer consists of crystalline phases and amorphous domains. It is reported that the high degree of crystallinity of UHMWEP is associated with the high modulus and yield stress [5].

1.2.2. Properties of polyethylene

The properties of polyethylene have a wide range due to the differences in the length of polymer chains, degree of branching, degree of crystallinity and polydispersity. The selected material properties of polyethylene materials are listed in Table 1.1.

LDPE is relatively flexible compared to HDPE and UHMWPE, which makes it a good choice for prosthetic devices. It is used for impact pads due to its good impact resistance. Due to its low viscosity, it is easy to process, making it widely used where chemical and corrosion resistance is in demand. Other advantages of LDPE include: light weight, easy to clean, very low moisture absorption, and satisfying food handing guidelines. It is also frequently used in packaging, bags, bottles, and liners.

HDPE has relatively higher tensile strength and wear resistance compared to LDPE, representing the largest portion of the polyethylene applications. HDPE also offers excellent impact resistance, light weight, no moisture absorption, non-toxic and non-staining. It also meets the requirements for food processing. As a thermoplastic, HDPE is commonly recycled. Due to its recycling properties, HDPE is being processed by recyclebots into filament for 3-D printers [16].

Table 1.1: Selected material properties of PE materials.

Property	**LDPE** [17]	**HDPE** [18, 19]	**UHMWPE** [18, 19]	**Test method ASTM**
Physical				
Density (g/cm^3)	0.910–0.940	0.952-0.965	0.926-0.945	D792
Water Absorption (%)	< 0.01	0	0	D570
Degree of Crystallinity (%)	35-55	60-80	39-75	DSC
Mechanical				
Tensile Modulus (Gpa)	0.28	0.4-1.0	0.58-1.6	D638
Tensile Yield Strength (Mpa)	9.4	26-33	21-28	D638
Tensile Ultimate Strength (Mpa)	13.4	22-31	39-48	D638
Tensile Ultimate Elongation (%)	515	1000-1200	350-525	D638
Hardness, Shore D	D41-D50	D69	D62-66	D785
Izod Notched Impact Strength	No break	1600.05	No break	D256
Thermal				
Melt Temperature (℃)	110	130-137	132-138	D3418
Coefficient of Linear Thermal Expansion ($\times 10^{-6}$/℃)	0.3	0.6	1.1	D696
Heat Deflection Temperature (℃) @66psi/@264psi	48/36	76/40	95/82	D648

UHMWPE is known for its superior wear resistance. It is considered the most wear resistant polymer due to the high molecular weight. It can be easily manipulated due to its high tensile strength. Its light weight and extremely high impact toughness, even at cryogenic temperature, make it a good choice for ballistic applications such as bullet proof vests and armored vehicles. It is also non-toxic and can be used for food and pharmaceutical equipment, especially when periodically cleaned with live steam or boiling water for sterilization.

1.2.3. Tribological applications of polyethylene

Due to the low friction and high wear resistance, HDPE and UHMWPE have been most widely used as bearing materials [20]. HDPE is increasingly demanded in various industrial areas due to its vast tribological applications including automotive [21], liners and pressure pipe [22], low speed gears and bearing [23], etc. (Figure 1.4). UHMWPE is also exploited as bearing components in a wide range of industrial applications including lining for coal chutes, runners for bottling production lines, wear strips, chain guides etc. [24]. In the mining industry, UHMWPE has been used in lining dump trucks and buckets for protection of equipment (Figure 1.4 (a)). By replacing steel or aluminum, it reduces the weight of the bed or bucket to improve the capability and elongate the longevity of the bulk transport. Due to the low friction, UHMWPE liners can not only protect the equipment, but also show the superior removing ability as illustrated in Figure 1.5.

Figure 1.4: The industrial application of HDPE as bearing materials: (a) gears [25]; (b) bearings [26]; and (c) liners [27].

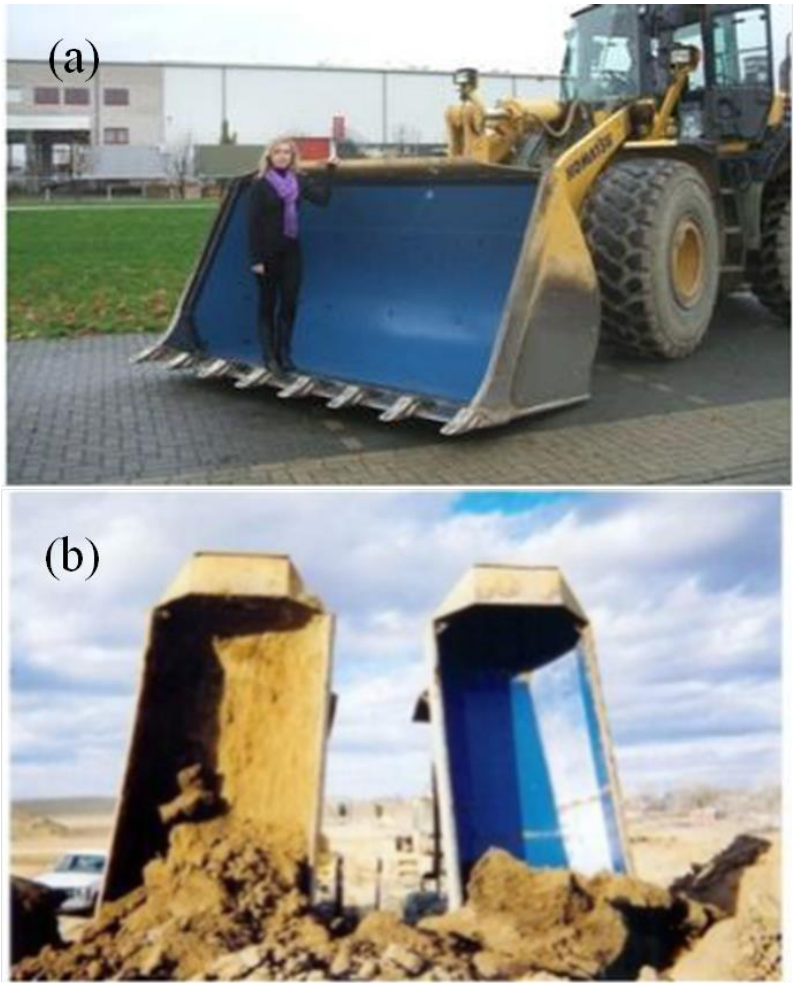

Figure 1.5: (a) UHMWPE lining for protection of the equipment and (b) improving the removing ability (reprinted with permission from Ref. [28]).

In addition, one of the important biomedical applications of UHMWPE is the key material of choice for total joint replacement. The majority of total hip prostheses consist of a polished metallic alloy or ceramic femoral head articulating against a plastic acetabular cup as shown in Figure 1.6. Extensive studies have been carried out on the development of suitable plastic materials for the acetabular cups. Today, UHMWPE not only remains the most frequently used material in total hip replacements, but is also the essential interposition material in total knee replacements [30]. However, the life expectancies of these prostheses have been limited to be within 25 years [31]. In spite of its excellent anti-wear properties, wear debris was

still generated during UHMWPE's service life which would result in osteolysis, loosening of the implant, and eventually revision of the artificial joints [32].

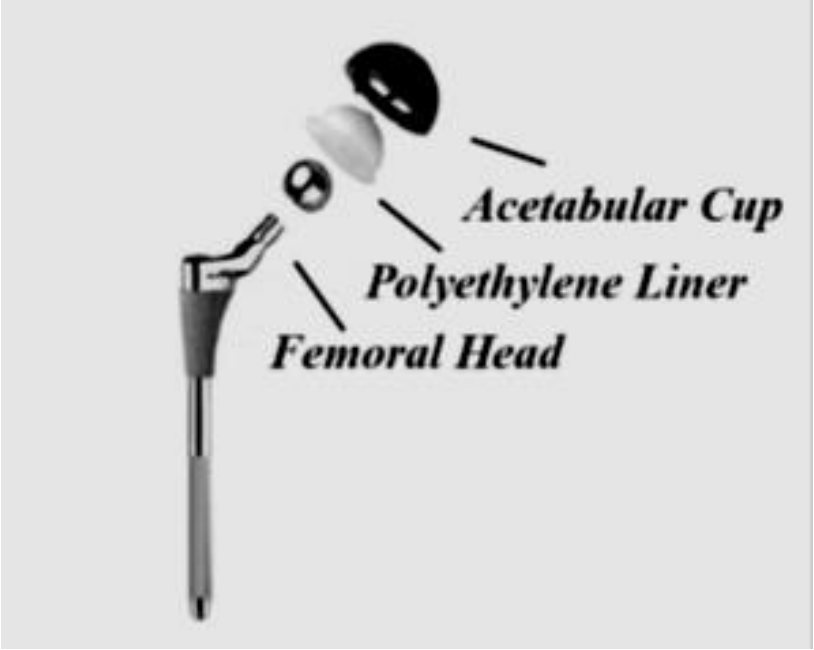

Figure 1.6: Schematic representation of artificial hip replacement (reprinted with permission from Ref. [29]).

Meanwhile, the attempts to use HDPE or its composites in plastic acetabular have never been abandoned. HDPE was used and examined in the 1980s to develop low-friction and low-wear arthroplasties [33, 34]. With the development of nanotechnology and new composite manufacturing techniques, HDPE nanocomposites were recently investigated as well for the application in total hip artificial joints [35-37]. Compared with UHMWPE, HDPE has essentially the same chemical structure, comparable mechanical properties, relatively low cost, superior creep resistance, better processability, and biocompatibility [36]. However, it was reported that with the long time use, HDPE exhibited a lower wear resistance than that of UHMWPE [38]. Therefore, currently HDPE is widely used as an additive for UHMWPE to improve its creep resistance and processability in total hip replacements, not as a bearing material.

1.3. Polyethylene-based nanocomposites

1.3.1. Overview of nanocomposites

Composites are materials consisting of two or more constituents. Composite materials have significantly different physical or chemical properties from the individual components. The new materials are usually preferred for excellent strength-to-weight and stiffness-to-weight ratios, when compared to traditional materials. Some other reasons include: less expensive, durable, heat-resistant, thermal and electrical conductive, etc.. With the development of nanotechnology, nano-fiber is becoming a popular reinforcement for polymeric composites.

A nanocomposite is defined as a multiphase solid material where one of the phases has at least one dimension in the range of 1-100 nm [39]. There are many advantages of nanocomposite compared to conventiaonal composites:

(1) Generally, nanocomposites differ from conventional composites due to the relatively higher surface to volume ratios of the nanofillers compared to the traditional microscaled fillers. Thus, a relatively small amount of nano-scale reinforcements could lead to observable effects on the macroscale properties of the composite;

(2) When the diameter of the fibers decreases, the numbers of surface defects become less, and thus the strength of the nanofibers is significantly improved. This phenomena can be verified in Figure 1.7 in which the ultimate strength of glass fibers increases with the decreasing of fibers diameter. Therefore, although bulk glass is very brittle and has relatively low strength, glass fibers are very strong and significantly less brittle;

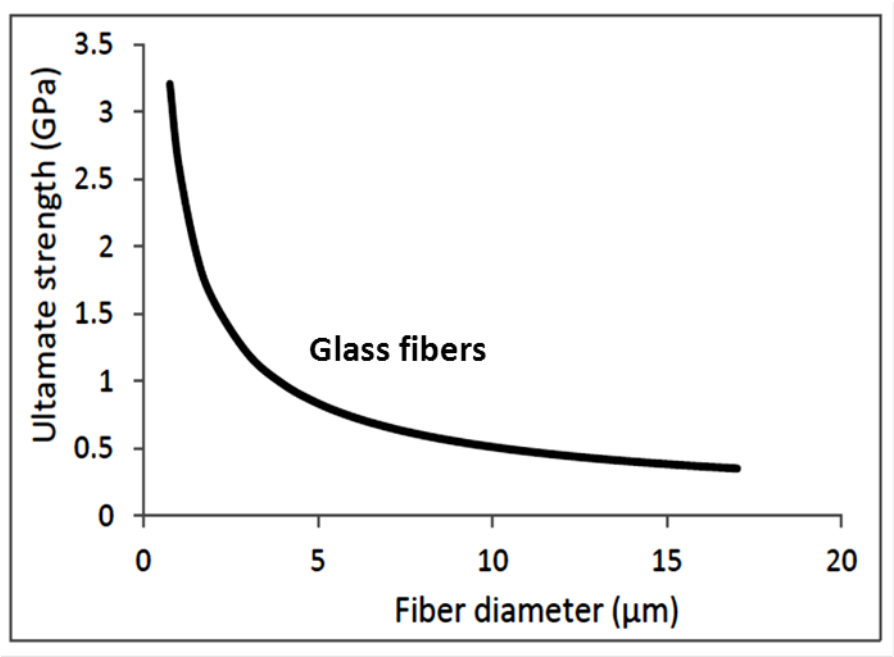

Figure 1.7: The tensile strength of glass fibers increases with the decrease of glass fibers diameter (reprinted with permission from Ref. [28]).

(3) The addition of nanoreinforcements to polymeric matrix is a possible way of improving desired mechanical properties of the composites without necessarily compromising their toughness [37]. For example, short carbon fibers have already been applied into UHMWPE as reinforcements for the artificial implants since as early as the 1970s [40]. This short carbon fiber-reinforced UHMWPE composite, named Poly II[TM], improved the wear behavior of UHMWPE considerably in the laboratory; however, such improvement was at the cost of toughness, crack resistance and fatigue resistance reduction [41]. Therefore, Poly II[TM] ran the fatal risks *in vivo*, early fracture and extensive delamination [24, 41, 42]. Actually, similar problems usually occurred with most macro-and microscopic fillers, because such fillers led to high stress concentrations at the interface [40]. However, due to the small size of nano-reinforcement and the lower filler concentration, the toughness of the polymer matrix can be maintained, or even improved in some cases [43-45].

1.3.2. Tribological properties of polyethylene-based nanocomposites

As mentioned in Section 1.2.3., HDPE and UHMWPE and their composites have been increasingly used for tribological applications due to their low friction and good wear resistance. Fillers and reinforcements are added into HDPE or UHMWPE matrix to improve the mechanical properties and potentially improve the material's wear resistance. Due to the various advantages of nanocomposites described in Section 1.3.1., nanocomposites seem to be good choices to enhance wear resistance. In particular, the major benefits of nanocomposites for tribological application were summarized as [46]: (1) interfacial bonding between the nano-fillers and the matrix was supposed to be better as the nano-fillers had large specific surface areas and high aspect ratios; (2) nanocomposite only needs a low concentration of nanofillers, and therefore the toughness and surface energy of the matrix material can be maintained, which are believed to be strongly correlated with the wear properties of polymer; (3) the nano inclusions may indirectly improve the wear behavior of the nanocomposite by changing the crystallinity, microstructure, glass transition and degradation temperatures, and other mechanical properties of the polymer matrix; (4) In addition, some nanofillers have self-lubricating function. For example, nanographite can reduce friction and wear of the nanocomposites.

Xiong et al. [47] prepared the nano-Al_2O_3/UHMWPE nanocomposites using hot pressing and irradiation by gamma ray, and found that the wear resistance of the nanocomposites against CoCrMo alloy under physiological saline solution lubrication was increased by 150% with 2% nano-Al_2O_3 compared to pure UHMWPE. The filling particles were believed to have linked with the UHMWPE molecular chains, resulting in an improved shear modulus [47]. Indirectly, the crystallization process was also modified by the addition of the Al_2O_3 nanoparticles that formed new nucleation sites [47]. Liu et al. [48] investigated the surface hardness and wear resistance of montmorillonite (MMT) reinforced HDPE

nanocomposites, both of which were significantly improved by the addition of low loadings of nano-MMT with polyolefin elastomers as the surfactant. Moreover, it was reported that the MMT fillers led to an enhancement of impact toughness [48]. Xiong et al. [49, 50] prepared the UHMWPE/nano-hydroxyapatite composites for the application of artificial joints by vacuum hot-pressing and gamma irradiation. The friction and wear behavior were characterized using cylinder (CoCrMo)-on-plane (sample) test machine under deionized water lubrication. The nanohydroxyapatite led to decreased contact angles and increased wettability which enhanced the lubricity of the contact pair under deionized water and lowered the friction coefficient of the nanocomposite consequently [49]. UHMWPE filled with 1% nano-hydroxyapatite exhibited a significant reduction of wear rate against CoCrMo alloy [49]. In this work, the higher elastic modulus of reinforced UHMWPE resulted from the nano-hydroxyapatite inclusions was considered to be the reason for achieving better wear resistance against abrasion.

Compared to UHMWPE-based nanocomposites, HDPE-based nanocomposites have good processability due to the low viscosity of HDPE at elevated temperatures. Many studies have been dedicated to the use of HDPE nanocomposites as the bearing inserts in total joint replacement components. [6, 35-37, 51, 52] Johnson et al. [37] studied the effect of carbon nanotubes (CNTs) on mechanical properties and wear behavior of HDPE nanocomposites. The results indicated that the addition of 5 wt.% CNTs decreased the wear rate and coefficient of friction of the nanocomposites by up to 50% and 12%, respectively. Kanagaraj et al. [51] found that HDPE/CNT nanocomposite with 0.44 wt.% of CNTs concentration showed a 22% enhancement of elastic modulus compared with neat HDPE. Fouad et al. [36] investigated the thermal, rheological, cytotoxicity, mechanical and abrasive wear behaviors of HDPE nanocomposites reinforced with graphite nano-particles (GNPs). The cytotoxicity test results showed that the neat HDPE and all HDPE/GNPs nanocomposites with different GNP

concentrations did not exhibit any cytotoxicity to the WISH cell line. The tensile strength, Young's modulus and shear modulus of HDPE/GNPs nanocomposite were found to be comparable to that of UHMWPE. The addition of 4 wt.% GNPs improved the abrasion resistance of the material by up to 8% compared to the neat HDPE.

1.3.3. Effects on the performance of nanocomposites

Effect of concentration. One of the advantages of nanocomposites is the large improvement of desired properties in the cost of low concentration of the reinforcements. Based on the traditional linear law of mixture [53], the more reinforcements were added into the matrix, the more improved properties would be achieved. However, this is not the case for polyethylene-based nanocomposites. Particle shaped nanofillers could have a higher concentration as much as 10 wt. % compared with fiber shaped nanofillers [36, 49, 54]. A low concentration of fiber shaped nanofillers, usually less than 5 wt.%, may provide the resulting nanocomposite material with significant property improvement due to their high aspect ratios [55, 56]. Wear loss of UHMWPE/CNTs composite was found to continuously decrease as the concentration of MWCNTs increased (Figure 1.8) [2]. However, when the amount of nanofillers exceeded 0.5 wt.%, the wear resistance of the nanocomposite would gradually decrease [46]. High concentration of nanofillers could contaminate the improvement of desired properties, since nanofillers tend to aggregate due to the strong intrinsic Van der Waals forces, leading to poor dispersion. For example, CNTs usually agglomerate into ropes or bundles when dispersed in polymers [57]. A scanning electron microscope (SEM) can be useful in identifying the presence of agglomerates (Figure. 1.9 (a)) [37], where the small lighter spots are the nanotube clumps. Nanotube agglomerates were also found in the debris accumulated on the counterpart surface after dry sliding wear of the UHMWPE/HDPE blend with 2 wt.% MWCNTs (Figure. 1.9 (b)) [58]. Those agglomerates not only affected the consistency of the nanocomposites, but also enhanced the abrasive wear as the third-body wear agents [46]. With

high strength and modulus, those nanofiller agglomerates acted like metal scourers, scratching the surface of the nanocomposite back-and-forth during the wear process. It was also shown in [40] that the presence of large CNF clusters in the UHMWPE nanocomposite containing 10 wt.% of CNFs further degraded the wear performance of the nanocomposite.

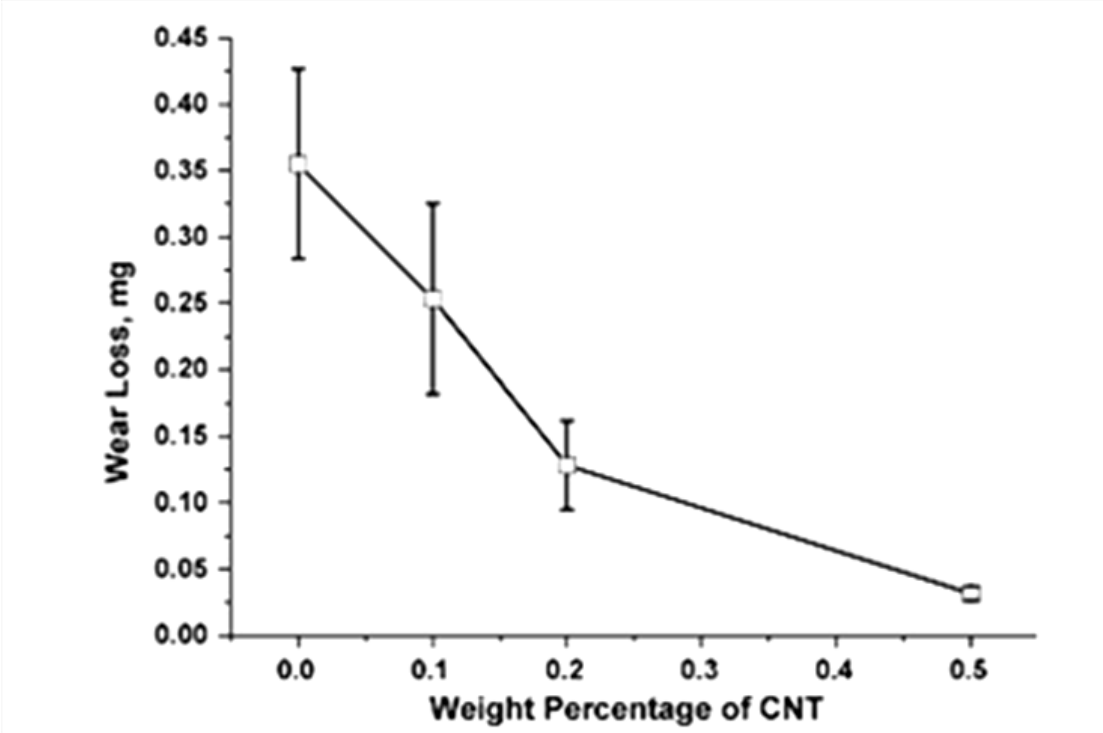

Figure 1.8: Influence of fiber concentration at low loading levels on the wear rate of UHMWPE/CNT nanocomposites (reprinted with permission from Ref. [2]).

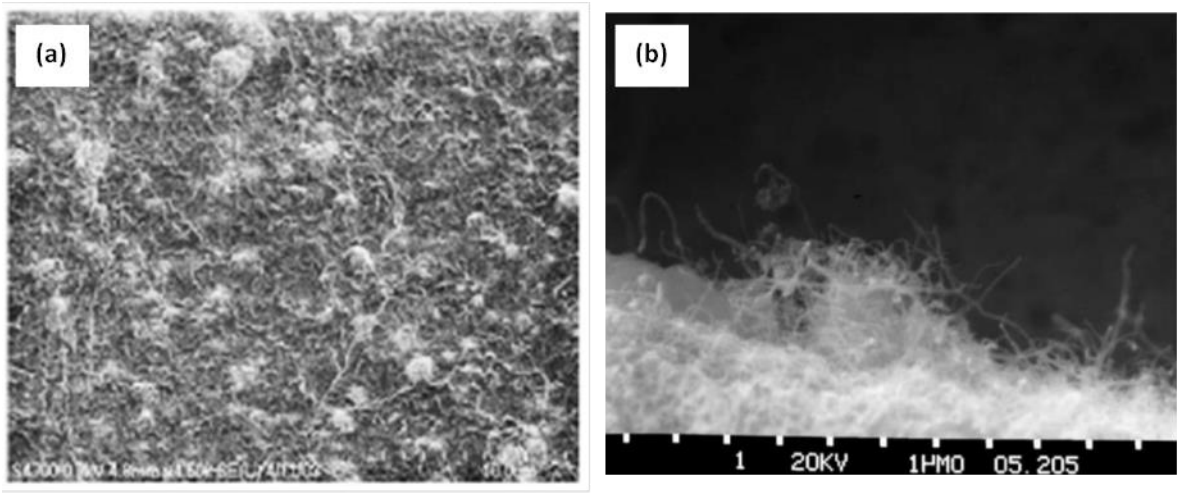

Figure 1.9: (a) CNT agglomerates in the UHMWPE matrix (reprinted with permission from Ref. [37]; Copyright (2009) Elsevier) and (b) CNT agglomerates inside the wear debris on the surface of a X5CrNi18-10 steel ball after sliding against UHMWPE/HDPE blend with 2 wt.% MWCNTs (reprinted with permission from Ref. [58]; Copyright (2006) Elsevier).

Effect of surface treatment. The performance of polymer nanocomposites depends on the dispersion of nanofillers in the matrix and interfacial interactions between the fillers and the matrix. Therefore, different nanofiller treatments have been attempted to improve the dispersion and interfacial interactions, including the purification and functionalization of the nanofillers. For polar polymer matrices, even simple oxidation of nanofillers can work well to enhance the load transfer and the dispersion of nanofillers within polymer matrices, due to polar interactions [59, 60]. However, for the matrix of non-polar polyethylene, the approaches to obtain advanced nanocomposites in volume production have been more challenging. In Lee's work [61], MWCNTs were oxidized and silanized using acid mixture and 3-aminopropyltriethoxysilane, respectively, to improve the interfacial strength. It was observed that silanized CNT-reinforced UHMWPE nanocomposites have a remarkably lower friction coefficient and decreased wear rate by about 83% at 0.12 m/s dry sliding speed compared with the neat UHMWPE [61]. Compared to CNTs, CNFs have much higher purity (for example, Pyrograf –III CNFs from Applied Sciences, Inc., have more than 99.9% fibrous carbon material and very low metal concentrations) and more active edges to facilitate functionalization [6].

Sui et al. [62] discussed the effect of a pretreatment for CNFs on the mechanical properties and friction behavior of UHMWPE/HDPE nanocomposites. Fewer exposed CNFs were found in the fracture surfaces of UHMWPE/HDPE nanocomposites with the pretreated CNFs than with the untreated CNFs [62]. Hence, the dispersion and interfacial adhesion of the pretreated CNFs were improved. The enhancement in tensile strength of nanocomposites with 0.5 wt.% pretreated CNFs was four times higher than that with untreated CNFs [62].

1.3.4. Wear mechanisms

The wear mechanisms of polymers can be grouped into several categories including abrasive, adhesive, fatigue, and delamination wear. Those wear mechanisms or combinations of them have been reported in the wear of UHMWPE, HDPE and their nanocomposites [2, 5, 46, 54, 58, 63].

Abrasive wear. As the most common type of wear in polymer composites, abrasive wear occurs when a hard rough surface slides across a softer surface [64]. According to ASTM, the definition of abrasive wear is the loss of material due to hard particles that are forced against and move along a solid surface [65]. Abrasive wear can be sub-divided into two processes [66]: two-body abrasive wear and three-body abrasive wear according to the type of contact and contact environment (Figure 1.10). When the grits or asperities that are rigidly mounted or adhered to the counterface remove the material from the soft surface, a two-body abrasive wear occurs [67]. During a three-body wear, the material is removed by particles that are not constrained and are free to roll and slide across a surface [67] . Three commonly identified characteristics of abrasive wear are plowing, cutting, and cracking [67]. The abrasive wear was reported most frequently in UHMWPE nanocomposites [5, 54, 58, 63]. For example, the 10 wt.% UHMWPE/nano-MMT and the 10 wt.% UHMWPE/nano-TiO_2 were found to have the abrasive wear mechanism, shown in Figure 1.11 [54, 63].

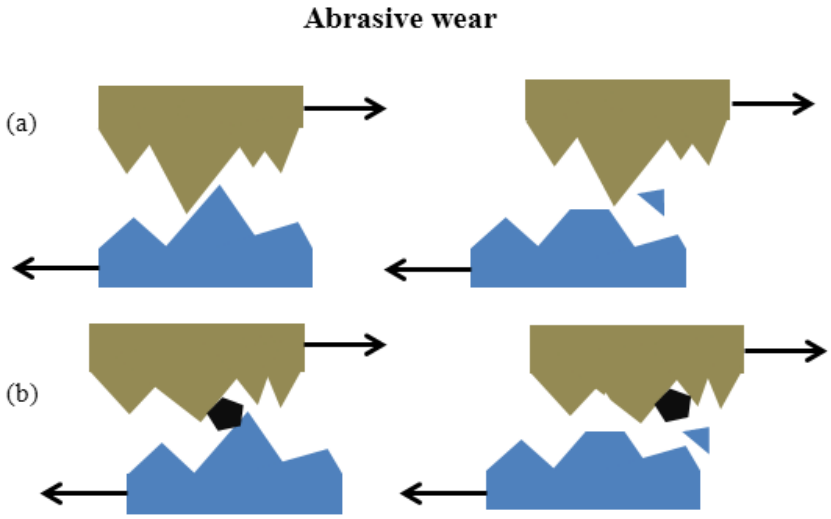

Figure 1.10: Schematic diagrams of the abrasive wear mechanism: (a) two-body abrasive wear and (b) three-body abrasive wear.

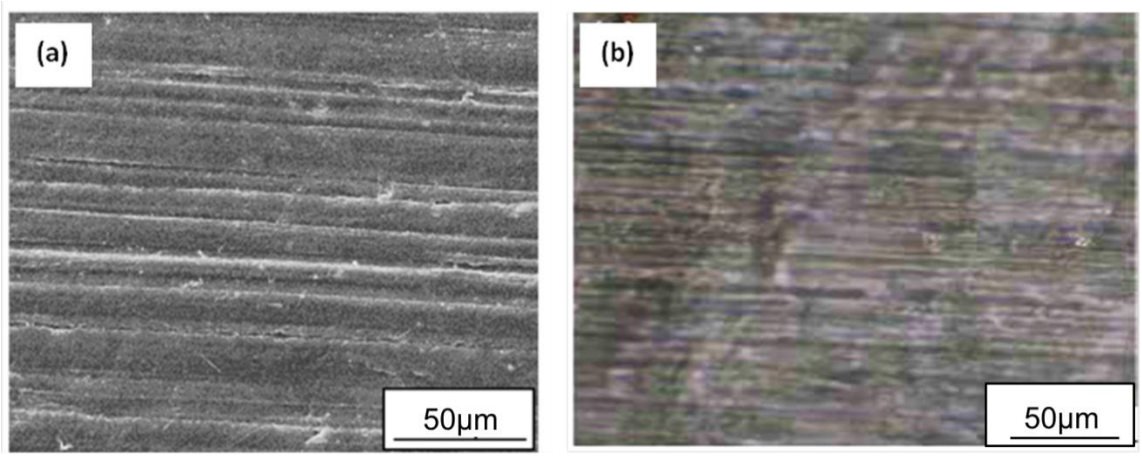

Figure 1.11: SEM micrographs of worn surfaces of (a) 10 wt.% nano-MMT/UHMWPE nanocomposite (reprinted with permission from Ref. [54]; Copyright (2008) Elsevier) and (b) 10 wt.% nano-TiO_2 /UHMWPE (reprinted with permission from Ref. [70]).

Adhesive wear. Adhesive wear is a result of material transfer from one surface to another due to the deformation and adhesion of the opposing asperities on the rubbing surfaces [46]. When two surfaces slide against each other, junctions are formed at the actual contact between asperities resulting from welding, physical or chemical interactions, or possibly heating at the interface which may be high enough to cause melting or softening of the sliding

polymer surface [68]. If further sliding is continued and the bonding between the interfaces of asperities is greater than the strength of the polymer, fragments will detach from the surface and adhesive wear occurs as shown in Figure 1.12. The obvious tears on the worn surface imply the occurrence of adhesive wear. An example showing adhesive wear in nanocomposites is given in Figure 1.13(a) for UHMWPE/CNTs (0.5 wt.%) [2]. It was believed that the HDPE chains compared with UHMWPE had the ability to flow under elevated temperatures caused by friction during dry sliding [69]. When heated to sufficient levels, the strength of the adhesive bonds between the counterface metal and the surface of the HDPE nanocomposite could be greater than the strength of the surface layer, resulting in adhesive wear instead of abrasive wear [70]. The adhesive wear of HDPE was evidenced through the wear debris analysis as shown in Figure 1.13(b), in which the small, flake-like debris indicated adhesive wear. It is noted that the improved thermal conductivity would reduce the negative thermal softening effects on the wear rate and allow the surface layer of the sample to maintain strength, while the decreased friction would weaken the adhesive bonds between the counterface and the surface layer [69, 70].

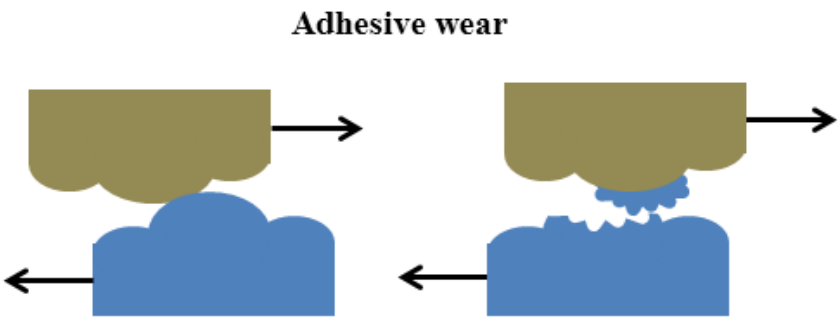

Figure 1.12: Schematic diagram of the adhesive wear mechanism.

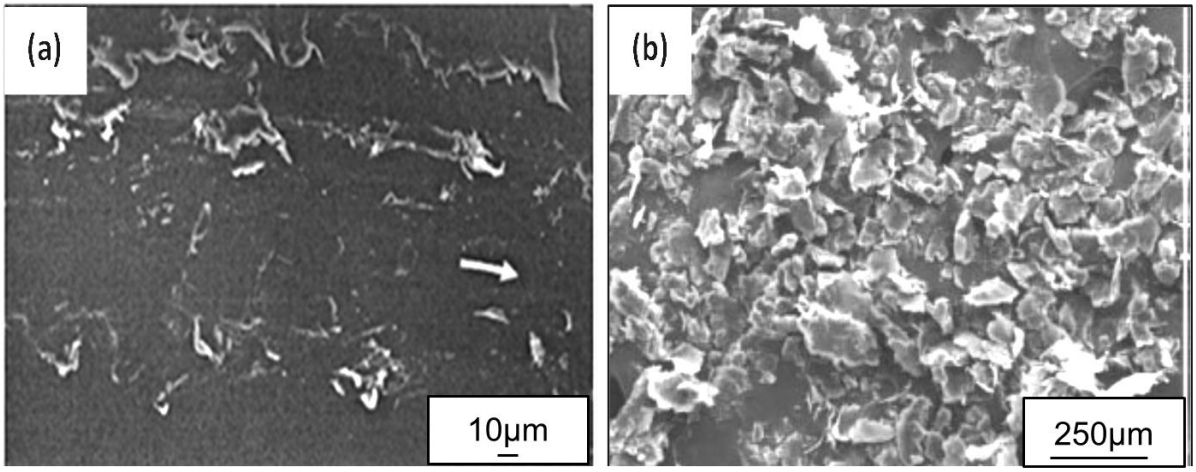

Figure 1.13: (a) Adhesive wear of the UHMWPE/0.5 wt. % CNT nanocomposite (reprinted with permission from Ref. [2]) and (b) wear debris of HDPE/UHMWPE blend with 1 wt.% CNFs (reprinted with permission from Ref. [167]; Copyright (2009) John Wiley and Sons).

*Fatigue wear and delamination wear***.** Fatigue wear is due to the weakness of surface material by cyclic loading as shown in Figure 1.14. In this case, the wear debris is detached by cyclic crack growth of micro-cracks on the surface. These fatigue cracks start at the material's surface and spread to the subsurface regions [46]. The cracks may connect to each other resulting in separation of the delamination of the material pieces, which is shown in Figure 1.15(a) [58].

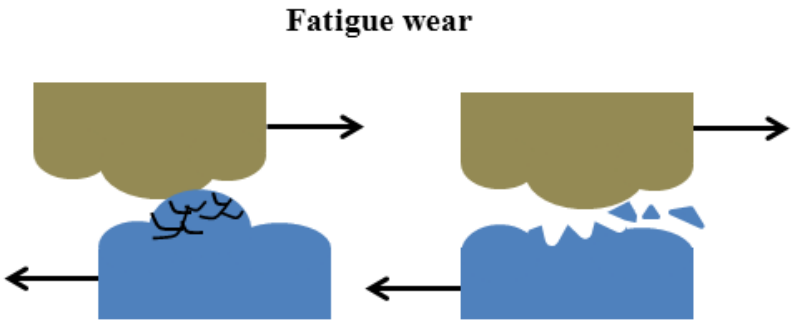

Figure 1.14: Schematic diagram of the fatigue wear mechanism.

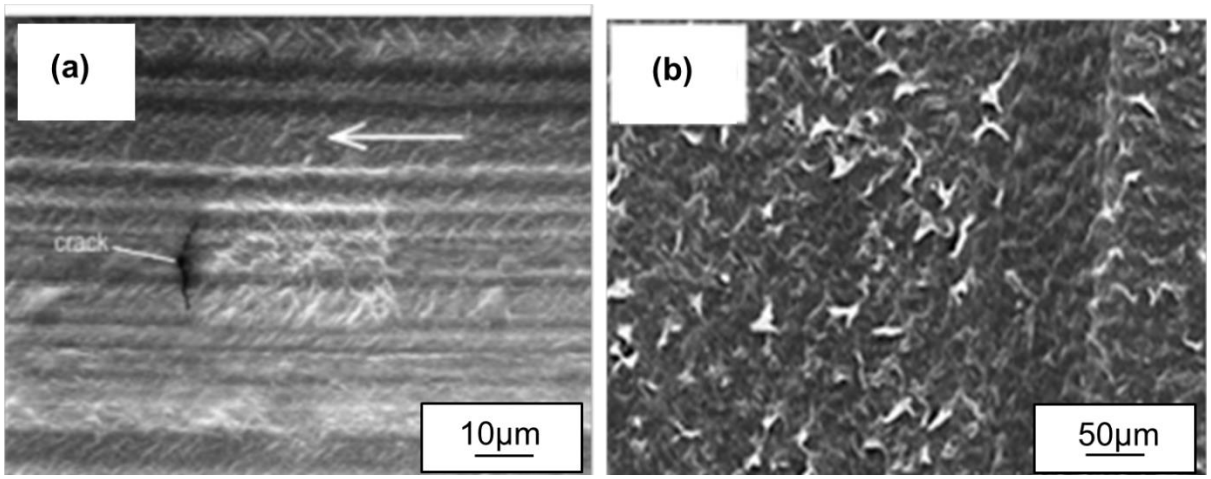

Figure 1.15: (a) Fatigue wear in UHMWPE/HDPE blends with 2 wt. % CNTs (reprinted with permission from Ref. [58]; Copyright (2006) Elsevier) and (b) ripple-like micro-scale topography of the worn surface under delamination wear (reprinted with permission from Ref. [71]; Copyright (2009) Elsevier).

Some reports suggested that delamination mechanism could be the main mode of wear for UHMWPE or HDPE applied to artificial knee and hip joints under cyclic loading [20, 72, 73]. Delamination wear takes place when two surfaces are brought together into contact only at the asperities, and small, localized plastic deformation occurs under these asperities [46]. A schematic of delamination wear is shown in Figure 1.16 [74]. The delamination wear mechanism seems more like a combination of the adhesive wear and fatigue wear. The worn surfaces of delamination wear were observed to have ripple-like microscale topography as shown in Figure 1.15 (b) [71]. As long as microplastic flow occurs in the thin layer of the bearing surface, ripples can be formed under repeated cyclic compression shear stresses.

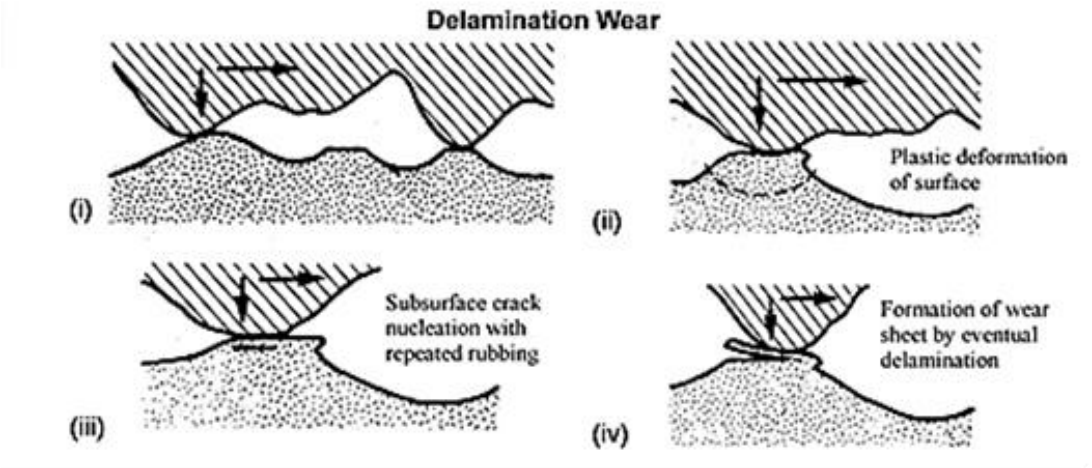

Figure 1.16: Schematic diagram of the delamination wear mechanism (reprinted with permission from Ref. [46]; Copyright (2009) Elsevier).

1.3.5. Wear models

To model the wear of materials, a classical wear model, Archard's law, claimed the following statements for dry sliding wear [12, 75]:

(1) wear volume is proportional to the sliding distance;

(2) wear volume is proportional to the normal load;

(3) wear volume is inversely proportional to the plastic yield pressure of the softer material under the normal load.

Archard's law can be expressed as an equation [12, 75]:

$$\Delta V = K_a \frac{N}{P_m} L \tag{1.2}$$

where ΔV is the volume of the worn off material, K_a is a constant, called Archard's wear rate, N is the normal load, P_m is the plastic yield pressure of the softer material in the two rubbing bodies, and L is the sliding distance. It should be noted that the yield pressure in Equation (1.2) was usually replaced with the indentation hardness (H) in later studies, as the yield pressure was recognized to equal the hardness value [1, 46, 76]. Archard's law postulated that the surface asperities are entirely deformed plastically under the applied normal load, and the term

N/P_m thus physically represents the true contact area between the two rubbing materials [75]. Sometimes the hardness (H) as a constant material property can be hidden in Archard's wear rate, K_a. Equation (1.2) can also be rewritten as: $\Delta V = K_s NL$, where K_s is called specific wear rate. The confirmation of these relationships between the wear volume and sliding distance as well as the wear volume and the hardness of the softer materials described in Archard's law can be found in [75, 77]. The relevant figure is reproduced in Figure 1.17.

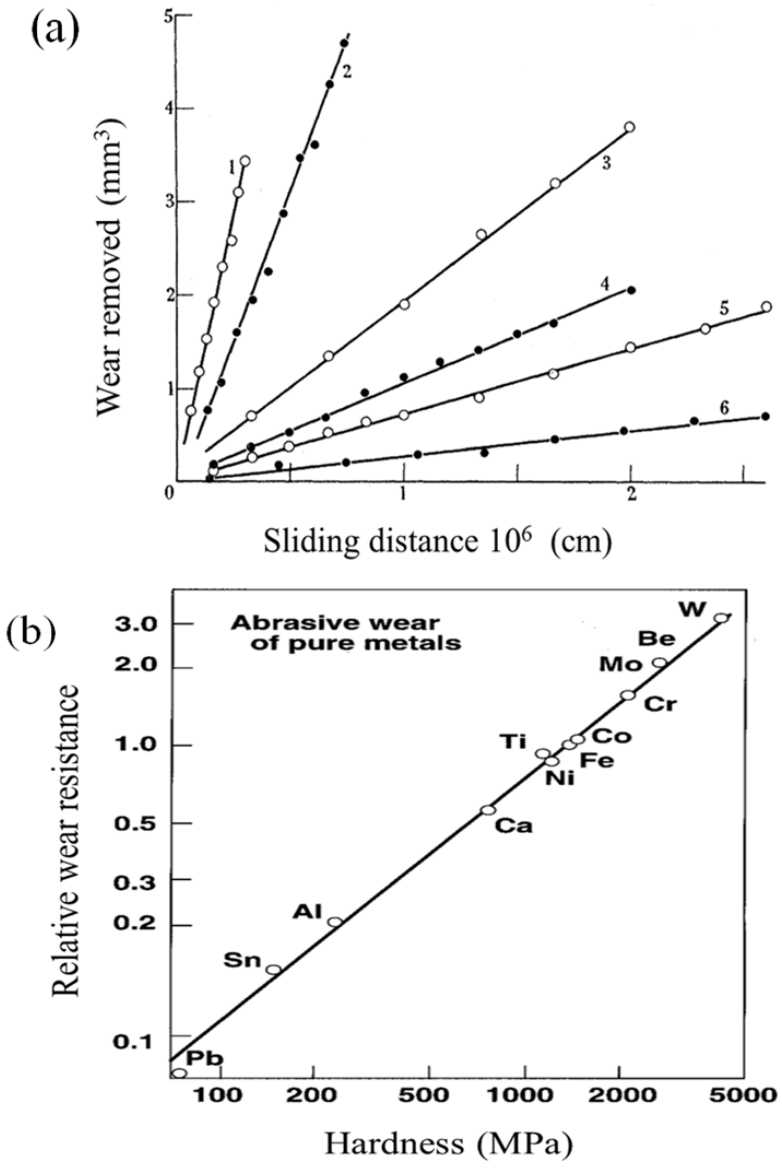

Figure 1.17: (a) Confirmation of the relationship between wear and sliding distance (1, Teflon on tool steel; 2, brass on tool steel; 3, ferritic stainless steel on sintered tungsten carbide; 4, Berllium copper on tool steel; 5, stellite grade 1 on tool steel; 6, sintered tungsten carbide on mild steel; reprinted with permission from Ref. [75]) and (b) Relationship between wear and hardness (reprinted with permission from Ref. [77]).

While Archard's law is indeed true for many systems, there are still two concerns when it is applied to the wear of polymers under lubricated conditions. The first concern is that Archard's law was developed for metals assuming the contacted asperities were totally plastically deformed [75]. It may or may not apply to other materials [1]. Because the elastic moduli of polymers are significantly lower than those of metals, it is believed that the plastic deformation in polymers becomes the predominant mode only when the asperity of the harder material is very sharp; otherwise, elastic deformation would play a much more important role in the wear process of polymers [78]. In addition, the deformation of polymers is also strongly time-dependent on their viscoelastic properties [79]. Therefore, the indentation hardness which incorporates the plastic yield pressure in Archard's law is not a good predictor for the wear of polymers [28, 78].

The second concern is that Archard's law, derived based on solid contact mechanism, is only examined for dry sliding contact in Archard's original paper [75]. Archard's law assumes that the normal load is entirely supported by the contact pressure of the asperities under dry sliding condition. Despite being widely used in the prediction of metal's wear under lubricated conditions, there have been few published works that validate the relationship between wear volume of polymers and the normal load under lubricated conditions. Under dry sliding condition, the normal load is only supported by the asperity contacts [1]; however under lubricated conditions, the normal load is supported by different mechanisms. The Stribeck curve is used to study the variation of friction (coefficient of friction, μ) between two liquid lubricated surfaces as a function of a dimensionless lubrication parameter $\eta v/p$, where η is viscosity of lubricant, v is sliding velocity, and p is pressure. The Stribeck curve can also be used to categorize the different lubrication mechanisms as shown in Figure 1.2 [1, 76, 80]. For example, in hydrodynamic (or thick-film) lubrication regime, the two rubbing surface are fully separated with the pressure build-up in the lubricant and a thick-film forms between them. The

force leading to the wear is the friction force between lubricants and the worn material, which significantly depends on viscosity of the lubricant. In mixed lubrication, asperity contacts and the build-up pressure of the lubricant support the normal load together. Therefore, under hydrodynamic and mix lubricated conditions, the pressure from the normal load on the worn surface is significantly influenced by the properties of the lubricant, which is not considered in the derivation of Archard's law. Due to the above concerns, it is reasonable to suspect the applicability of Archad's law in the wear of polymers under lubricated conditions.

Lancaster et al. [78] then proposed a relation for polymers between the wear volume *V* and other factors

$$\Delta V = K_L \frac{\mu N L}{H \epsilon_u \sigma_u} \tag{1.3}$$

where K_L is a constant as the Lancaster's wear rate, σ_u and ϵ_u are the ultimate tensile strength and strain, respectively. However, although using the hardness as a predictor for wear rate is true for pure metal as shown in Figure 1.17(b), some researchers believe that it should be avoided for polymeric materials, because wear of polymers is generally more complicated than traditional metal wear due to their viscoelasticity, toughness and the formation of polymeric wear debris transfer films [28, 81]. However, it has been proven that the wear volume most strongly correlate with $\epsilon_u \sigma_u$ (Figure.1.18) which can be described as an index of the toughness of the material.

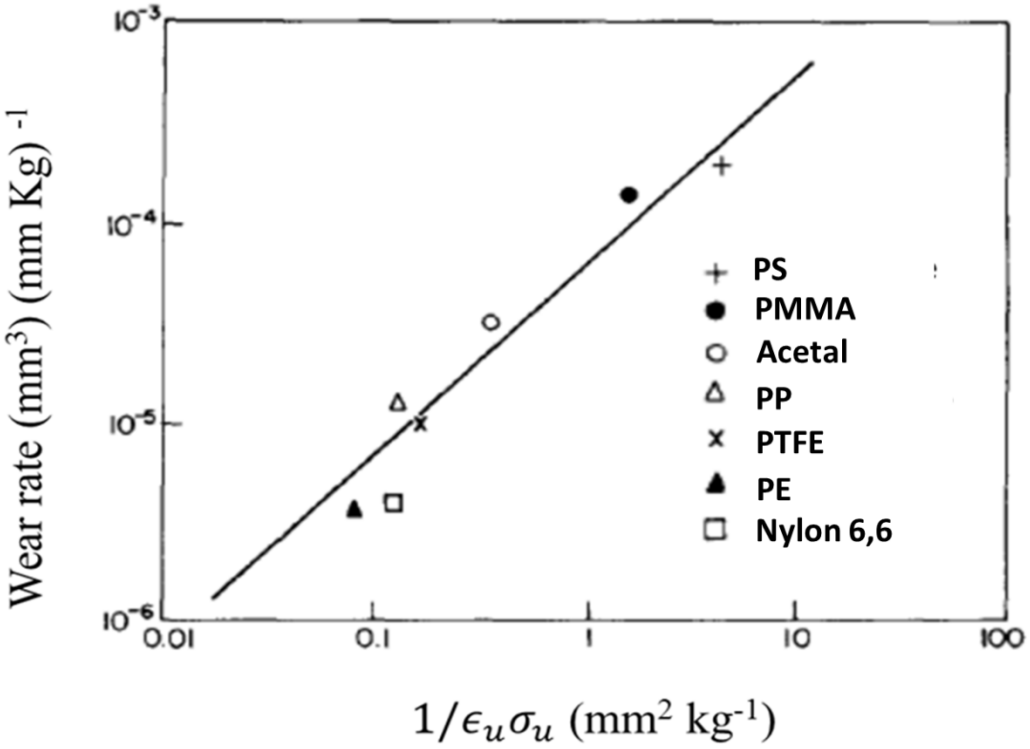

Figure 1.18: Relationship between wear rate and product of ultimate strength and strain for polymeric materials (reprinted with permission from Ref. [82]).

In addition, Reye's model [83] that the volume of the removed debris due to wear is proportional to the work done by friction forces, was considered more consistent with the wear of polymer than Archard's equation. The Reye's model can be written in following form

$$\Delta \mathrm{V} = \mathrm{K}E_f = K_f \int_0^L F_x(x)dx = K_f N \int_0^L \mu(x)dx \approx K_f \bar{\mu} N L \qquad (1.4)$$

where E_f is friction energy; F_x is friction force; $\bar{\mu}$ is average value of COF. K_f is a new wear rate called specific wear volume in a recent study [84]. However, to the best knowledge of the author, there is no wear model that is specifically developed for the wear of PE family materials.

1.4. Scope of the research

In this work, CNFs have been added into the HDPE polymer matrix, due to their excellent mechanical properties and high thermal conductivity. Three types of CNFs (pristine,

thicker-silane and thinner-silane treated CNFs) at different loading levels (0.5 wt.%, 1 wt.% and 3 wt.%) are used as nanoreinforcements to improve the mechanical, thermal, and tribological properties of the HDPE/CNF nanocomposites. The fabrication of the nanocomposites used in this research was done by our collaborator's group at Washington State University and was not in the research scope of this study. This research mainly focused on the investigation of tribological behavior of the nanocomposites, the understanding of the relationship between the wear and factors including friction, hardness, work of fracture, and thermal conductivity, and the development of wear models for dry sliding and lubrication conditions. The specific research tasks are shown below:

(1) Measure the mechanical properties and thermal conductivity of the nanocomposites, which will be used as parameters in latter studies (Chapter 2).

(2) Experimentally investigate the tribological behavior of the nanocomposites under dry, saline water, bovine serum lubricated condition, respectively and explore the possible correlations of wear with hardness and work of fracture (Chapter 3).

(3) Study the relationship between the wear and friction force under lubricated conditions (Chapter 4).

(4) Establish a thermal analysis method to determine the heat generation during a pin-on-disk wear test, correlate the wear with thermal conductivity, and develop an energy-based wear model for dry sliding condition (Chapter 5).

(5) Develop a theoretical model to predict the long-term wear of the nanocomposites under lubricated conditions (Chapter 6).

CHAPTER 2. MECHANICAL AND THERMAL PROPERTIES OF CARBON NANOFIBER REINFORCED HIGH DENSITY POLYETHYLENE NANOCOMPOSITES

The tribological behavior of a material is dependent on its mechanical properties, especially the hardness and toughness. Improving polymer's thermal conductivity is deemed to be a promising engineering approach to increase the frictional heat dissipation and result in significantly lower surface temperature on the polymer body. In this chapter, the mechanical properties (Young's modulus, ultimate stress, strain at fracture, work at fracture, hardness) and thermal conductivity of the HDPE/CNF nanocomposites are measured. It was found that the addition of CNFs increased the Young's modulus, work of fracture, hardness, and thermal conductivity of the nanocomposites. The contribution of mechanical and thermal properties to the wear of the nanocomposites will be discussed in Chapter 3 and Chapter 5. The obtained Young's modulus of the nanocomposites will be used in the future wear modeling works in Chapter 6.

2.1. Introduction

In recent years, the polymer nanocomposites reinforced with CNFs draw more and more attention due to the various advantages of CNFs including excellent strength, good thermal conductivity, high aspect ratio, multi-functionality and commercial availability [85], If CNF reinforced HDPE nanocomposites can exhibit an appreciable level of mechanical properties and thermal conductivity improvement, it may enhance the wear properties of HDPE for current tribological applications. Wood et al. [86] successfully treated oxidized CNFs with two types of silane coatings (with different thicknesses) and prepared the HDPE nanocomposites reinforced with these silane-treated CNFs. The storage modulus of HDPE nanocomposite reinforced by only 0.4 wt.% loading of thick silane-treated CNFs had a

dramatic enhancement (40%) compared with the neat HDPE. Moore et al. [87] incorporated CNFs into nylon 11 to synthesize nylon 11/CNF nanocomposites via twin screw extrusion. Compared to the neat nylon 11 with thermal conductivity of 0.24 W/m.K, the nylon 11/CNF nanocomposite with 7.5 wt.% CNF loading had an increased thermal conductivity of 0.3 W/m.K. Ma et al. [88] studied the effects of silane functionalization of multiwall CNT on the thermal properties of CNT/epoxy composites. It was indicated that grafting silane molecules onto a nanotube's surface improved the dispersion of the nanotubes in the epoxy matrix and resulted in improved thermal conductivity. Nevertheless, it seems that the mechanical properties and the thermal conductivity of HDPE/CNF nanocomposites have never been reported in literature. The present work will measure the mechanical and thermal properties of the nanocomposites and discuss the influence of CNF on the improvement of mechanical and thermal properties of HDPE/CNF nanocomposites.

2.2. Experiments

2.2.1. Materials

HDPE (HP54-60 Flake) supplied by Bamberger polymers Inc. was used as a matrix. The pristine CNFs (PR-24-HTT) and pretreated oxidized CNFs (PR-24-HHT-OX) were purchased from Applied Sciences Inc. with diameters of approximately 60 to 150 nm and lengths of 30 to 100 μm. Octadecyltrimethoxy-silane (ODMS) (90% technical grade) was manufactured by Sigma-Aldrich. The pretreated oxidized CNFs were modified with ODMS and ethanol solution, and a silane coating was formed to cover the fiber surface. Acetone was obtained from J.T. Baker. Ethanol was purchased from Decon Laboratories Inc.

The pretreated oxidized CNFs (ox-CNFs) were modified under subsequent treatment in boiling ODMS (90% technical grade)-ethanol solution. The condensation reaction of ox-CNFs and organosilane then occurred due to the reactive hydroxyl groups on the surface of

organosilane after hydrolysis, forming a silane coating to cover the fiber surfaces. By changing the ratio of ODMS to ox-CNF added and the percentage of ethanol and water in this reaction, it was possible to control the degree of hydrolysis and the thickness of silane coating. The average coating thicknesses were determined using TGA data, which were about 46 nm for silanized CNF-Treatment 1 and 2.8 nm for silanized CNF-Treatment 2 [86]. These two types of silanized CNFs have been chosen for this study.

Three levels of fiber concentrations of 0.5 wt.%, 1 wt.%, and 3 wt.% for both pristine CNFs and silanized CNFs were mixed with HDPE by a Haake Torque Rheometer to achieve good dispersion. The detailed descriptions of the samples were shown in Table 2.1, in which the weight percentage of CNF loading is also converted into volume fraction by taking the density of CNFs, HDPE, and silane coating as 1.95 g/cm^3, 0.954 g/cm^3, and 0.88 g/cm^3, respectively [86]. Mixing was set at 170 °C with a rotator speed of 30 rpm. The order of adding the materials was as follows: half amount of HDPE, CNFs, and then another half amount of HDPE. The speed was then raised to 70 rpm for 15 minutes. A neat HDPE reference was also prepared under identical conditions. Thereafter, the processed HDPE and the mixed polymeric nanocomposites were hot-pressed at 180 °C for 10 min via a hydraulic presser. The samples cooled down to room temperature naturally after the heat was turned off. The obtained samples from the hydraulic presser are with the size of 50.8 mm × 50.8 mm and thickness around 2.5 mm. It should be pointed again that the materials was prepared by our collaborators at Washington State University, and the detailed fabrication information can be referred to the Ref. [6, 28, 86].

Table 2.1: Descriptions of the HDPE/CNF nanocomposite samples.

Sample	Matrix	Reinforcement	Coating thickness	Weight Percentage (wt.%)	Volume fraction (vol.%)
Neat	HDEP	-		-	-
P-05		Pristine CNF (P-CNFs)	-	0.5	0.2
P-1				1	0.5
P-3				3	1.5
T1-05		Thicker-silane treated CNFs (T1-CNFs)	46nm	0.5	0.4
T1-1				1	0.8
T1-3				3	2.6
T2-05		Thinner-silane treated CNFs (T2-CNF)	2.8nm	0.5	0.3
T2-1				1	0.5
T2-3				3	1.6

2.2.2. Test methods

Tensile test. Tensile tests were carried out using a laboratory-made micro-load stage at room temperature, as shown in Figure 2.1. The load cell (SN: 384355) was used with the maximum load of 45 kg and a minimum load sensitivity of 0.0265 N. A constant strain rate of 0.002 mm/mm/s was maintained up to sample fracture and the tensile stress and strain data were recorded simultaneously throughout the test. The sample size was about 50.8 mm × 20 mm × 3.5 mm. At least five specimens were tested for each material. The average values of the elastic modulus, ultimate strength, and strain at fracture were determined from their stress-strain curves.

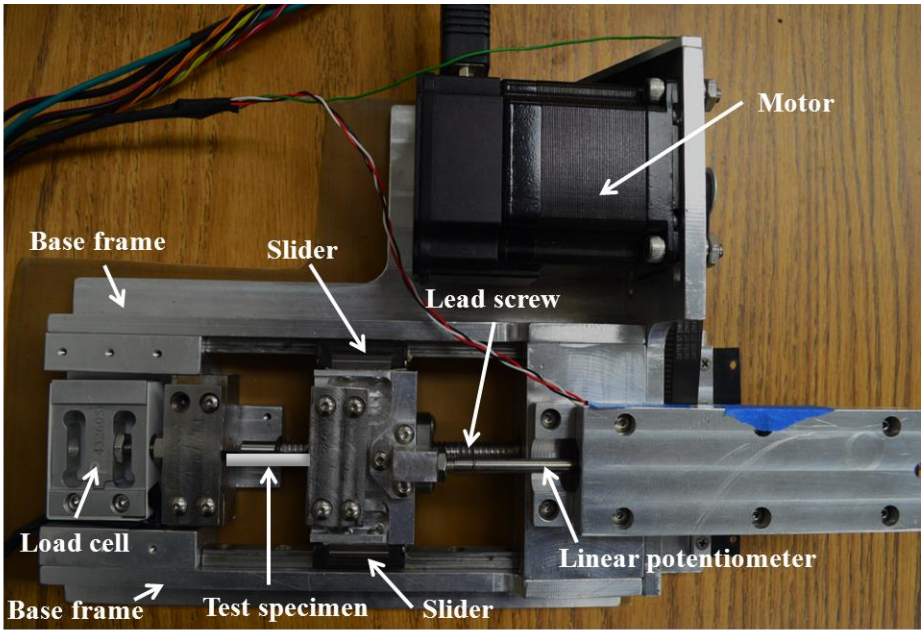

Figure 2.1: Top view of a laboratory-made micro-load stage.

Hardness test. The micro-hardness testing was conducted using a pin-on-disc tribometer (CETR-UMT-2) (see Figure 2.2). A load force of 3N and a stainless steel ball indenter with diameter of 3/16 in. (4.762 mm) was used. A loading cycle of 20s was implemented to ensure sufficient plastic deformation. Each specimen was indented three times at three different locations under the same loading condition. The depth of indentation was measured using a NT3300 optical profilometer. The micro-hardness (H) was calculated by the equation [89]:

$$H = \frac{P}{\pi[R^2 - (R - h)^2]} \tag{2.1}$$

where P is the applied load, R is the radius of the ball indenter, and h is the mean depth of the indentation after the indenter being removed. The average value of H from three measurements was recorded for each sample.

Figure 2.2: CETR-UMT-2 pin-on-disc tribometer set-up.

Thermal conductivity measurement. The measurement of thermal conductivity of the samples followed the standard guarded hot plate method (ASTM C 518). The apparatus consisted of two isothermal steel plates which acted as constant heat source (hot plate) and heat sink (cold plate), respectively. During the testing, a specimen was placed between the two square plates, illustrated in Figure 2.3. The face temperature was measured via an Omega Engineering HFS-4 heat flux transducer and the heat flux at each side of the specimen was measured by a K-type thermocouple embedded in each plate. To minimize the heat loss from areas not in contact with the plates, the specimen needs to have a good contact with the two plates and must be well insulated. After the specimens reached a thermal steady state, the minimum temperature difference through the thickness of the material was 10°C, and the heat

flux and temperatures were recorded to compute the thermal conductivity of the material. ASTM C 518 provides the following equation for calculating the thermal conductivity:

$$k = \frac{(\mu_{hot} \cdot v_{hot}) + (\mu_{cold} \cdot v_{cold})}{2} \cdot \frac{L}{\Delta T} \tag{2.2}$$

where μ_{hot} and μ_{cold} are calibration factors of the two HFS-4 heat flux transducers; v_{hot} and v_{cold} are the average voltage output (V) from the two heat flux transducers; $L\ (m)$ is the average thickness of the specimen; and ΔT (°C) is the temperature difference across the specimen measured by the embedded K-type thermocouples. The thermal conductivity values of ten types of materials are given in Table 2.3 and discussed in the next Section.

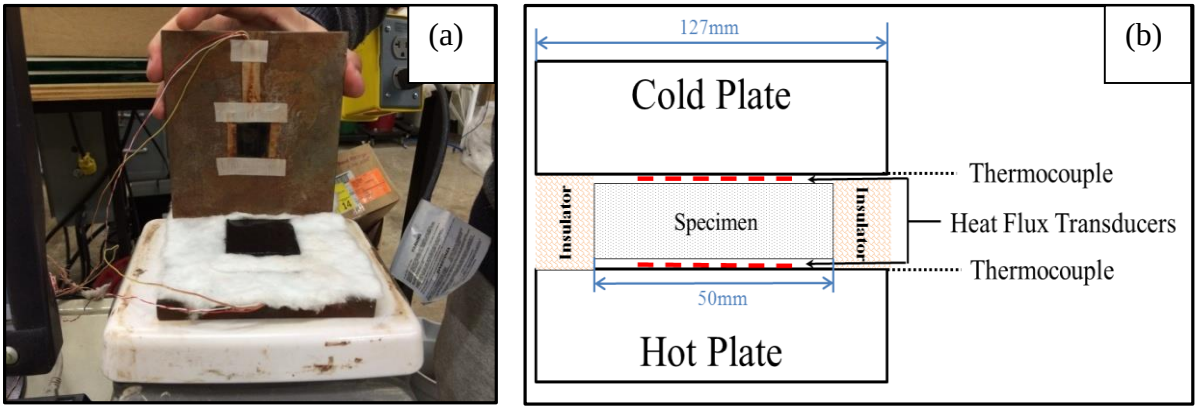

Figure 2.3: The photo (a) and schematic (b) of guarded hot plate method for thermal conductivity measurements with two heat flux transducers, two thermocouples, and one specimen.

Scanning electron microscopy analysis. The fracture morphology of the 3 wt.% HDPE/P-CNF and 0.5 wt.% HDPE/T1-CNF specimens were observed by a scanning electron microscope (JEOL JSM-7600F, Peabody, Massachusetts).

Transmission electron microscopy analysis. The transmission electron microscopy (TEM) of both thick-silane treated CNFs and HDPE/T1-CNF-0.5 wt.% nanocomposites were recorded on a transmission electron microscope (JEOL JEM2100 LaB_6, JEOL USA, Peabody, Massachusetts).

2.3. Results and discussion

2.3.1. Tensile properties

Figure 2.4 shows the stress-strain curves of HDPE and HDPE/CNF nanocomposites. The slope of the linear part of each curve determines the material's Young's modulus, and the curve's maximum point corresponds to the material's ultimate stress. Beyond the ultimate stress, the specimen began to form a "neck," and then the load fell until rupture occurred. Such curve features were also observed in the tensile tests of HDPE/CNT nanocomposites reported in Kanagaraj's work [51]. The mechanical properties of the nanocomposites, including Young's modulus, ultimate stress, and fracture strain, are summarized in Table 2.2.

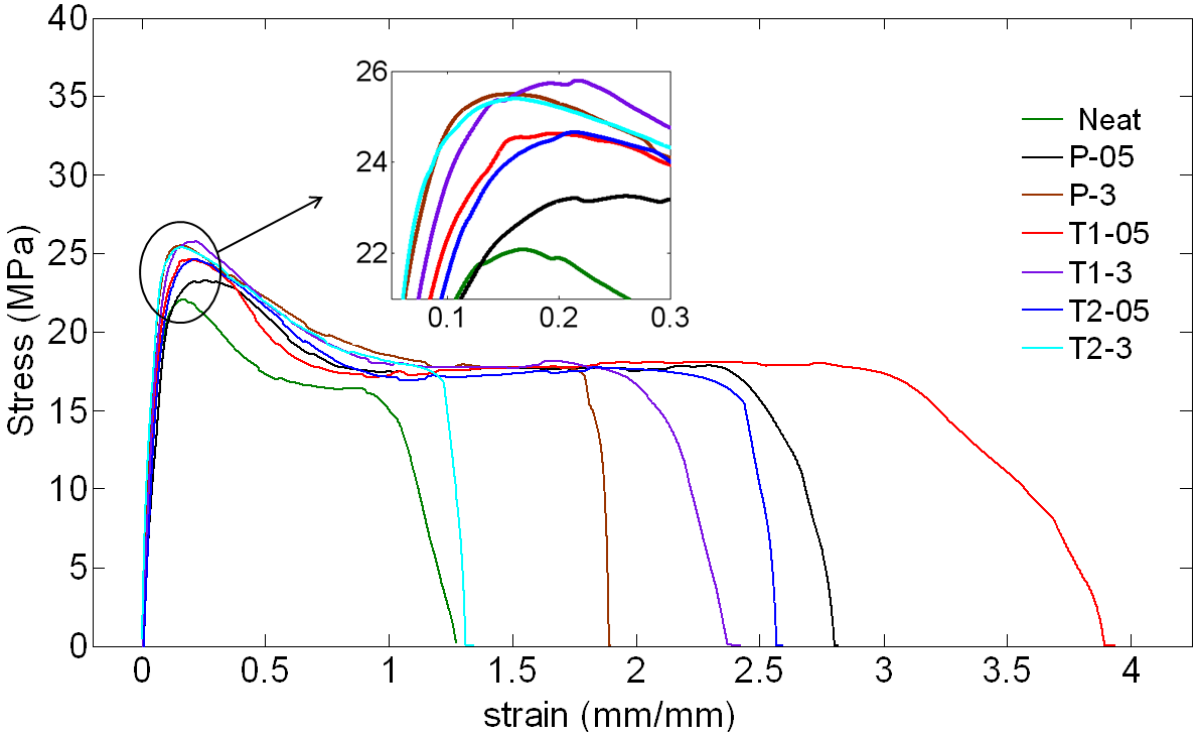

Figure 2.4: Stress-strain curves of HDPE and HDPE/CNF nanocomposite samples.

Table 2.2: Mechancial properties of HDPE/CNF nanocomposites.

Sample	Young's modulus E (MPa)	% Increment of E	Ultimate stress σ_u (MPa)	% increment of σ_u	Strain at fracture ε_u (mm/mm)	% increment of ε_u
Neat	526.83	0.00	22.09	0.00	1.28	0.00
P-05	512.81	-2.66	23.26	5.30	2.82	120.31
P-3	623.89	18.42	25.50	15.44	1.90	48.44
T1-05	537.54	2.09	24.64	11.54	3.94	207.81
T1-3	619.81	17.65	25.80	16.79	2.43	89.84
T2-05	533.08	1.19	24.62	11.45	2.60	103.13
T2-3	653.20	23.95	25.40	14.98	1.34	4.69

Young's Modulus. The addition of 0.5 wt.% CNFs of any type, pristine, thick- or thin-silane treated, did not have significant influence on the Young's modulus of the nanocomposites compared to the neat HDPE, and the differences were within ± 3%. With 3 wt.% of CNFs, the nanocomposites' Young's modulus were increased by about 20%, compared to the neat polymer. It seems that more CNFs lead to the higher Young's Modulus, possibly due to the fact that more CNFs results in more load transfer to the nanofibers' network [35].

Ultimate Stress. It is shown in Figure 2.4 that all the nanocomposites had larger ultimate stresses compared to the neat polymer. The ultimate stress values listed in Table 2.2 show that the 3 wt.% CNF loading level improved the ultimate stress more than the lower 0.5 wt.% loading level. With the same CNF concentration, the thick-silane treated CNFs resulted in the highest ultimate stress compared to the pristine and thin-silane treated CNFs.

Strain at Fracture. The strains at fracture of the nanocomposites were all higher than that of the neat HDPE. The nanocomposite with thick-silane treated CNFs at 0.5 wt.% level yielded the highest strain at fracture with a 207.81% increase compared to neat HDPE.

Although the addition of CNF may induce more fracture defects, the fracture strain enhancements of nanocomposites may be because of two mechanisms: (1) CNFs can effectively hinder the crack propagation to resist the strain improvement; (2) CNFs can absorb fracture energy through the interfacial deformation between CNF and HDPE matrix such as debonding, yielding or pullout [90, 91]. It was reported that thick-silane treatment produced a three-dimensional cross-linking network of silane coating on CNFs [86]. It is highly possible that the cross-linking network structure of thick-silane coating generates more interfacial deformation and absorb more energy from failure, compared to the pristine and thinner-silane treated CNFs. Therefore, at the same CNFs loading level, the thick-silane treated CNF reinforced HDPE led to the largest strain at fracture, compared with the thin-silane treated and pristine CNFs.

However, with the same silane treatment of CNFs, the strain at fracture decreased with increasing CNFs content to 3 wt.%. A possible reason is that at higher concentrations, the CNFs tend to aggregate more easily, leading to stress concentration within the matrix [51]. The nanocomposite with thick-silane treated CNFs at 0.5 wt.% level showed no aggregates of the CNFs in the HDPE matrix in the TEM image (Figure 2.5). As shown in the SEM image of Figure 2.6(a), the CNFs on the surface of T1-05 were worn off transversely and the cross-sections of the CNFs were exposed. Consistent with the TEM observation, the distribution of these CNF is basically uniform and the microstructure of T1-05 can be believed to be homogenous. However, the CNFs in the worn surface of P-3 were more inclined to aggregate, shown in Figure 2.6(b). The aggregates can be easily formed during the fabrication due to Van der Waals forces and the high surface energy of CNFs [46]. A suspension experiment indicated that thicker-silane treatment of CNF can make CNFs easily wetted by the liquid matrix resin which significantly contribution to the dispersion of CNF in HDPE matrix [86, 92]. The good dispersion of T1-05 results from the low concentration and the thicker-silane treatment on

CNFs. The good dispersion of thick-silane treated CNFs at 0.5 wt.% may be an important reason for obtaining the highest strain at fracture. In addition, the work of fracture (the area under the stress and strain curve) can also be determined from the tensile test and refers to the toughness of the polymer. The highest strain at fracture of T1-05 lead to the highest work of fracture which may contribute to the reduction of the wear rate. The detail discussion will be presented in Section 3.3.3.

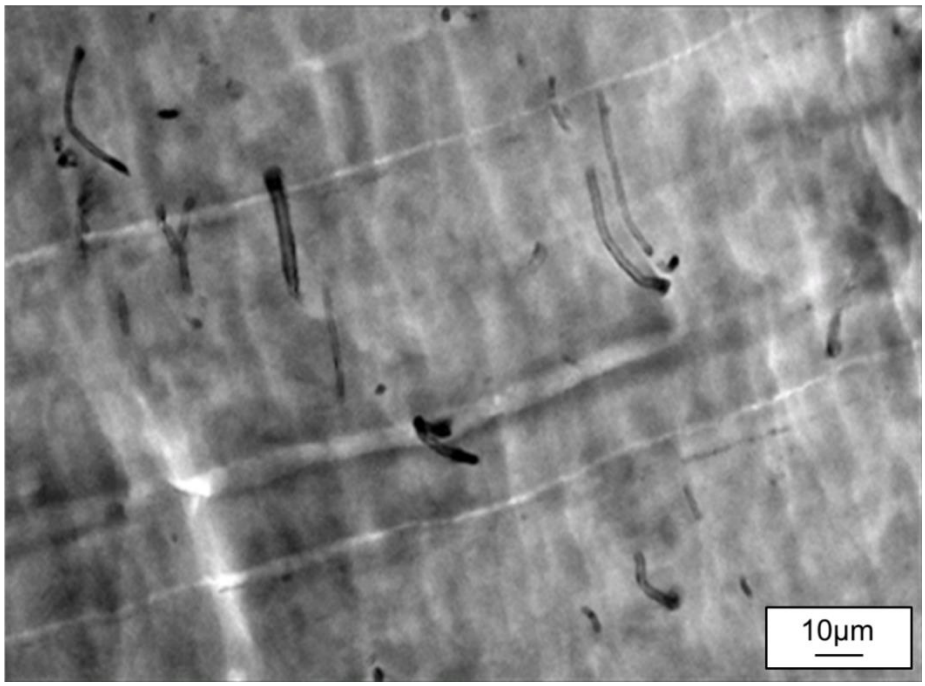

Figure 2.5: TEM image of HDPE/thick-silane treated CNF nanocomposites at 0.5 wt.% loading (T1-05).

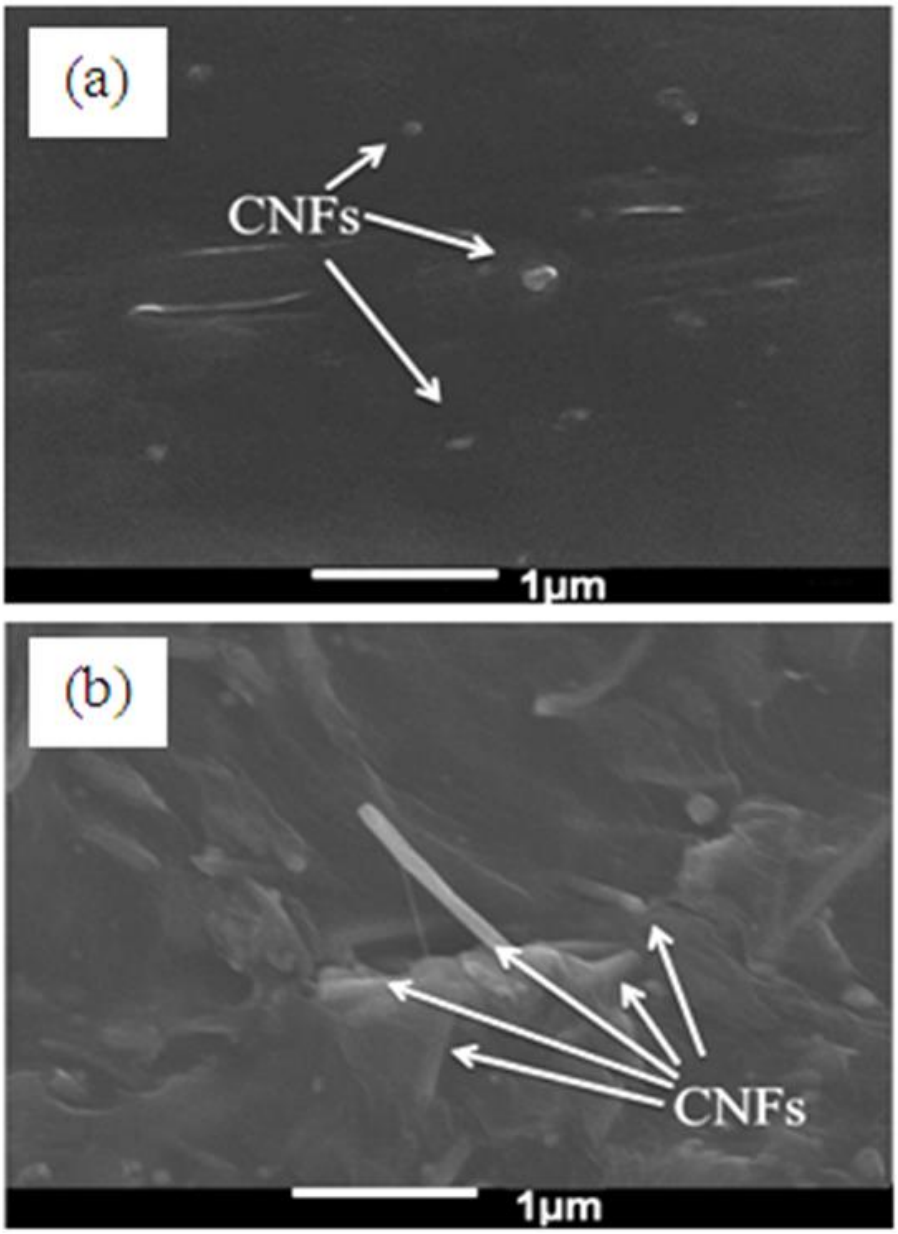

Figure 2.6: SEM micrographs of the worn surfaces: (a) is HDPE/thick-silane treated CNF nanocomposites at 0.5 wt.% loading (T1-05) and (b) is HDPE/pristine CNF nanocomposites at 3 wt.% loading (P-3).

2.3.2. Hardness

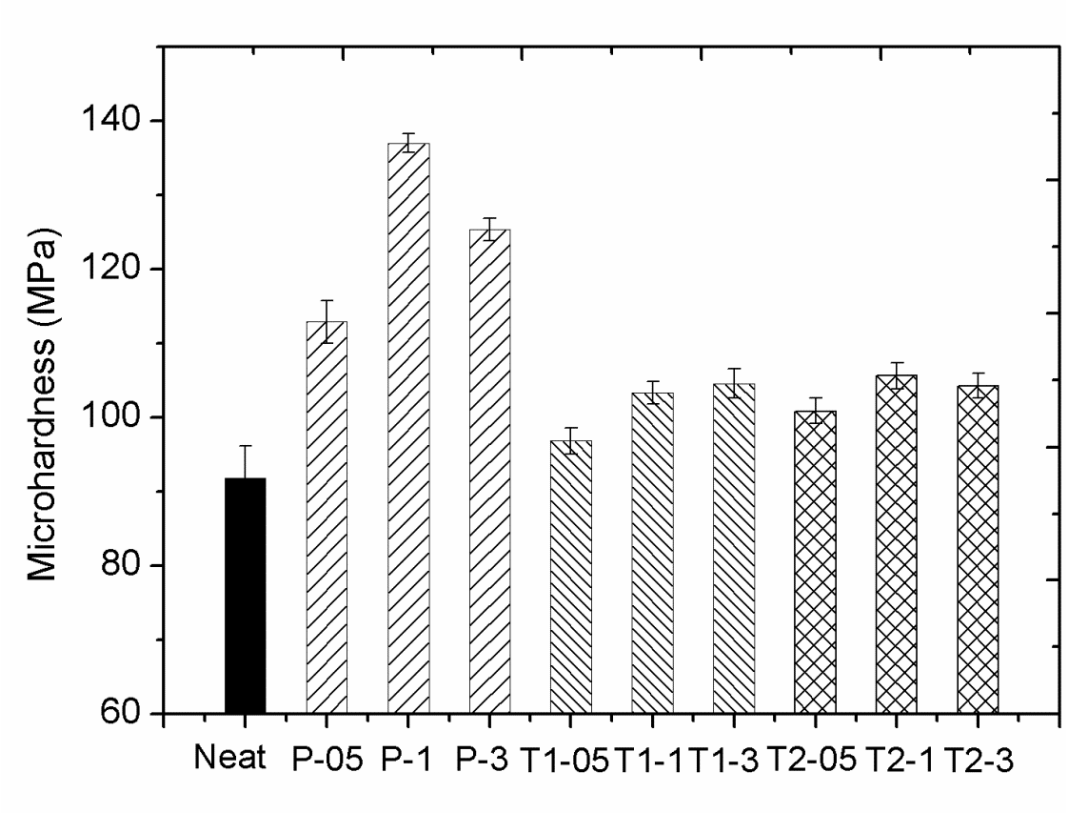

Figure 2.7: Comparison of microhardness values of ten samples; Neat: neat HDPE. P-05: HDPE with 0.5 wt.% of pristine CNFs. T1-05: HDPE with 0.5 wt.% of oxidized CNFs with thick silane coating (see Table 2.1).

The microhardness values of the ten types of samples are presented in Figure 2.7, nine of which are nanocomposites reinforced with three types of CNFs (see Table 2.1) and for each type, there are three concentration levels of CNFs, 0.5 wt.%, 1 wt.% and 3 wt.%. The nine nanocomposite samples uniformly had higher micro-hardness values compared to the neat HDPE. Statistical analysis of the significance in differences between the micro-hardness values was performed using SPSS. The ANOVA analysis showed significant differences between the groups (p-value<0.001), and then the Bonferroni multiple group comparisons were carried out. The Bonferroni results indicated that compared to the neat HDPE, the micro-hardness values of most nanocomposites samples were significantly different (higher) (p-values<0.001) with the exception of the HDPE nanocomposites with T1-CNF at 0.5 wt.% loading (p-value=0.654)

and HDPE nanocomposites with T2-CNF at 0.5 wt.% (p-value=0.003, which also indicated significant difference) samples. The different silane coating thickness did not have considerable influence on the microhardness of the nanocomposites. The samples enhanced with silane treated CNFs exhibited lower micro-hardness values than those with pristine CNFs. It was reported in Ref. [86] that the silane coating occurred as a crosslinking network structure; thus, it is speculated that such crosslinking network of the silane coating on the CNFs could result in more interfacial deformation between the CNFs and the HDPE matrix to make the composite more ductile compared to those reinforced with pristine CNFs.

2.3.3. Thermal conductivity

The thermal conductivity values of HDPE/CNF nanocomposites are compared in Figure 2.8. The addition of CNFs improved the thermal conductivity of the nanocomposites compared to the neat HDPE. The thermal conductivity of the nanocomposites increased with the increasing CNF loading level for all types of CNFs. This phenomenon could be due to two reasons: (1) CNFs can be viewed as heat conductors, and therefore, more CNFs meant more heat conductive components; (2) as the loading level increased, more CNFs could come in contact with each other and form partial heat conductive networks. These highly conductive paths could enormously contribute to the heat conductance of the nanocomposites [93].

In addition, Figure 2.8 shows that the thick-silane treatment effectively enhanced the thermal conductivity compared to the pristine and thin-silane treated CNFs. HDPE filled with thick-silane treated CNFs at 3 wt.% loading had the highest thermal conductivity among all nanocomposites, with an increase of 18% compared to that of pure HDPE. Besides the thermal conductivity of reinforcement, the thermal conductivity of composites depends strongly on secondary aspects such as the interface bonding between the fillers and matrix, distribution, geometry, and filler size [94-96]. First, the interfacial physical contact between the polymer matrix and the fillers plays a very critical role in the heat conductance of composites since the

transport of heat in all non-metals is by the flow of lattice vibration energy, or phonons, which are very sensitive to surface defects [97, 98]. The high thermal conductivity of thick-silane treated CNF filled HDPE was probably due to the fact that the surface treatment of CNFs with silane agent effectively improved the interfacial interaction.

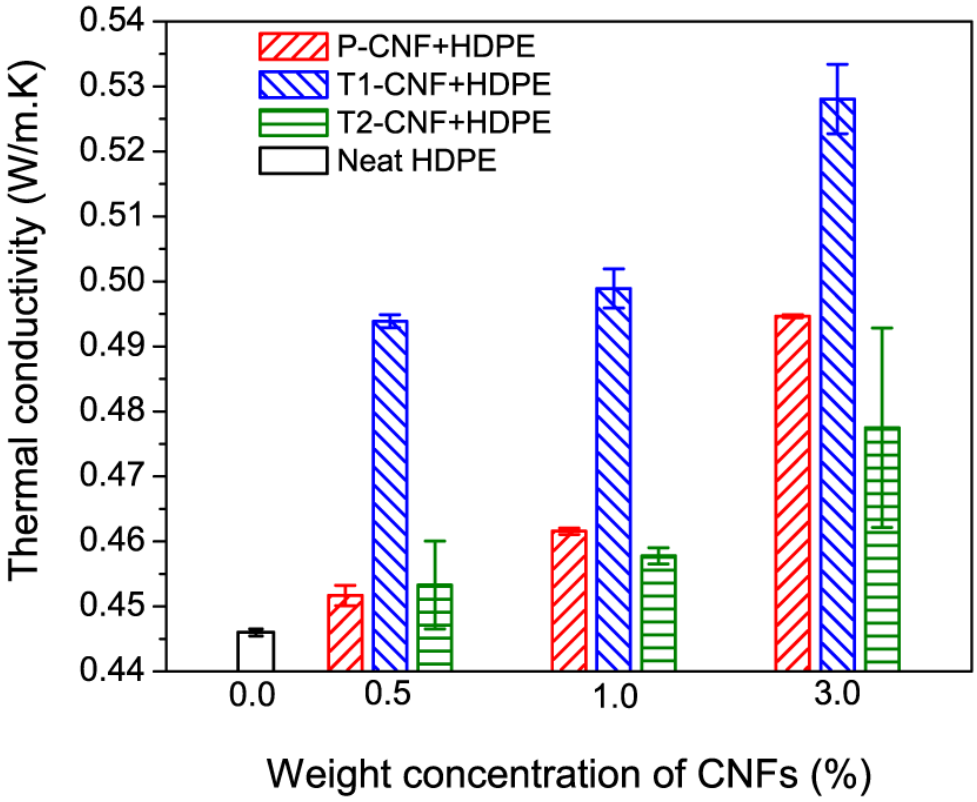

Figure 2.8: Thermal conductivity of neat HDPE, HDPE /pristine CNF, HDPE /silane treated CNF nanocomposites as a function of the weight concentration of CNFs.

The comparison of the degrees of fibers' pull-out between the different CNFs reinforced HDPE nanocomposites is illustrated in the SEM images of fracture morphology (Figure 2.9). For the nanocomposites with pristine CNF and thin-silane treated CNFs at 3 wt.% , there were some fiber pullout (Figure 2.9(a) and (b)). With same concentration, thick-silane treated CNFs result in almost no fiber exposed on the surface of matrix and few pull-out, as shown in Figure 2.9(c). These phenomena revealed that the interaction between the pristine

/thinner-silane treated CNFs and polymer matrix were not as strong as that of thick-silane treated CNF.

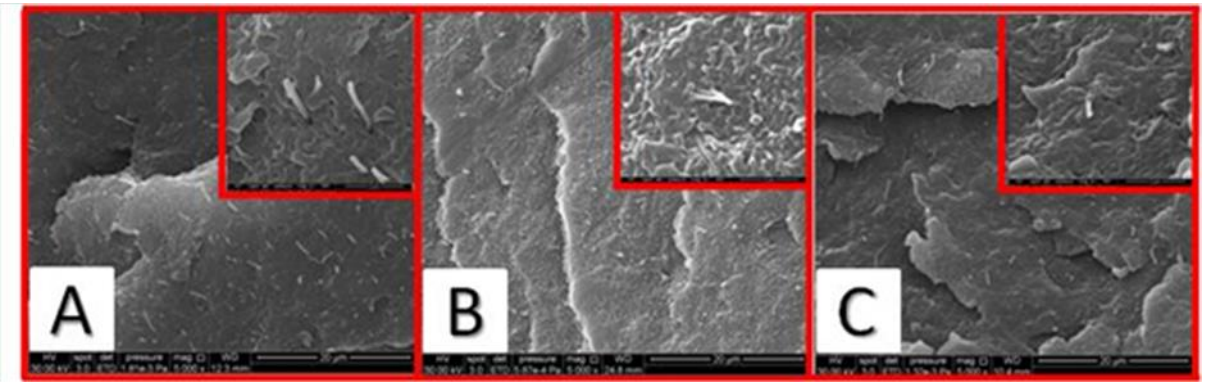

Figure 2.9: SEM micrographs (scale bar: 20 μm; insert: 2 μm) for the fracture surfaces of HDPE nanocomposites reinforced by CNF-P (A), CNF-T2 (B), and CNF-T1 (C). The fiber loading of all nanocomposites was 3 wt.%.

In addition, the thermal contact resistance between the CNFs and the HDPE matrix can be evaluated through the effective medium approach [87, 95, 99]. Assuming that the CNFs are randomly oriented, of equal size, and perfectly straight in an isotropic polymer matrix, this model takes into account the thermal conductivity of the components of nanocomposites, the aspect ratio and volume fraction of nanofillers, and the thermal resistance at the filler/matrix interface. According to the effective medium approach, the effective thermal conductivity k_{eff} of the nanofiber composites can be derived as [95]:

$$\frac{k_{eff}}{k_m} = \frac{3 + f(\beta_x + \beta_z)}{3 - f\beta_x} \tag{2.3}$$

where k_m is the thermal conductivity of the matrix, f is the volume fraction of the CNFs, and the terms β_x and β_z are given as:

$$\beta_x = \frac{2(k_{11} - k_m)}{k_{11} + k_m} \tag{2.4}$$

$$\beta_z = \frac{k_{33}}{k_m} - 1 \tag{2.5}$$

and

$$k_{11} = \frac{k_f}{1 + \frac{2ak_f}{dk_m}} \tag{2.6}$$

$$k_{33} = \frac{k_f}{1 + \frac{2ak_f}{lk_m}_z} \tag{2.7}$$

The parameters k_{11} and k_{33} represent the equivalent thermal conductivities of CNFs in the transverse and longitudinal directions in a nanocomposite unit cell, as illustrated by Nan et al. [95], k_f , *d*, and *l* are the thermal conductivity, diameter, and length of the CNFs, respectively, and the variable *a* is called Kapitza radius defined as:

$$a = R_c k_m \tag{2.8}$$

with R_c representing the interfacial thermal contact resistance between the CNFs and the HDPE matrix.

In this work, the measured thermal conductivity value of neat HDPE was used for k_m in Equation (2.3). The density of CNFs, HDPE, and silane coating was respectively taken as 1.95 g/cm^3, 0.954 g/cm^3, and 0.88 g/cm^3 to convert the weight percentage of CNF loading into volume percentage [28]. The converted results are listed in Table 2.1. The thermal conductivity of CNFs (Pyrograf®-III PR-24-HHT) was given by the manufacturer as 1750 W/m·K. The diameter of the CNFs used in the model was 100 nm, 105.6 nm, and 192 nm for pristine, thin-silane treated, and thick-silane treated CNFs, respectively. The length of the CNFs used was the average length of 65 μm.

Figure 2.10(a-c) shows the predicted effective thermal conductivity values of the three types of CNF reinforced HDPE nanocomposites at 0.5, 1 and 3 wt.% loading levels as a function of the interfacial thermal contact resistance R_c. Based on the measured thermal conductivity of each nanocomposite (the circle markers in each figure), the corresponding R_c of each nanocomposite can be estimated. The estimated R_c values are listed in Table 2.3. These

values are in good agreement with the range reported in nylon/11 CNF nanocomposites at 1 and 3 wt.% loading levels (2.5-5.0 × 10^{-6} m^2·K/W) [87]. The R_c values of CNFs can be different over several orders of magnitude depending on the polymer matrix, size, surface modification, surface roughness, etc. [87]. In comparison, the R_c values of vapor-grown CNF in polypropylene and polycarbonate matrix were reported by Macedo et al. [100] to be 4.6-5.0 × 10^{-7} m^2·K/W and 1.3 × 10^{-6} m^2·K/W, respectively. Hubmann [99] et al. estimated the R_c of vapor-graphitized and vapor-grown CNF in poly(ethylene glycol) matrix to be 15 × 10^{-8} m^2·K/W and 12 × 10^{-8} m^2·K/W.

Table 2.3: Summary of the thermal conductivity (k) and interfacial thermal contact resistance (R_c).

Material	k $(W/m \cdot K)$	R_c $(\times 10^{-6} m^2 K/W)$
Neat HDPE	0.446	-
0.5 wt.% P-CNF +HDPE	0.455	2.38
1wt.% P-CNF +HDPE	0.462	2.68
3 wt.% P-CNF +HDPE	0.495	2.75
0.5 wt.% T1-CNF +HDPE	0.494	0.88
1wt.% T1-CNF +HDPE	0.499	1.53
3 wt.% T1-CNF +HDPE	0.528	2.72
0.5 wt.% T2-CNF +HDPE	0.453	2.92
1wt.% T2-CNF +HDPE	0.458	3.57
3 wt.% T2-CNF +HDPE	0.477	3.89

As shown in Figure 2.10(d), the R_c values of the nanocomposites with thick-silane treated CNFs were lower than those with pristine and thin-silane treated CNFs at the same CNF volume fraction level. In particular, at 0.5 vol.% loading level, the R_c value of the

nanocomposite with thick-silane treated CNFs was at least 2.5 times lower than that of the nanocomposite with pristine CNFs. This verified that compared the pristine and thiner-silane treatment, the thicker-silane functionalization resulting in a stronger interaction between the CNF and HDPE matrix, gave a positive contribution to lower R_c. Therefore, the coupling of the nanofibers in the matrix molecules was improved and the heat transfer to the surrounding polymer material was facilitated. However, it was interesting that the thin-silane treated CNFs yielded a higher R_c value compared to the pristine CNFs, possibly because the thin-silane coating may only have the limited interaction of thin-silane treated CNFs with the polymer chains, but at the same time block the thermal conductive and have negative effect on the thermal conductivity between CNFs and HDPE matrix.

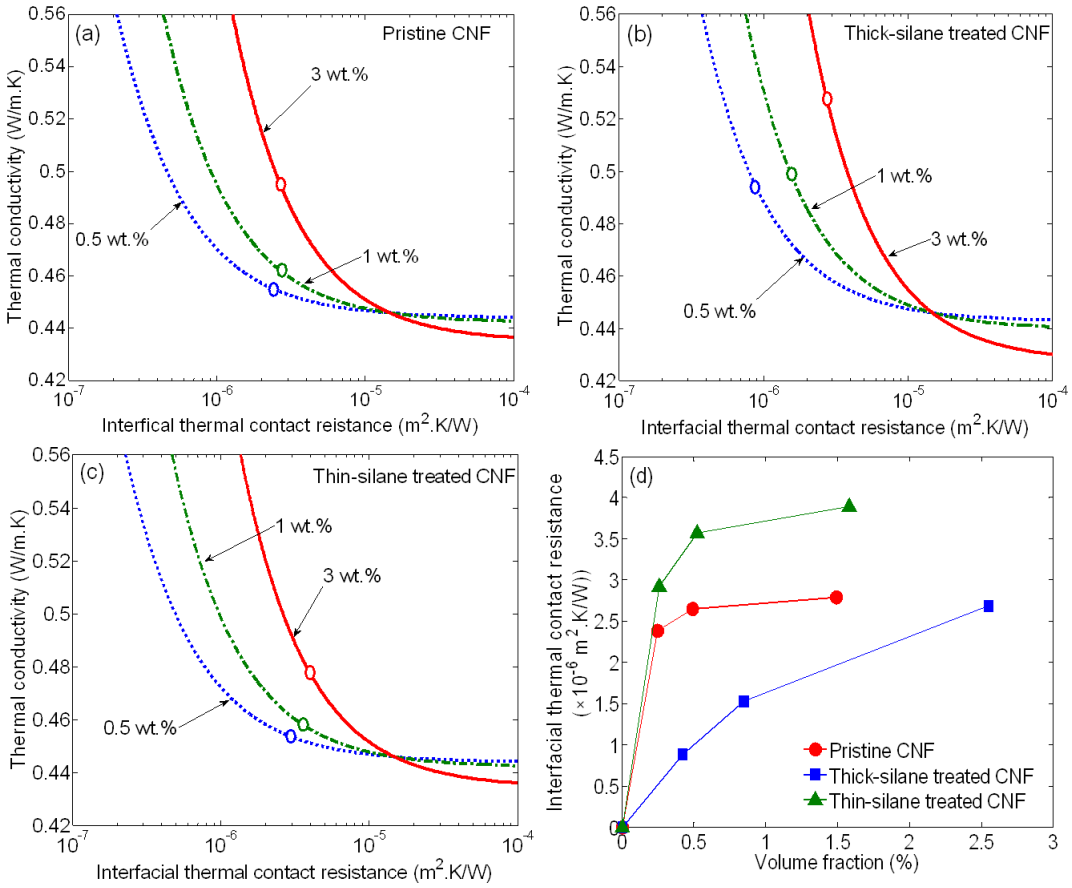

Figure 2.10: Model prediction of thermal conductivity for the (a) pristine CNF, (b) thick-silane treated CNF, (c) thin-silane treated CNF reinforced HDPE nanocomposites at loading levels of 0.5, 1 and 3 wt.% (the circles are the experimentally measured thermal conductivity of the corresponding nanocomposites), and (d) the comparison of evaluated interfacial thermal contact resistance of the nine nanocomposites as function of volume fraction of CNFs.

2.4. Conclusion

In summary, a series of experiments were performed to study the addition of CNFs and the functionlization of CNFs on the mechanical and thermal properties of HDPE/CNF nanocomposites. The addition of CNFs led to significant enhancement of the ultimate stress, strain at fracture, and hardness compared with the neat HDPE. As the CNF concentration increased, the Young's modulus and ultimate stress of the nanocomposites also increased as a result of the reinforcement effects of CNFs. The thermal conductivities of HDPE/CNF nanocomposites were all improved with the increase CNF loading. Thermal conductivity

measurements reflected that an 18% improvement in the nanocomposite reinforced with thick-silane treated CNFs at 3 wt.% loading was yielded. The results of this study have the potential to benefit the development of HDPE in tribological applications and the wear simulations in the latter studies.

CHAPTER 3. TRIBOLOGICAL BEHAVIOR OF CARBON NANOFIBER REINFORCED HIGH DENSITY POLYETHYLENE NANOCOMPOSITES

In this chapter, the coefficient of friction and wear rate of the nanocomposites under dry sliding, saline water lubricated and bovine serum lubricated conditions were reported. Compared with the neat HDPE, the friction coefficients of the nanocomposites were reduced in all samples under all three conditions. CNFs with thicker-silane coatings at low concentration levels, yielding the lowest wear rate in all three conditions, have the potential to serve as promising reinforcements for HDPE to achieve improved tribological property of the nanocomposites. In addition, the relationships between the wear rate and the mechanical properties of the nanocomposites such as the hardness and tensile properties were discussed.

3.1. Introduction

As reviewed in Chapter 1, HDPE has been used as a bearing material both in industrial and biomedical applications because of its low cost, low friction, good resistance to wear and to chemical attacks, and good biocompatibility [20, 23]. The incorporation of nano-reinforcement into the polymer matrix is found to be an effective way for improving mechanical and tribological properties while maintaining the toughness of the polymer [28]. HDPE-based nanocomposites have good processability due to the low viscosity of HDPE at elevated temperatures compared to UHMWPE. Results obtained from studying HDPE nanocomposites may have potential implications and contributions to the study of UHMWPE nanocomposites. Many studies have been dedicated to the use of HDPE nanocomposites as bearing materials in industry and biomedical applications. [6, 35-37, 51, 52]. Wood et al. [6, 86] successfully produced silane-treated oxidized CNFs with different silane coating thicknesses as nanofillers for HDPE, and found that the thick-silane coated CNFs (thickness of 46 nm) had improved interaction with HDPE. Liu et al. [16] studied the correlation of wear

effects with dielectric properties of silane treated CNF reinforced HDPE composites. However, the tribological properties of HDPE/CNF nanocomposites and their wear mechanism have not been specifically reported in literature so far. In this chapter, the tribological behavior of HDPE/CNF nanocomposites under dry sliding, saline water, and bovine serum lubricated conditions are investigated.

3.2. Test methods

3.2.1. Pin-on-disc wear test

The wear and friction tests were performed using a pin-on-disc tribometer (CETR-UMT2) (see Figure 2.2). The schematic of the pin-on-disc wear test is shown in Figure 3.1. Though for applications in artificial joints, a multidirectional wear simulator, such as a hip simulator, would provide a more realistic pattern of motion, for preliminary study of the material's wear properties, the pin-on-disc tribometer has been widely used as an acceptable testing device in the literature [32–39]. The stainless steel balls (SS440 Grade 25) with diameter of 4.762 mm (3/16 in.) and surface roughness of 0.51 μm (2 micro in.) from Salem Specialty Ball, Inc. were used. The normal load, sliding speed, and test duration were set at 30N, 1 rpm, and 8 hour, respectively. Each test specimen was a 1 in. ×1 in. and the diameter of the wear track was set as 10 mm. The specimens were carefully cleaned and dried in an autoclave at 65 °C for at least 8 hours before the wear test. The tangential force and normal load were recorded by the tribometer directly during the wear process, from which the coefficient of friction (COF) was calculated. The wear tests were performed in three conditions: dry sliding, saline water lubricated condition, and bovine serum lubricated condition. The friction and wear tests were repeated at least four times for each material and each wear condition.

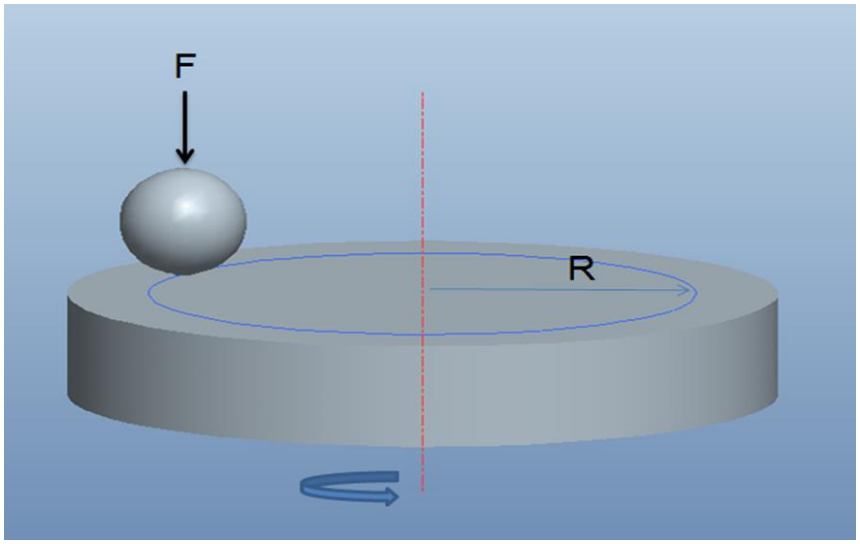

Figure 3.1: Schematic of a pin-on-disc wear test.

For the wear tests under lubricated conditions, a lubricant holder was designed to contain different lubricants as shown in Figure 3.2. When the wear test was conducted, the sliding surface between the ball and polymer disc was fully immersed in the lubricants. The phosphate buffered saline water was from Thermo Fisher Scientific Inc. with PH 7.4. The bovine serum was purchased from Hyclone Laboratories, Logan, UT (100% serum = approximately 34 mg/mL total protein). Based on ASTM F732, the serum is diluted with de-ionized water of up to 75 vol.%. The diluted serum was filtered through a filter of 0.2 µm mesh size to remove any hard, abrasive, and particulate contaminants. 0.25 wt.% sodium azide and 7.45 g/L ethylenediaminetetraacetic acid (EDTA) were added into the serum lubricants to retard any possible bacterial degradation, and to minimize the precipitation of calcium phosphate onto the bearing surface, respectively. During the wear test, the bovine serum was replenished periodically by adding the right amount of de-ionized water up to the original volume.

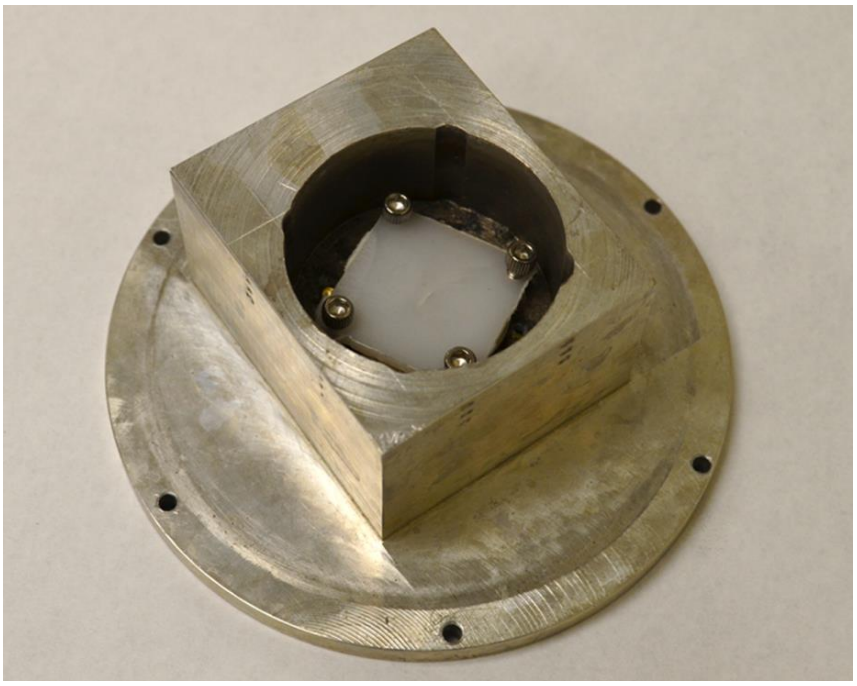

Figure 3.2: A photo of lubricant holder for the pin-on-disc wear test.

3.2.2. Measurements of wear loss

Volume-based measurement. For the wear test under dry sliding condition, the wear loss is evaluated with volume-based measurement. After each dry sliding wear test, the sample was shelved in oven at 80 °C for at least two weeks to remove the water absorption and potential viscoelastic deformation. Contact profilometer (P-15 Longscan Stylus) was then used to measure the geometry of the cross-section of the wear track at 8 evenly distributed locations for each sample as shown in Figure 3.3.

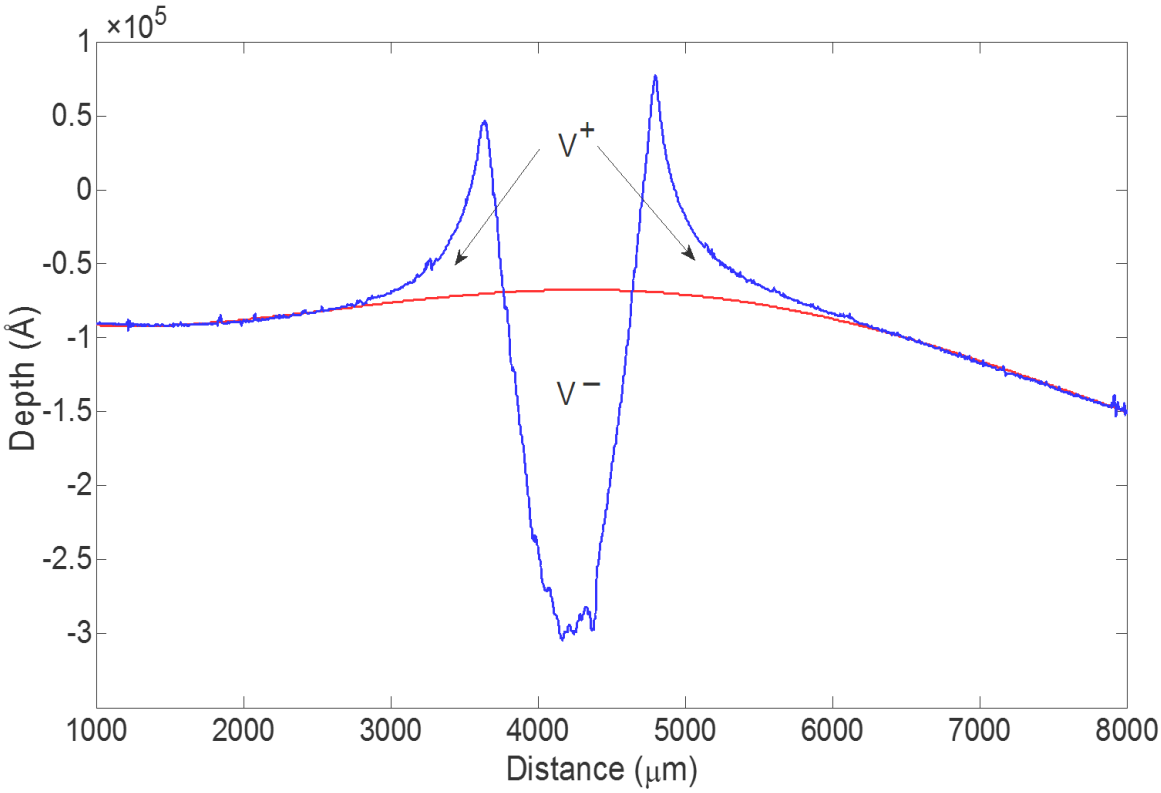

Figure 3.3: Schematic of contact profile of the wear track.

The wear volume loss (ΔV, mm^3), defined as the difference between the grooved volume, V^- and the pile-up volume, V^+, was calculated from the circumference and the measured average cross-sectional area of the track [101, 102]. In calculating the cross-sectional area, the curvature of the surface was taken into account by approximating the surface by a polynomial shown in Figure 3.3 in smooth solid line and then integrating it to obtain the total area. Such geometry-based wear volume calculation was also used in the tribological study of UHMWPE in [102, 103]. The wear rate was determined using the following equation:

$$W = \frac{\Delta V}{T} \tag{3.1}$$

where W is the wear rate, ΔV is the wear volume, and T is the time of wear.

Mass-based measurement. For the wear tests under dry sliding and bovine serum lubricated condition, the mass-based measurement is used for the assessment of wear loss.

Before and after wear test, the specimens were all carefully cleaned and dried in an autoclave at 65 °C for at least 8 hours, and then the weight of each specimen was measured using a digital scale with an accuracy of 0.1 mg. The mass loss during the wear test thus can be obtained.

The specific wear rate (SWR), which is defined as the wear volume per unit distance and unit load [104], can be used to evaluate the wear resistance of the materials. The lower the specific wear rate, the better the wear resistance. The specific wear rate can be determined using the following equation [5, 6]:

$$W = \frac{\Delta V}{NL} = \frac{\Delta m}{\rho NL} \tag{3.2}$$

where W is the specific wear rate, ΔV is the wear volume (mm^3), N is the normal force (N), and L is the sliding distance (m). The wear volume ΔV can further be expressed as $\Delta m/\rho$, where Δm is the mass loss and ρ is the density of the material.

3.2.3. Biocompatibility test

MC3T3 cells (a mouse osteoblast precursor cell line) were cultured in alpha minimum essential medium containing 10% fasting blood sugar, 50 U/ml penicillin and 50 U/ml streptomycin. The medium was refreshed every 2 days and the cells were incubated in a tissue culture incubator at 37 °C with 5% CO_2. After reaching about 80% confluence, the cells were detached by 0.25% trypsin. The plates of samples were sterilized by 75% ethanol and a separate culture dish without any sample was used as the control. A density of 3×10^5 cell/ml was seeded in the Corning Costar 6-well cell culture dishes containing the samples (Neat, P-3, and T1-05) as well as the control dish for cell growth assay and microscopy observation. Cell numbers in each culture dish were counted using Auto T4 Nexcelom Cellometer on the initial time and after 3, 4, and 5 days, respectively, based on which the cell proliferation is monitored. Cells growing on the bottom of culture dishes were observed after 4 days using a Leica DM IL

inverted microscope, and the cells growing on the samples were viewed through an Axiovert 40 Mat optical microscope.

3.3. Results and discussion

3.3.1. Tribological behavior of HDPE/CNF under dry sliding condition

Coefficient of friction. In Figure 3.4, the COFs of all samples changed drastically during the earlier stage of sliding up to 1000 s, and then slowly reached a relatively steady state after about 12500 s. With the addition of CNFs, both pristine and silane-treated, the COFs of the nanocomposites were all lower than that of the neat HDPE. Graphite possesses self-lubricating and dry lubricating properties due to the loose interlamellar coupling between the planes of polycyclic carbon atoms in the structure [105]. For that reason, the addition of CNFs might decrease the COF of HDPE/CNFs nanocomposites due to their layered graphitic structures.

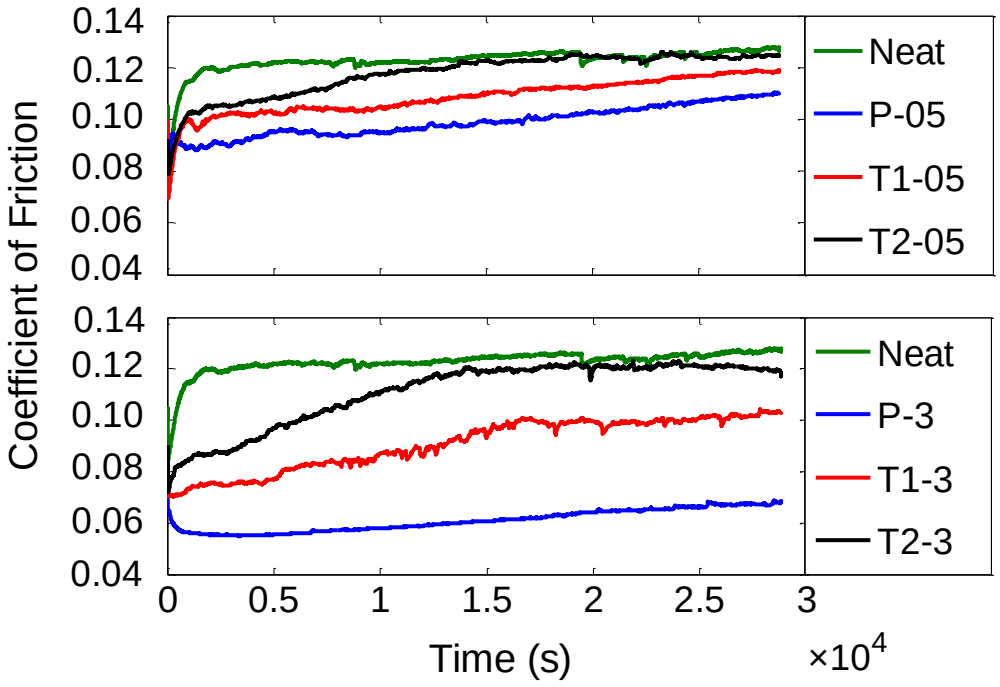

Figure 3.4: Variations of the coefficients of friction over time.

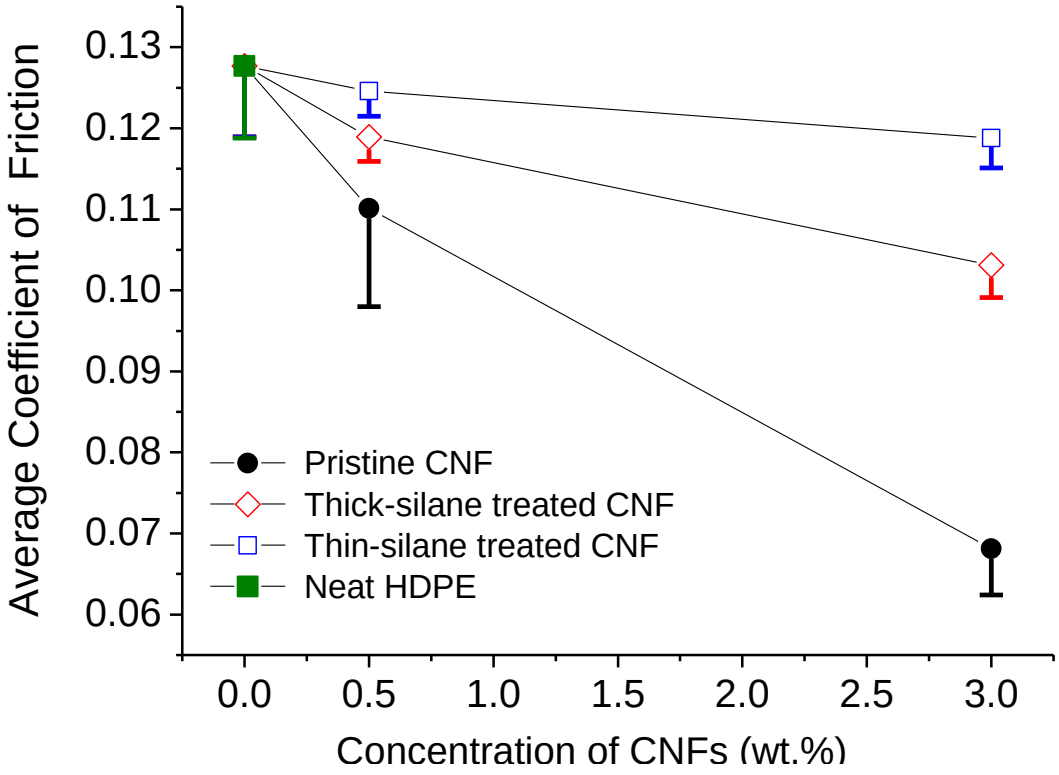

Figure 3.5: Comparison of the coefficients of friction of the seven materials under dry sliding condition.

The average COFs of the samples at steady state (after 12500 s) are summarized in Figure 3.5. Only half of the error bars of the results were shown in the figure for a clearer presentation. For each type of CNFs (pristine, thick or thin silane coated), the nanocomposites with higher concentrations of CNFs yielded lower COFs. The COFs of the nanocomposites with silane-treated CNFs were higher than those with pristine CNFs at the same concentration level. This may be because after the wear debris that contain CNFs were worn off, the silane coating on CNF might inhibit the formation of carbon film from the layer-by-layer graphite structure of CNFs at the interface of the two rubbing materials.

The COF between any two materials depends on many system parameters such as the temperature, geometric and material properties of the contact surfaces. Any subtle variation in those parameters might lead to unstable measurements of the COF, especially during a long sliding duration. Moreover, the COF measurement of polymeric material can be even more

complicated because the large plastic deformation might occur at the tips of the asperities and the geometric conditions around the tips could easily change [106]. Therefore, some relatively large standard deviations were observed in the COF measurements of samples such as the Neat, P-05 and P-3. However, even with the consideration of these relatively large standard deviations, the addition of CNF can be regarded as being effective in decreasing the COFs of the HDPE nanocomposites.

Wear resistance. The SWRs of the seven materials are illustrated in Figure 3.6. The HDPE nanocomposite enhanced with 0.5 wt.% of thicker-silane treated CNFs (T1-05), yielded the lowest wear rate, and compared to the neat HDPE, its wear resistance was enhanced by almost 68%. Moreover, compared to the neat HDPE and other nanocomposites with the same CNF concentration of 3 wt.%, the T1-3 nanocomposite had the lowest wear rate. Therefore, the thick silane-treated CNFs seemed to be more effective in improving the wear resistance of the nanocomposites compared with pristine CNFs and those treated with thin silane coatings. It was believed that a thicker silane coating might result in a stronger interaction between the CNFs and the matrix and functioned as a transition zone to transfer load from the polymer matrix to the nanoreinforcement better, compared to the pristine and thinner-silane treated CNFs [86].

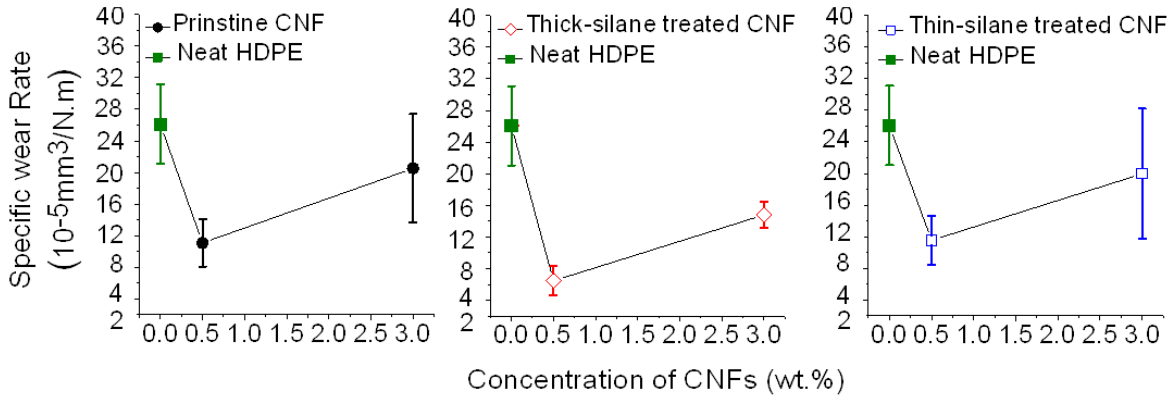

Figure 3.6: Comparison of the specific wear rates of the seven materials.

The effect of CNFs concentration on wear rates of the nanocomposites can also be discussed through Figure 3.6. The nanocomposites with the three types of CNFs at a low concentration of 0.5 wt.% all showed decreased wear rates compared to that of the neat HDPE; however, with the concentrations of CNFs increasing to 3 wt.%, the wear rate also increased. From the COF results, it would be expected that the nanocomposites at 3 wt.% CNFs loading, which have lower COFs, would yield lower wear rates, since in general the lower the COFs are, the lower the shear stresses would be on the sample surfaces. To explain this phenomenon, the microstructures of the worn surfaces of T1-05 and P-3 were needed. The CNFs on the surface of T1-05 have a good dispersion in the HDPE matrix in Figure 2.5. However, the CNFs in P-3 were more inclined to aggregate, shown in Figure 2.6(b). It is speculated that the increased wear rates of the nanocomposites with higher concentration of CNFs were due to such small aggregates of the nanofibers which affected the dispersion of CNFs and decreased their reinforcement effect on the matrix. Furthermore, wear debris that contained these aggregates of CNFs could work as hard abrasive grains in third-body abrasive wear, thus removing more material from the worn surface [5].

Wear mechanism. The worn surfaces and wear debris of the samples were observed by an optical microscope. Figure 3.7 shows optical micrographs of the wear tracks (a, c, e) and wear debris (b, d, and f) from the three samples (Neat, T1-05, and P-3) in which the T1-05 and P-3 had the lowest and the highest SWR, respectively. The wear track of the neat HDPE exhibited areas of deep pits in Figure 3.7(a). It is speculated that these pits began with small cracks transverse to the sliding direction due to repeated stressing and unstressing of the shear force, and eventually the subsurface over the micro-crack was exfoliated out. These deep pits indicated a larger component of fatigue wear. The wear track of T1-05 possessed the smoothest surface and, compared with the deep pits of the neat HDPE, showed smaller and shallower defects transverse to the sliding direction, as shown in Figure 3.7(c). This suggests that the

major wear mechanism in T1-05 may have been fatigue wear, same as the neat HDPE. However, the fatigue wear in T1-05 has a lesser degree, because the pits in T1-05 are shallower and smaller than that of the neat HDPE. It was believed that CNFs could resist the nucleation of cracks by acting as stress-transfer "bridges" and even if the cracks were nucleated, CNFs could block the crack from propagating further [107]. Therefore, these smaller and shallower defects of T1-05 indicated the large contribution of silanized CNFs to the nucleation and propagation of micro-crack in the fatigue wear. However, with much more CNFs, P-3 exhibited worse wear with wider and deeper scratching grooves on the wear track in Figure 3.7(e). Such scratching grooves are typical of the abrasive wear mechanism. Although the worn surfaces of all specimens had some abrasive wear patterns, the scratching grooves, P-3 obviously exhibited the most severe abrasive wear, making abrasive wear its primary wear mode. The potential reason for the severe abrasive wear of P-3 may be P-3 have lower work of fracture compared to the neat HDPE and T1-05. The lower work of fracture indicates a lower toughness. The toughness may pay an important role in the wear of polymer which will be discussed in Section 3.3.3.

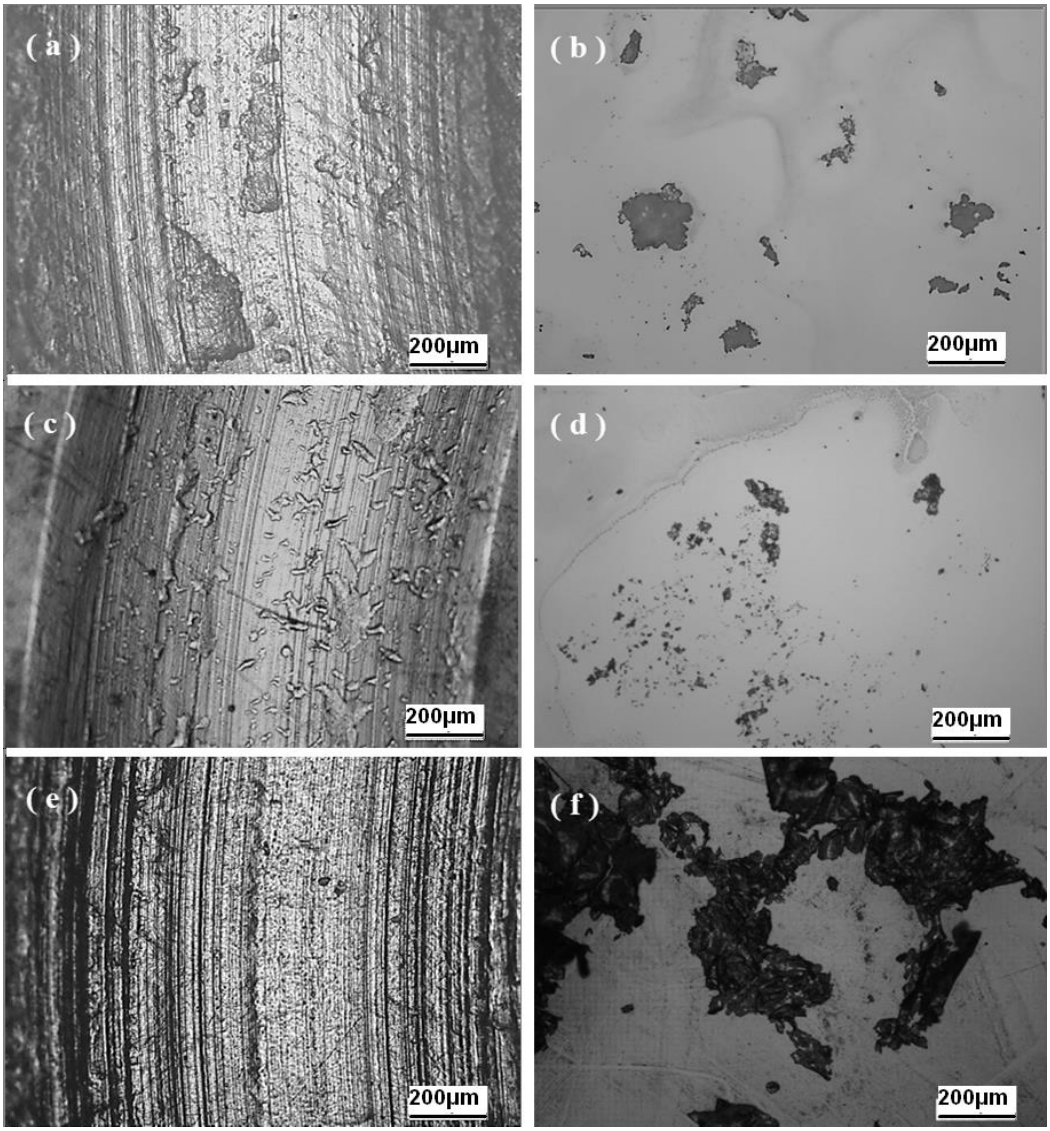

Figure 3.7: Optical microscopy of the worn surfaces and wear debris of three materials: Neat HDPE (a and b), T1-05 (c and d), and P-3 (e and f).

The wear debris of neat HDPE and T1-05 showed comparable flake shapes in Figure 3.7(b) and 3.7(d). Obviously, T1-05 produced smaller debris compared with the neat HDPE. This phenomenon was consistent with the smaller and shallower defects on the worn surface in Figure 3.7(c). However, the debris from P-3 was observed to be very large flakes in Figure 3.7(f), possibly due to the severe abrasive wear during which the exfoliated debris from each scratching groove aggregated or linked together. The wear modes of the neat HDPE, T1-05 and P-3 are further illustrated in Figure. 3.8. In Figure 3.8(a), the micro-cracks is generated in the neat HDPE sample under the cyclic strain followed with the relatively big wear debris

exfoliated out, and leave the deep pits on the wear track. However, due to the resistance of CNFs to the nucleation and extension of cracks, the second mode of Figure 3.8(b) occur to the T1-05, presenting shallow pits and tiny wear debris. But the more CNFs results in the lowest ductility of P-3, the severe abrasive wear as shown in Figure 3.8(c) happened, with the formation of large flake-shaped wear debris.

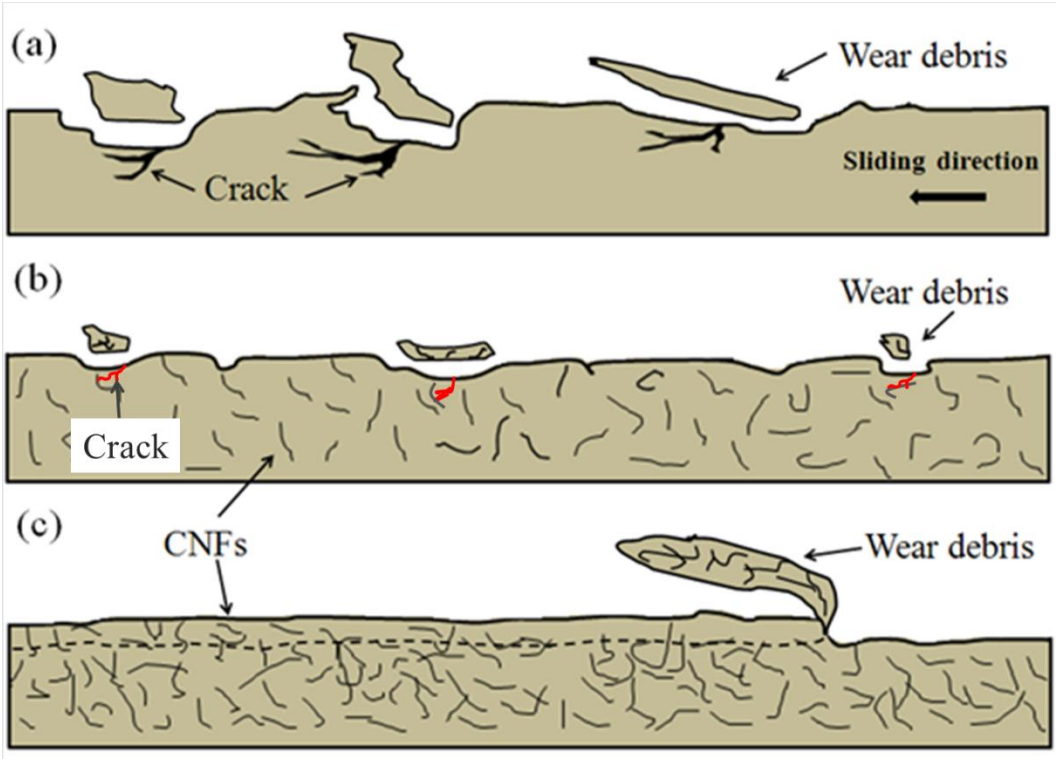

Figure 3.8: Illustrations of the wear mechanisms of (a) Neat HDPE, (b) T1-05, and (c) P-3.

3.3.2. Tribological behavior of HDPE/CNF under saline water lubricated condition

Coefficient of friction. The variations of COF of the ten types of samples during the saline water lubricated wear tests are presented in Figure 3.9 and Figure 3.10. In each test, the COF had a running-in period during which its value changed drastically compared to the latter stable stage; after approximately 5000s, it reached a relatively stable stage. Such trend was also observed in Zhang's work [108], where the COF of polyimide/short carbon fiber composites

against stainless steel reached the steady-state after 4800 s in dry sliding using a ring-on-block wear tester. It was believed that the wear debris formed during the running-in period were compacted and transferred onto the friction surface that worked as an extra lubrication layer and thus lowering the COF in steady-state [108]. Similarly, during the wear tests that we conducted in saline lubricated condition, part of the wear debris might also be compacted on the wear track to result in the running-in period, while the rest was dispersed into the saline solution.

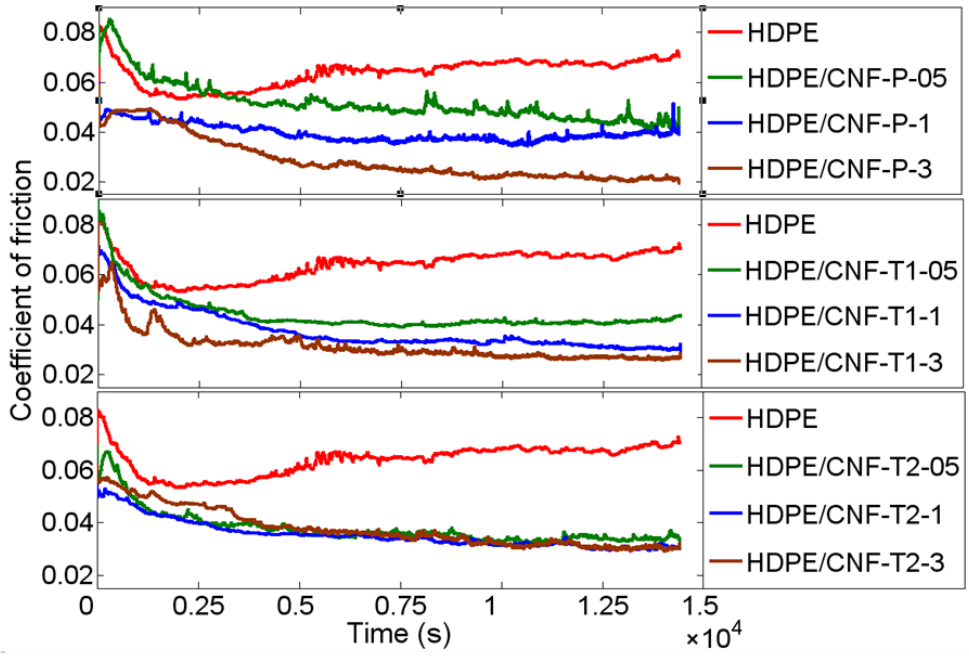

Figure 3.9: Variation of the coefficients of friction over time for the comparison of different CNFs concentration.

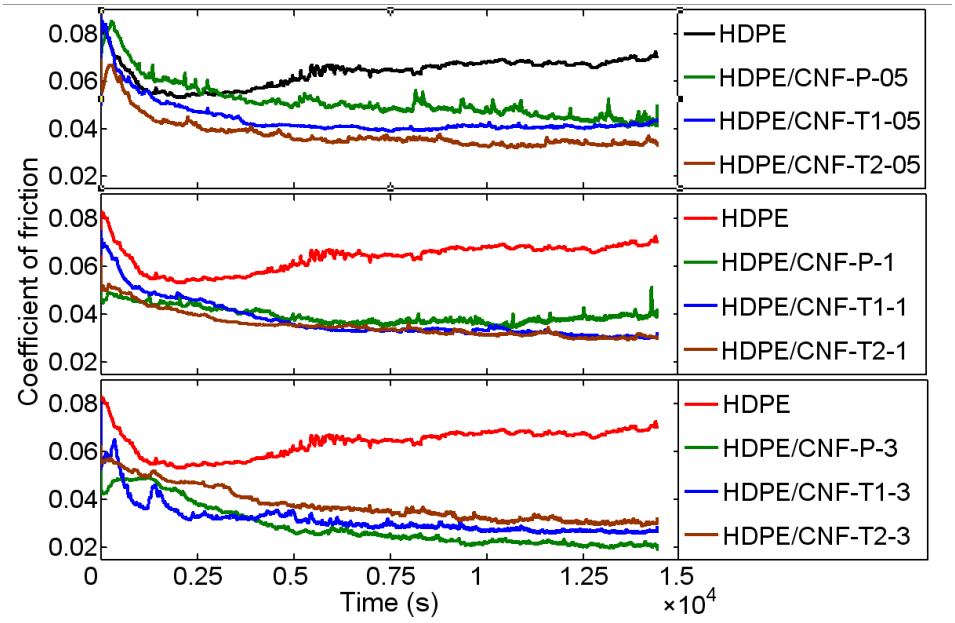

Figure 3.10: Variation of the coefficients of friction over time for the comparison of different CNFs treatment.

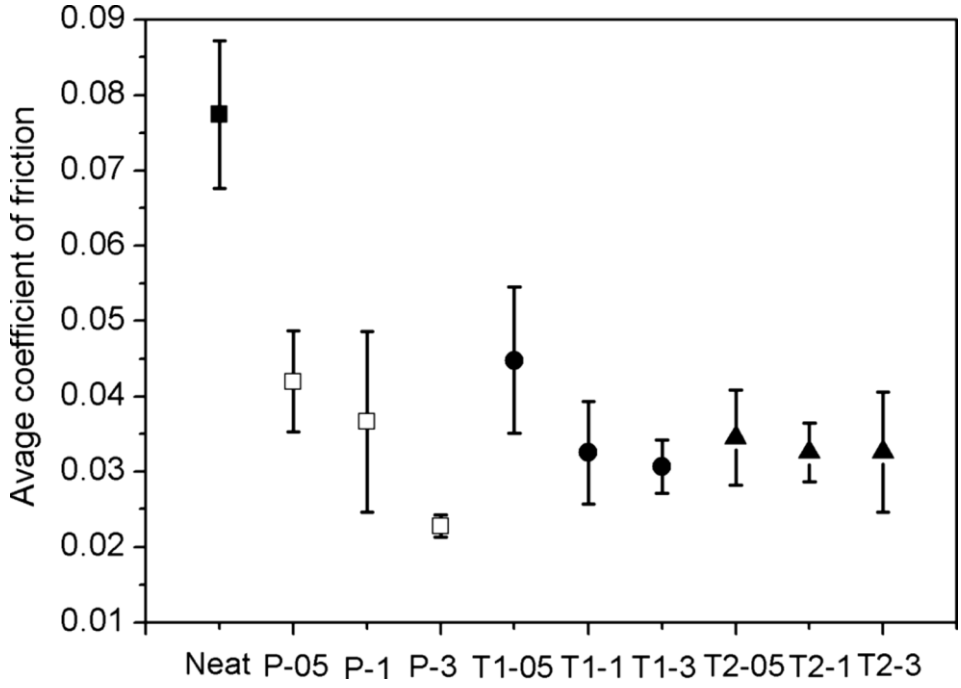

Figure 3.11: Coefficient of friction of the ten samples in contact with steel ball in saline lubricated condition (See Table 2.1 for notation of the sample names).

The average values of COF of the samples at steady stage (after 5000 seconds) are compared in Figure 3.11. With the addition of CNFs, both pristine and silane-treated, the average COF of nanocomposites is decreased compared to that of the neat HDPE. Bonferroni multiple group comparisons also indicated significant differences between the results (p-values < 0.001).

Wear resistance. The wear rate of the ten samples were determined using Equation 3.2. The wear rate of HDPE/CNF-T1 nanocomposites at 0.5 wt.% and 1 wt.% loading levels was lower than that of the neat HDPE by approximately 35% and 29%, respectively. Other nanocomposite samples, however, yielded higher wear rate than the neat HDPE. Particularly, the samples with pristine CNFs at all three loading levels had the highest wear rate among samples with the same loading level of CNFs. Bonferroni multiple group comparison analysis showed that compared to the neat HDPE, the wear rate of most nanocomposites was not significantly different (p-values = 1) except for the three samples that had obviously higher wear rate, HDPE/CNF-P1, CNF-P3 and CNF-T2-3. For the three groups of nanocomposites, there was a general trend that the wear rate increased as the loading level of CNFs became higher. The samples with 3 wt.% CNFs in all three groups exhibited much higher wear rate compared to those with lower CNF loading levels. Higher concentration of CNFs is more likely to result in small aggregates, even though the big agglomerates were not obviously seen in the SEM images (Figure 2.6). The small aggregates may reduce the mechanical properties of the nanocomposite. It has been reported that the tensile strength and modulus of nanocomposites with 3 wt.% CNFs were significantly lower than those with 1 wt.% CNFs [62, 109]. Moreover, the aggregates of CNFs may work as abrasive grains in third-body abrasive wear [46] and thus increase the overall wear rate of the material.

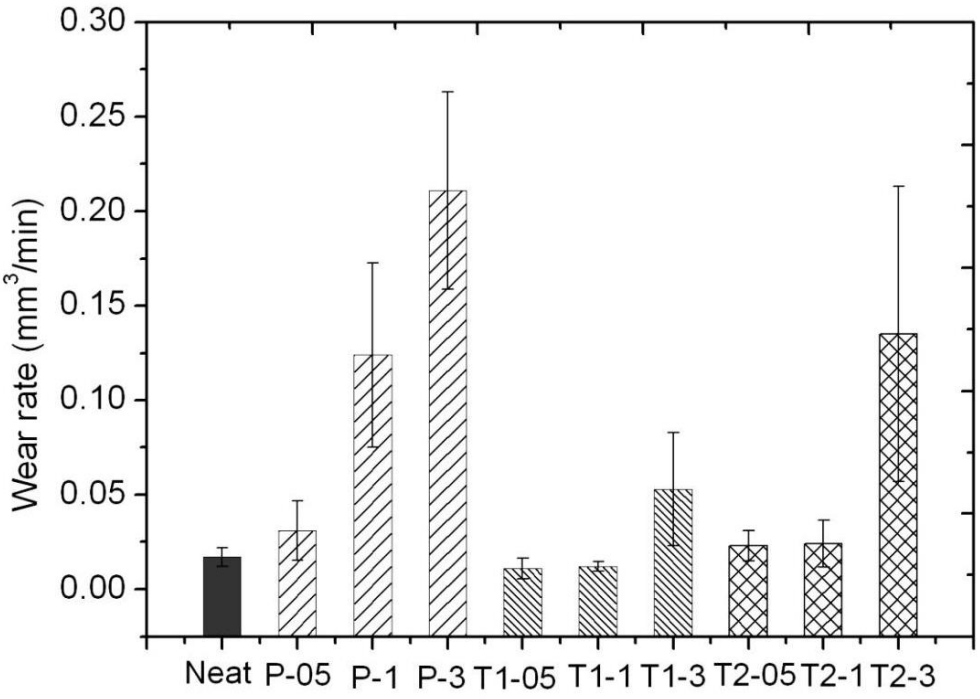

Figure 3. 12: Comparison of the wear rate of the ten samples.

Wear rate vs. hardness. A number of models have been proposed to relate the wear resistance of polymeric materials to micro-hardness [12, 64]. For example, famous Archad's wear law presented in the Ref. of [12, 75] indicated that the wear rate was inversely proportional to the micro-hardness of the material, especially in the case of abrasive wear. However, the opposite was observed for the nine types of nanocomposites here. With the same CNF loading level, the HDPE with pristine CNFs had higher micro-hardness (Figure 2.7) and also higher wear rate (Figure 3.12) than the HDPE with silane treated CNFs. It is noted that Archad's law is proposed to the wear of metal under dry sliding condition. For the wear of polymer, the material properties such as the work of fracture, and the product of the ultimate stress and strain at fracture may play much important role compared to the hardness [51]. This point will be further addressed in the next Section 3.3.3.

3.3.3. Tribological behavior of HDPE/CNF under bovine serum lubricated condition

Coefficient of friction. The COF for each material was tested under the bovine serum lubricated condition and the averages of repeated tests are reported in Figure 3.13. The COFs of neat HDPE and HDPE/CNF nanocomposites fell in the range of 0.045-0.085. The addition of CNFs all resulted in decreased COFs compared with the neat HDPE. Figure 3.14 shows the change in COF of different materials as a function of time. As shown in Figure 3.14(a) and Figure 3.14(b), the COF value of T1-05 and T1-3 are lower than that of neat HDPE and other composites with pristine CNFs and thin-silane CNFs, after the results reached steady state at roughly 5000 s. Compared with other CNFs, such as pristine CNFs and thin-silane treated CNFs, the thick-silane treated CNFs were more effective in reducing the COFs of HDPE/CNF nanocomposites. In addition, the variation of the COF of thick-silane treated CNF reinforced HDPE over time appeared more stable.

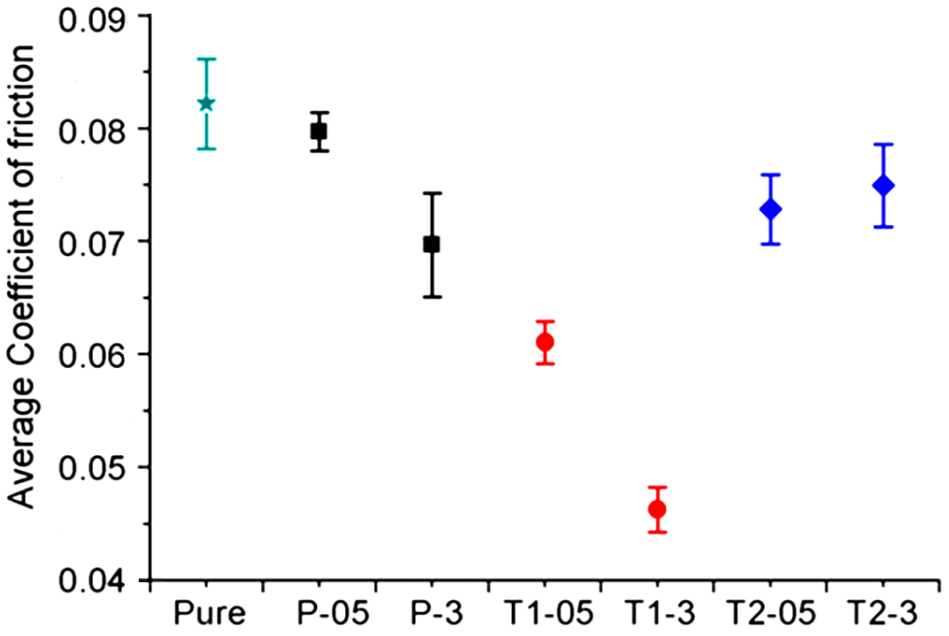

Figure 3.13: Coefficient of friction of the seven materials in contact with steel ball in bovine serum lubricated condition.

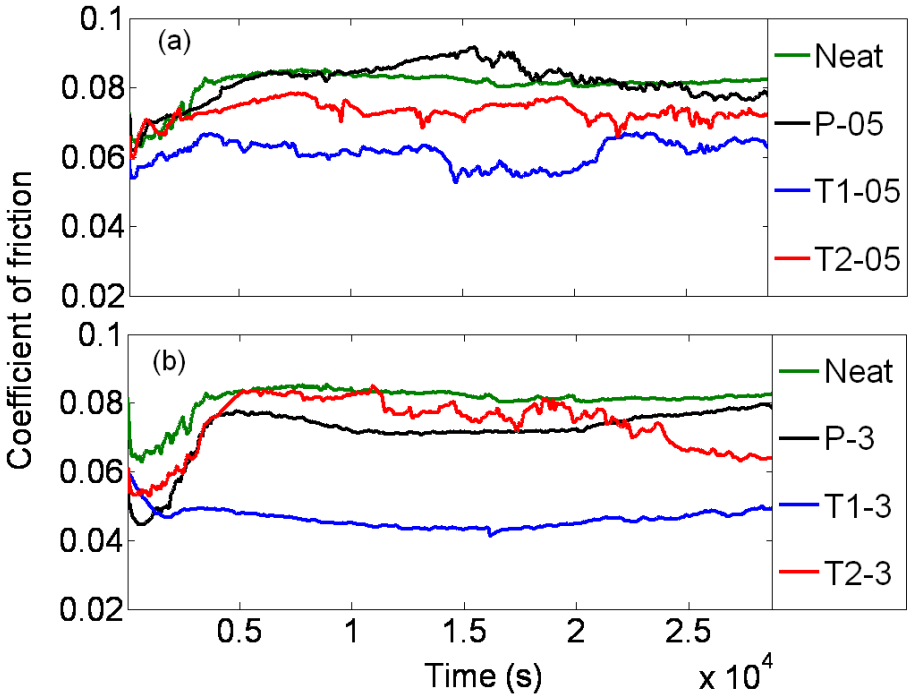

Figure 3.14: Comparison of the effect of silane treatment of CNFs on coefficient of friction with the CNF concentration at (a) 0.5 wt.% and (b) 3 wt.%.

Wear resistance. The specific wear rate of the neat HDPE and HDPE/CNF nanocomposites from the bovine serum lubricated pin-on-disk wear tests is illustrated in Figure 3.15. The nanocomposites had lower wear rates than that of the neat HDPE. As the concentration of CNFs increased from 0.5 wt.% to 3 wt.%, the specific wear rate increased. The thick-silane treated CNF reinforced HDPE at 0.5 wt.% loading level (T1-05) had the lowest wear rate, and the wear resistance of T1-05 was significantly improved by 57.9%, compared to the neat HDPE. The thick-silane treated CNFs was more effective in reducing the wear loss of the nanocomposites under bovine serum lubricated condition compared with the pristine and thin-silane treated CNFs.

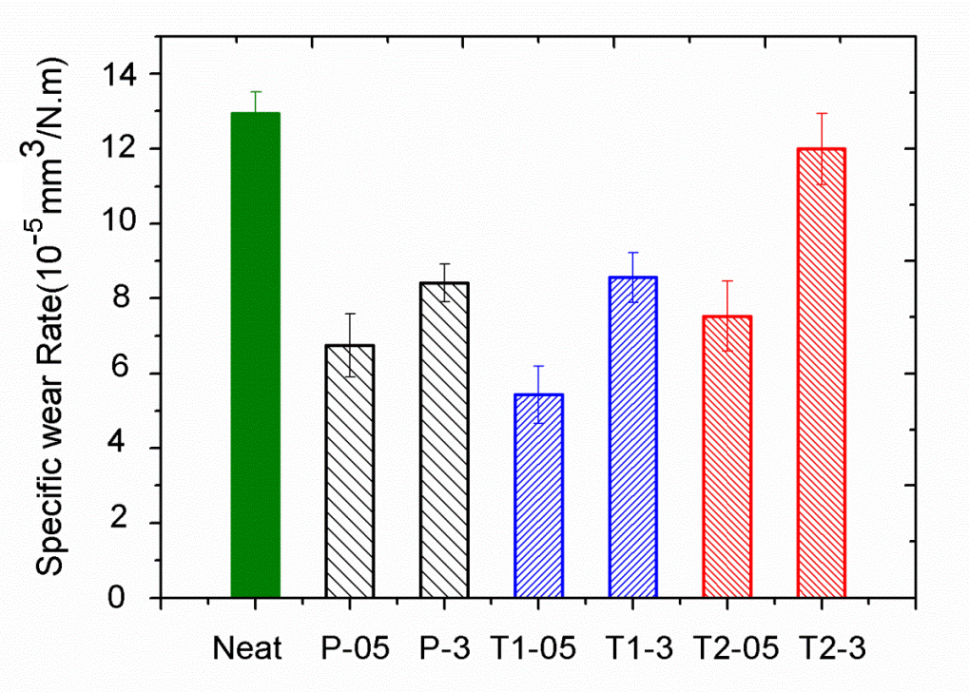

Figure 3.15: Comparison of wear rate for the seven materials by specific wear rate.

Wear rate vs. tensile properties. It was reported that the volumetric wear loss of the material is significantly related to the tensile properties of the material. [51] A number of models have been proposed to relate the volumetric wear loss of polymers (ΔV) to ultimate tensile stress (σ_u), strain at fracture (ϵ_u) and work of fracture as follows:

Ratner-Lancaster's correlation [78]:

$$\Delta V \propto (\sigma_u \epsilon_u)^{-1} \tag{3.3}$$

Wang's model [110]:

$$\Delta V \propto {\sigma_u}^{-3/2} {\epsilon_u}^{-1} \tag{3.4}$$

and Kanagaraj's correlation [51]:

$$\Delta V \propto (work\ of\ fracture)^{-1} \tag{3.5}$$

In Equation (3.5), *work of fracture* is calculated from the area under the stress and strain curve in the tensile test in Section 2.3.1., which refers to the toughness of the polymer and represents the total energy absorbed in the deformation to failure. The wear loss factors (right-

hand side of each equation) in the three correlations were calculated from the experimental results and summarized in Table 3.1. The correlations of the seven materials' specific wear rates and their corresponding wear loss factors are plotted in Figure 3.16.

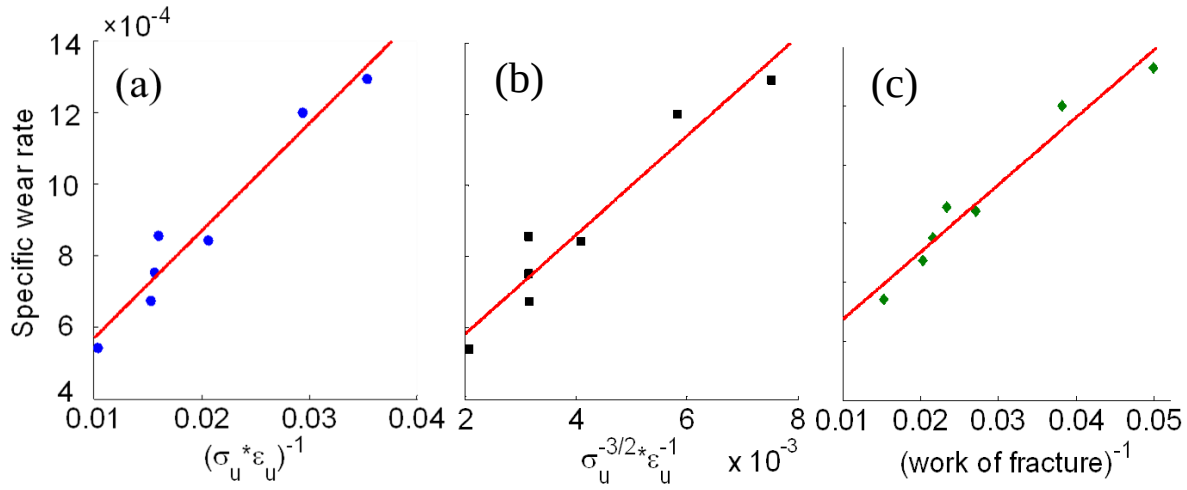

Figure 3.16: Relationship between the specific wear rate and different multiplication factors from: (a) Ratner-Lancaster's correlation; (b) Wang's model; and (c) Kanagaraj's correlation.

Table 3.1: Wear loss factors and specific wear rates of HDPE/CNF nanocomposites.

Sample	Wear loss factors			Specific wear rate
	$(\sigma_u \epsilon_u)^{-1}$	${\sigma_u}^{-3/2}{\epsilon_u}^{-1}$	(work of fracture)$^{-1}$	(10^{-5}mm^3/N.m)
Neat	0.0354	0.0075	0.0499	12.94
P-05	0.0152	0.0032	0.0203	6.75
P-3	0.0206	0.0041	0.0271	8.42
T1-05	0.0103	0.021	0.0152	5.43
T1-3	0.0160	0.0031	0.0233	8.56
T2-05	0.0156	0.0031	0.0215	7.53
T2-3	0.0294	0.0058	0.0381	11.99
Norm of residuals	0.000147	0.000179	0.000143	-

Figure 3.16 shows that the wear rate and the three types of wear loss factors all have the general linear relationships. The norm of residuals between the data points and the fitted line for each type of model are also given in Table 3.1. It can be found that the Ratner-Lancaster and Kanagaraj's correlations have comparable lower norms than Wang's model. Therefore,

compared to Wang's model, the Ratner-Lancaster and Kanagaraj's correlations gave better fits and may predict the wear loss of the nanocomposites more accurately. The wear resistance of HDPE/CNF nanocomposites is general linearly related to the product of ultimate strength and strain at fracture or work of fracture. Although the ultimate strength of the nanocomposite increases with the addition of CNFs (see Table 2.2), the wear resistance of each type of nanocomposite at 3 wt.% loading level is lower than that at 0.5 wt.% due to the reduction of the strain at frature. The highest wear resistance of T1-05 could be the result of the largest work of fracture (see Table 3.1).

Biocompatibility. The *in vitro* cytotoxicity of the neat HDPE and HDPE/CNF nanocomposites was evaluated by the observation of living cells and the number of them in the culture dishes. It was observed that after four days the bottoms of all culture dishes were fully covered by the living cells. The limited space for further growing of the cells might increase the risk of cell degeneration. The cell numbers were counted up to five days without observable cell degeneration, and the microscopic images of the cells were taken after four days. Figure 3.17(a)-(d) show that any signs of cytotoxicity such as cell degeneration, lysis, shrinkage and detachment were completely absent in all groups at the fourth day.

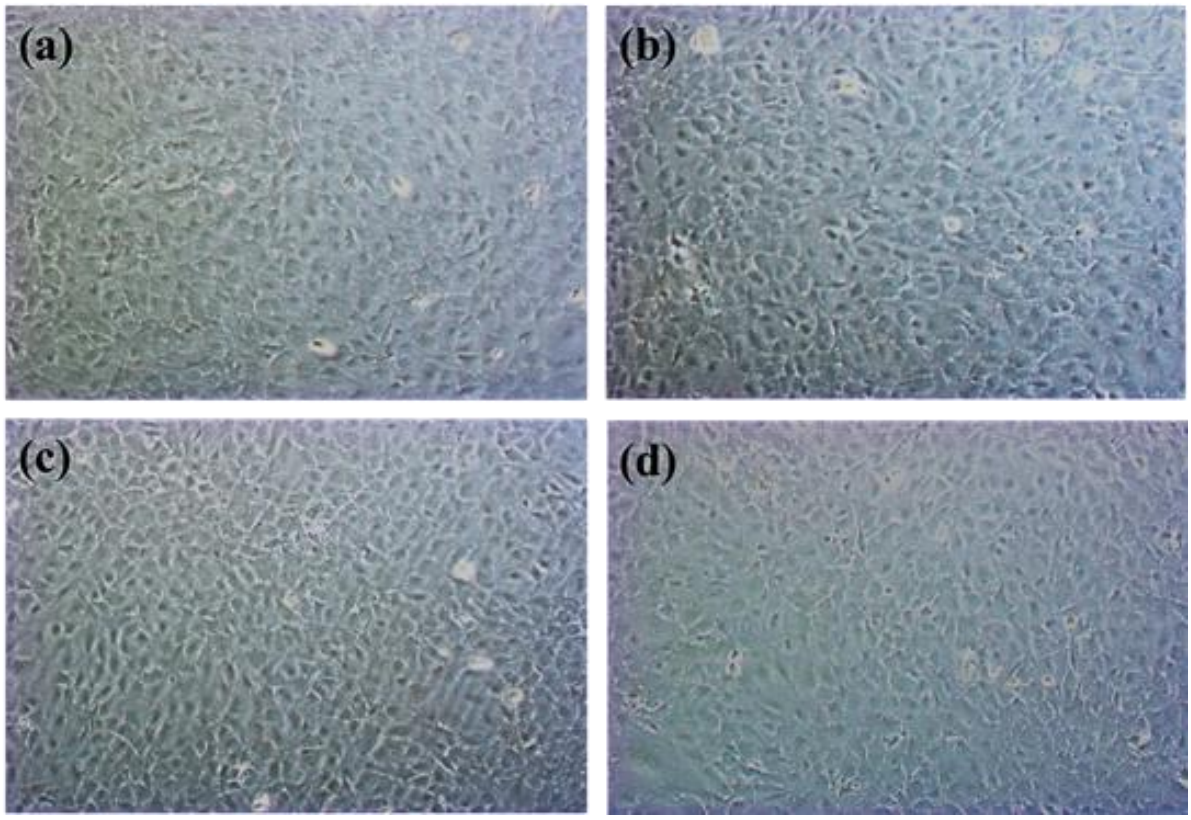

Figure 3.17: Optical microscopy images of MC3T3 cells on the bottom of culture dishes containing (a) Neat, (b) P-3, (c) T1-05, and (d) control after 4 days.

Figure 3.18 shows the cell attachment on T1-05 and P-3 nanocomposites as well as on the neat HDPE sample during the incubation period of four days. The density of the cells on the samples appeared lower than the density of the cells on the bottom of the culture plates as shown in Figure 3.17, because the commercial culture plates used were treated for optimal cell attachment. The MC3T3 cells grew well, and were spreading on both HDPE and HDPE/CNF nanocomposites. The relationship between the number of cells in the culture dishes and the cell culture time are shown in Figure 3.19 (a). It can be seen that the cells in all four groups kept proliferating during the five days. There are no significant differences in the cell numbers between the HDPE/CNF nanocomposites and the control group. The proliferation rates of the MC3T3 cells in the control group and in the culture dish containing T1-05 sample are nearly the same as shown in Figure 3.19 (b). These results revealed that no cytotoxicity was found

due to the addition of CNFs in the HDPE nanocomposites and the nanocomposites did not show any influence on the proliferation of the MC3T3.

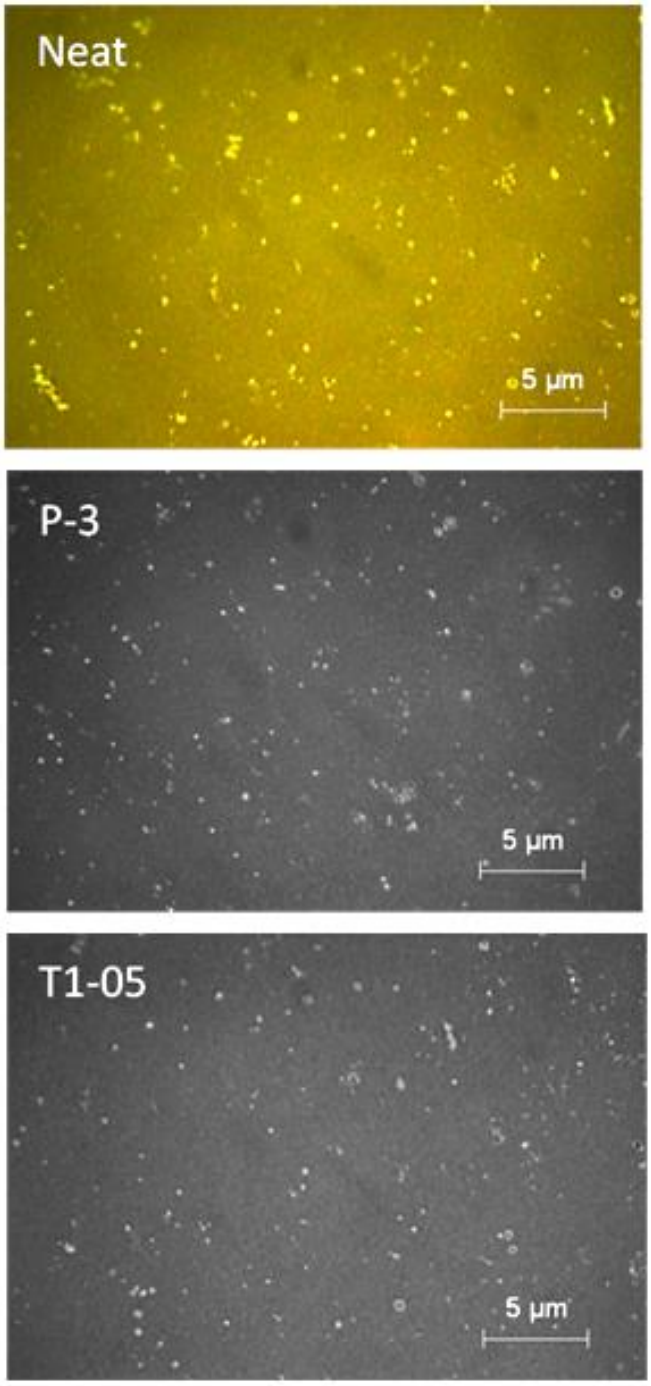

Figure 3.18: Optical images of MC3T3 cells on the neat HDPE and HDPE/CNF nanocomposites after 4 days.

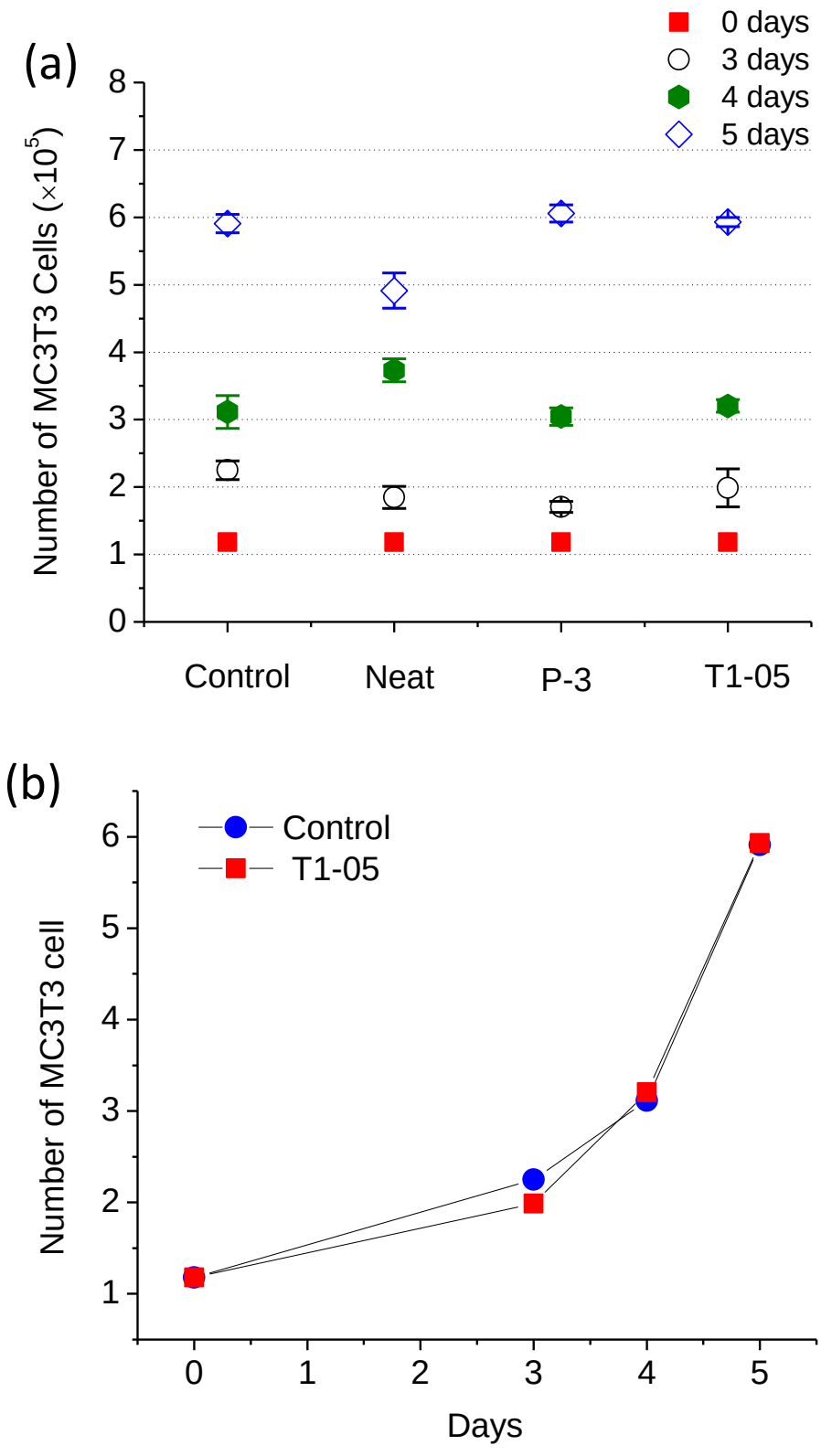

Figure 3.19: (a) Number of MC3T3 cells in the four culture dishes at different culture times and (b) Comparison of the number of MC3TE cells between the control and T1-05 group.

3.4. Conclusion

In this study, the tribological properties of the HDPE/CNFs nanocomposites under the dry sliding, saline water lubricated, and bovine serum lubricated condition were investigated using a pin-on-disc tribometer. In all wear conditions, the addition of CNFs was found to decrease the COF noticeably, even with low concentration of 0.5 wt.%. Compared to the higher loading level of CNFs (3 wt.%), the lower concentration (0.5 wt.%), resulted in lower wear rates possibly due to the good dispersion. The wear resistance of the nanocomposties with thicker-silane treated CNFs were proven to be better than those with pristine and thinner-silane treated CNFs due to improved interaction between the CNFs and the HDPE matrix. The wear rate of the nanocomposite is found to have a weak correlation with micro-hardness, but it is inversely proportional to the work of fracture from the tensile tests. The wear rates of the HDPE nanocomposite with thick-silane treated HDPE at 0.5 wt.% concentration were lower than those of the neat HDPE by about 68%, 35%, and 58% under dry sliding, saline water lubricated, and bovine serum lubricated condition, respectively. Resulting in the best wear resistance of the nanocomposites, CNFs with thick silane coatings at low concentration levels (0.5 wt.%) have the potential to serve as promising reinforcements for HDPE to achieve improved tribological property of the nanocomposites.

CHAPTER 4. WEAR AND FRICTION OF LOW DENSITY POLYETHYLENE AND ULTRA HIGH MOLECULAR POLYETHYLENE UNDER LUBRICATED CONDITIONS

One of the difficulties in tribological studies of UHMWPE is that the wear volume of the UHMWPE under lubricated condition is too low to be quantitatively measured in a short experimental duration. This work uses Reye's model to clarify the relationship between the wear rates (wear volume per sliding distance) of LDPE and the average friction forces under various lubricated conditions, respectively. The experimental results indicates two distinguishable regimes in the relationship due to the different wear modes, namely, the sliding mode and the shaving mode. Similar relationship is also verified to exist for UHMWPE. The relationship is expected to predict the long term wear of the PE family's materials under lubricated conditions in terms of a measured friction force from a short wear test.

4.1. Introduction

UHMWPE is a key material in the production of acetabular cups for hip joint replacements [111]. There is a continuing and urgent need to test new materials, artificial hip designs, and bio-lubricants to reduce the wear and elongate the lifetime of such joint implants [112]. However, one of the difficulties in these tribological studies subject to artificial implants is that the wear of the candidate materials, for example, UHMWPE, is very low, especially when it is under lubricated condition. Therefore, it is very hard to measure the wear quantitatively in a short experimental duration [113]. For example, ASTM standard F732 recommends conducting at least 2 million cycles for each pin-on-disk wear test, which corresponds to about 23 days of testing duration with the commonly used rotation rate of 1 cycle/sec [114]. In addition, at least four wear "measurements" for each sample shall be made. To quantitatively assess the wear of UHMWPE, long term experiments have to be conducted.

Some researchers adopt the visualization method to evaluate wear, which involves inspections of the surface before and after the wear test using microscopy, profilometry, or other techniques to observe the fine surface features [80]. Although widespread and accepted, this method only provides a microscopic snapshot of the surface in its before and after states, and cannot guarantee that the same surface location is selected at different states. Furthermore, the wear evaluation under visualization methods cannot give an exact worn-volume quantity. Other researchers focused upon controlling the coefficient of friction of a system with different hydrodynamic and boundary lubricants, but with little attention or efforts on how these lubricants affect the wear [80]. In many applications, protecting surfaces against wear instead of decreasing the coefficient of friction is the eventual purpose of the biotribology [112]. Therefore, it would be meaningful to predict the wear with some tribological parameters that can be easily obtained in a short experimental duration, such as the average coefficient of friction (or the average friction force).

To model the wear of polymeric materials under lubricated condition, it seems that the famous Archard's law is not applicable, because it is originally derived for the wear of metals under dry sliding condition, as discussed in Section 1.3.5. Another classical wear model, Reye's model [83], may be suitable for the wear of polymers under lubricated condition, as it only considered that the volume of the removed debris due to wear is proportional to the work done by friction forces. Reye's model can be expressed as:

$$\Delta \mathrm{V} = \mathrm{K} \int_0^L F(x)dx \approx \mathrm{K}\, \bar{F} L = KLN\bar{\mu} \tag{4.1}$$

where K is a constant, called specific wear volume in a recent study [84]; L is the sliding distance; F is the friction force, which is a function of the distance; and $\bar{F}$ and $\bar{\mu}$ are the average friction force and the average coefficient of friction within the duration of the wear test, respectively. Equation (4.1) can be rewritten as:

$$\dot{w} = \frac{\Delta V}{L} = K\bar{F} \tag{4.2}$$

where $\dot{w}$ represents the wear rate, or wear volume per unit sliding distance. It should be noted that the unit of K is m^3/J, representing the volume of material removed by one Joule of energy, and K is a material property, independent of the lubricant.

In this chapter, the correlations of the wear rate (wear volume per sliding distance) of LDPE with the corresponding average friction force under five different lubricated conditions are investigated. LDPE is selected due to its higher wear rate compared to HDPE and UHMWPE. The results may have implications to the wear of other members of the polyethylene family since they have similar chemical structures. The various lubricants used in this study include water, bovine serum, water solutions of hyaluronic acid, lipid, and glycerol. Similar relationships between wear rates and average friction forces of UHMWPE under different lubricated conditions are also obtained and compared to those of LDPE. This study is expected to clarify the relationship between the UHMWPE's wear rate and the friction force under lubricated conditions, find the material properties of UHMWPE regardless of the lubricants, normal load, and sliding distance, and provide a method to predict the long term wear of UHMWPE with a friction force that is measured from a short wear test.

4.2. Experiments

4.2.1. Materials

LDPE used in this study was supplied by Small Part Co. with a reported density of 0.92 $g \cdot cm^{-3}$, and medical grade UHMWPE by Total Plastics Inc. with density of 0.945 $g \cdot cm^{-3}$. All polymer pins were tested in the form of cylinders with diameter of 6.35 mm and height of 14mm. The work surface of the pin was polished with by sandpapers with two grit sizes of 400 and 800 to provide final roughness Ra < 1μm. Metal disk was prepared by cutting a medical

implant from Mayo Clinic. The work surface of the metal disk was subsequently polished by sandpapers with two grit sizes of 400 and 1000, and then by Vel-polishing cloth with 0.05 μm Alumina polishing powder to provide roughness Ra = 23-24 nm.

4.2.2. Lubricant preparation

Four types of lubricants, besides water, were prepared for the wear and friction tests. Glycerol solutions were prepared by direct dissolving of glycerol (> 99.5%, Sigma) with water. To obtain a wide range of friction forces, various weight concentrations of Glycerol (10%-99.5%) were used. DPPC (1, 2-dipalmitoyl-sn-glycero-3-phosphocholine, 98%, Avanti Polar Lipids) micellar lipid solution was prepared by serial dilution of sonicated solutions of DPPC in water with lipid concentration of 0.003 mg/ml. Hyaluronic acid (HA) solution was made by dissolving dry Hyaluronic acid (97.3%, NuSci) in water with HA weight concentration of 0.3%, and then the solution was stirred at room temperature for 8-10 hours in order for HA to be completely dissolved. Bovine serum solutions were prepared by diluting concentrated bovine serum (Hyclone Laboratories, Logan, UT) with de-ionized water based on ASTM F1714. In all cases, the lubricant solutions were stabilized with NaN_3 (0.08 ml of 5% NaN_3 solution per 10 ml of lubricant) to prevent microbial degradation.

4.2.3. Pin on disk wear tests

Wear and friction tests were carried out on a pin-on-disc tribometer (UMT-2). A prepolished LDPE or UHMWPE pin was mounted in the pin-holder and pressed with a controlled load against a polished metal disk. Wear tests were performed in the airproof setup shown in Figure 4.1.

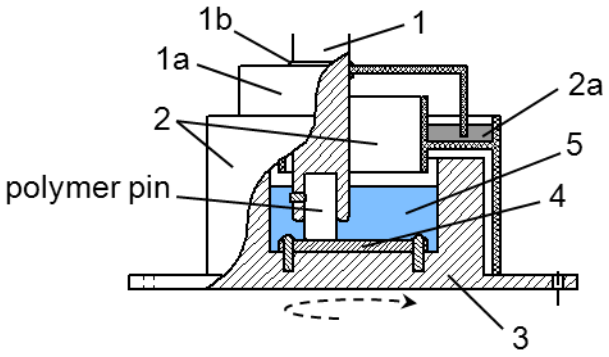

1. Pin holder (stainless steel);
1a. Plastic cap mounted to the holder (polystyrene);
1b. Sealing;
2. Plastic cover (polystyrene);
2a. Silicone "lock";
3. Metal disk holder mounted on the rotating platform (aluminum);
4. Metal disk;
5. Lubricant.

Figure 4.1: Experimental setup for lubricant testing.

The metal disk was mounted on the holder in the center of a rotating platform. The offset between the center of the pin and center of the metal disk was the same (7 mm) for all tests. The lubricant level was kept in the range of 8 to 10 mm. The operating parameters were set as the follows. Sliding speed: 1 rpm, normal load: 5 to 180 N, and test duration: 3 to 76 h. The tangential friction force, F, and normal load, N, were continuously monitored by the tribometer directly, and the coefficient of friction was then calculated as a ratio of F/N. Before each wear test, the polymer pin was washed with acetone and water, dried in oven at 80 °C for at least 8 h., equilibrated at room temperature and weighted 5 to 10 times using a digital balance with the accuracy of ± 0.01 mg. The same procedure was applied to determine the weight of the pin after wear in order to calculate the mass loss of the pin.

4.3. Results and Discussion

4.3.1. Wear and friction of LDPE

Figure 4.2 depicts the wear rate of LDPE against the average friction force in each test for different lubricated conditions. Despite the differences in lubricant type, lubricant concentration and normal load used in the wear tests, two noticeably different regimes can be identified in this figure. In the lower friction force range of 0-20 N (Regime I), the wear rates

of LDPE are low and increase slowly with the increasing of the average friction forces, up to a critical friction force. Upon reaching the critical friction force, a transition from Regime I to Regime II takes place and then the wear rate in Regime II increases more rapidly with the increase of friction force.

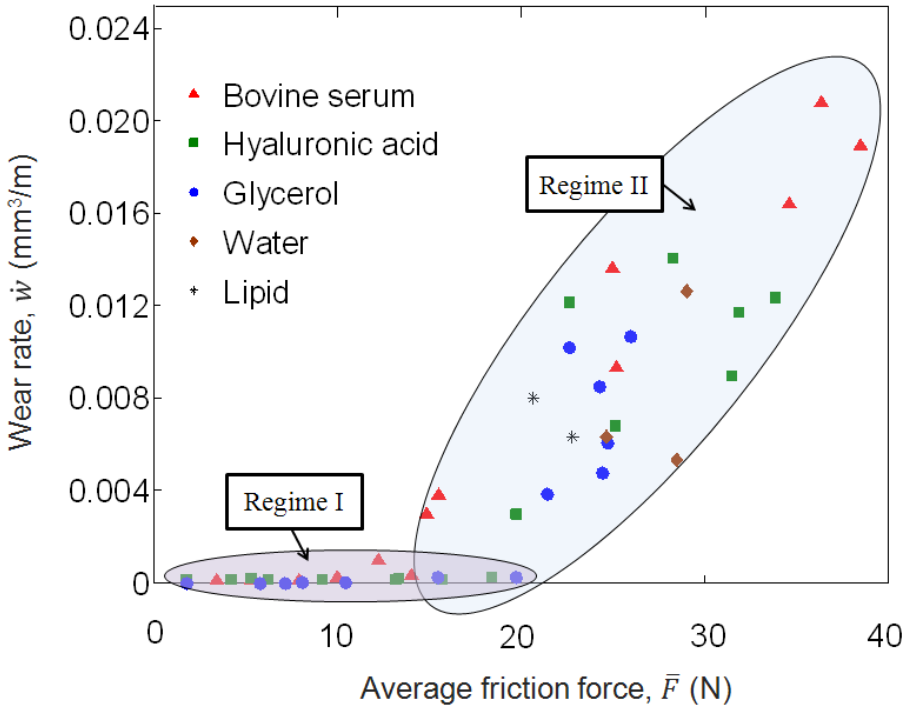

Figure 4.2: Wear rate of LDPE vs. average friction force under lubricated conditions.

It is interesting to note that a similar transitioning behavior occurred in the wear of stainless steel against high-speed tool steel under dry sliding condition as shown in Figure 4.3. Here the wear rate was claimed to be proportional to the applied normal load from Archard's law [75]. The two regimes of wear in Figure 4.2 were named as mild wear and severe wear, respectively. It was believed that the transition from mild to severe wear in stainless steel was strongly related to their wear mechanisms [1]. During mild wear, a protective oxide film formed on the surface of the stainless steel that slowed down the wear generation [1]. However, when the normal load was increased to a critical load, the metal beneath the oxide layer was

plastically deformed, and asperities on the harder material's surface would penetrate through the oxide layer, resulting in a severe wear [64].

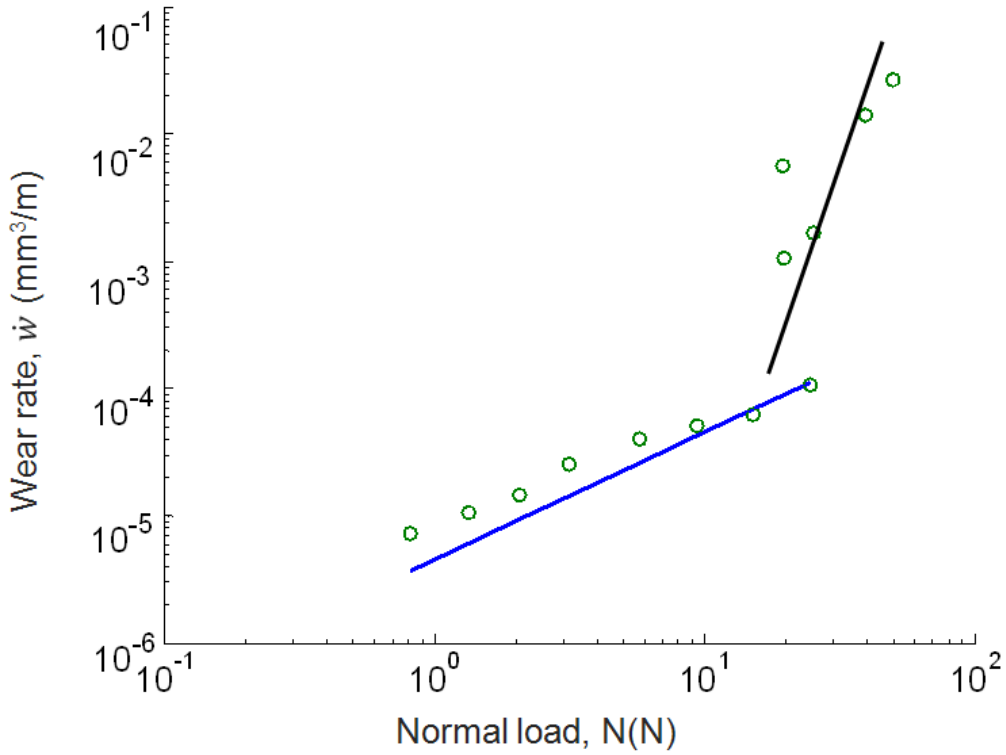

Figure 4.3: Wear rate of stainless steel vs. normal load under unlubricated conditions. (Reproduced with permission from Ref. [75]).

The transition from Regime I to Regime II in Figure 4.2 may also imply a change of the wear mechanism. To identify the wear mechanisms of the LDPE pins in these two wear regimes, the worn surface of the pin after each test and the wear debris were observed using an optical microscope and a digital camera, respectively. Because the wear rate in Regime I is very small, no wear debris was observed in the lubricants with naked eyes. In order for the wear rates to reach Regime I, the normal load was reduced and viscosity of the lubricant was also increased at the same time when conducting the tests. The increase of viscosity (η) and reduction of normal load (p) would increase the Stribeck number as shown in Figure 1.2, and may move the lubrication to the thick film lubrication regime. Under thick film lubrication, the contact surfaces of the pin and disk were entirely separated by a liquid film, which served as a

lubrication layer, resulting in an indirect contact between the pin and metal disk [1, 80]. Because the movable molecules of the liquid lubricants slide upon each other more easily than that of two solid materials, the friction and wear are significantly reduced [80]. The worn surfaces of the pins were relatively smoother in Regime I (Figure 4.4(a)) than in Regime II (Figure 4.4(b)) and did not show any signs of the solid-to-solid asperity contact such as the deep plowing and scratching grooves. It was most likely that in Regime I, the wear of the pins is under the thick film lubrication and the wear mode in Regime I is classified as *sliding mode* in this work.

The worn surfaces of the pins in Regime II are rougher with signs of abrasive wear, such as plowing and scratching grooves (Figure 4.4(b)). These grooves were results of asperity contacts, and the lubrication in Regime II was likely to be the mixed lubrication or boundary lubrication. In addition, the wear debris in Regime II was of sizes observable by naked eyes. The wear debris was mostly in shapes of long stripes. After the wear test, some stripes were still attached to the pin and could easily be observed when being immersed in water as shown in Figure 4.4 (c). The wear mode in Regime II is named as *shaving mode* due to the formation of the long striped debris.

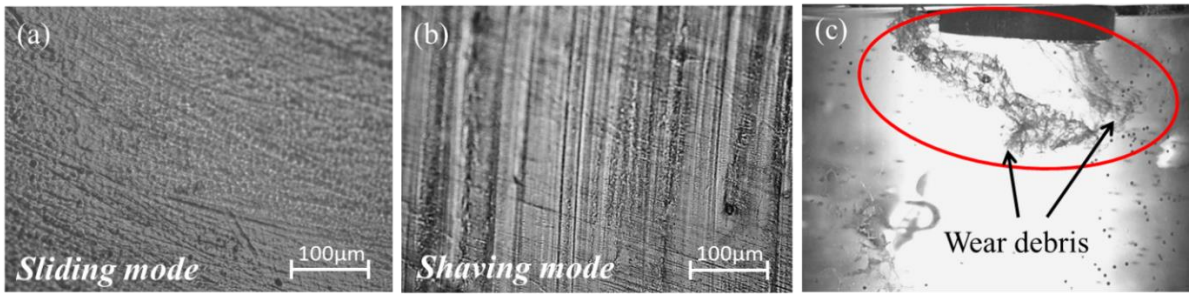

Figure 4.4: Typical worn surfaces of the LDPE pins in wear Regime I (a) and Regime II (b), corresponding to sliding mode and shaving mode, respectively. (c) Wear debris of an LDPE pin in wear Regime II.

Obviously, the two different wear modes resulted in two different relationships between the wear rate and the average friction force in Regime I and Regime II, respectively. However, it seems that both relationships are linear. The slopes (K in Eq. (4.2)) of LDPE in each wear regime can be determined by fitting these experimental data in Figure 4.5 to straight lines. For the data points in Regime I, all the fitted curves are considered to pass through the origin since there should not be any wear when the friction force is zero. Three lines are determined based on the experimental data from the three lubricants, bovine serum (Line BS), hyaluronic acid (Line HA), and glycerol (Line G) (Figure 4.5). The slopes are calculated to be 1.32×10^{-5} (BS), 1.46×10^{-5} (HA), and 1.00×10^{-5} (G), respectively. In addition, the standard errors of estimate (SEE) are determined to be 5.76×10^{-5} (BS), 7.07×10^{-5} (HA), and 6.98×10^{-5} (G), respectively. Only one SEE bar for each fitting curve is shown in Figure 4.5 for clarity of presentation. The scopes of these fitted lines are in the same order of magnitude and the differences among them are very small. It is reasonable to conclude that in Regime I, the different lubricants lead to no significant differences in the generated wear under similar friction forces. All the experimental data in Regime I can therefore be regarded as one group to be represented by one line, as shown in Figure 4.6(a).

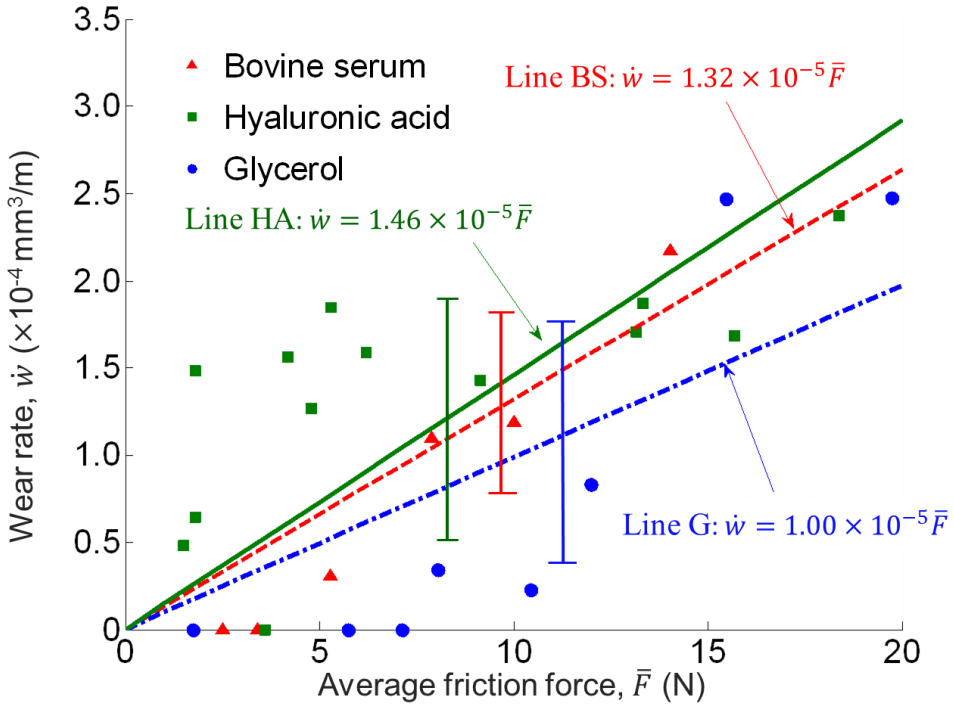

Figure 4.5: Fitting curves for the experimental data points under bovine serum (Line BS), hyaluronic acid (Line HA) and glycerol (Line G) lubricated conditions, respectively; The standard errors of estimate of Line BS, Line HA, and Line G are 5.76×10^{-5}, 7.07×10^{-5}, and 6.98×10^{-5}, respectively.

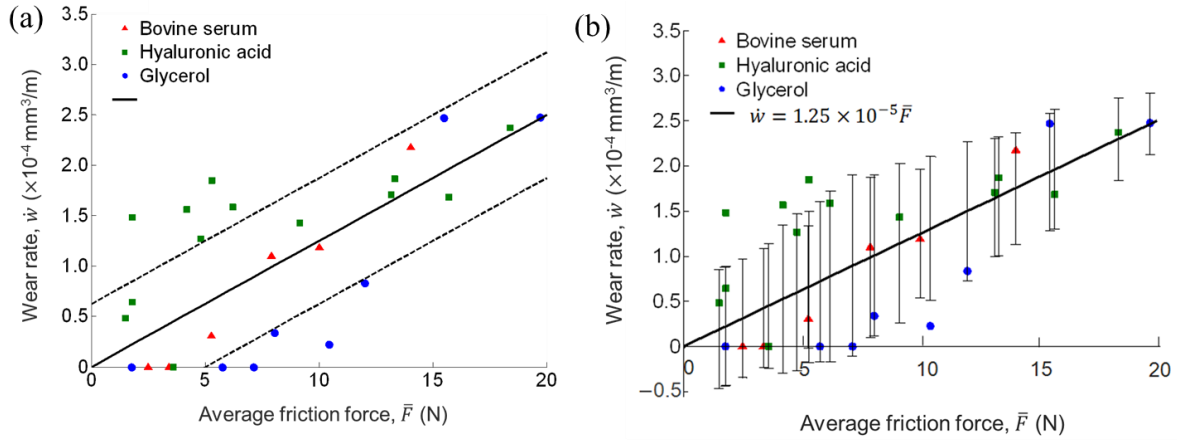

Figure 4.6: (a) Fitted line of all data points in Regime I: SEE = 6.25×10^{-5}; (b) variations of SEE for all data points in Regime I.

The slope of the fitted line (1.25×10^{-5}) in Figure 4.6 (a) is between the BS and HA lines in Figure 4.5 and the SEE are enclosed in between the two parallel dashed lines. The variations of SEE of the fitted line in Figure 4.6 (a) are plotted in Figure 4.6 (b). In Figure 4.6 (b), the SEE at each data point is calculated from the nearest seven data points, instead of the entire data set. It is observed that the SEE generally decreases with the increase of the average friction force. At low friction forces (0-7N), some tests do not yield any detectable wear. Such low or no wear generations led to the scattered nature of the wear rates at low friction forces. One should note that even though the data seems to be scattered in this regime, the differences among them are insignificant. The fitted line in Figure 4.6(a) can therefore be considered to represent the relationship between the wear rate and friction force for LDPE under lubricated conditions, regardless of the lubricant.

Similarly, the wear rates in Regime II can also be represented by a straight line, shown in Figure 4.7. It should be noted that the fitted curve in this regime does not necessarily pass through the origin. Therefore, a linear function of $\dot{w} = K_{II}\bar{F} + b$ is used for the fitted curve in Regime II. The slope of the fitted curve in Regime II (7.19×10^{-4}) is significantly larger than that of the fitted curve in Regime I (1.25×10^{-5}) by an order of magnitude. The value of SEE in Regime II (2.69×10^{-3}) is also several orders of magnitude larger than that of Regime I. After the two fitted curves in both wear regimes are determined, a critical friction force can be identified at which a transition takes place from Regime I to Regime II as depicted in Figure 4.8. The critical friction force of LDPE under lubricated condition is found to be about 13.7 N. Upon reaching this critical value, the wear mode changes from sliding mode to shaving mode, and then the wear rate increases rapidly as the friction force increases.

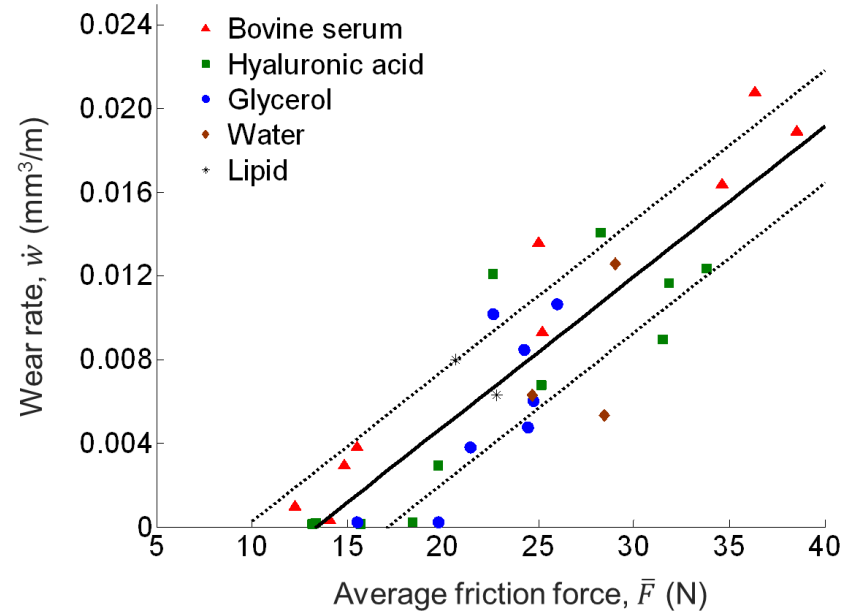

Figure 4.7: Fitted curve of all data points in Regime II, where K_{II} and b are 7.19×10^{-4} and 0.96×10^{-4}, respectively; the standard error of estimate of the fitted curve is 2.69×10^{-4}.

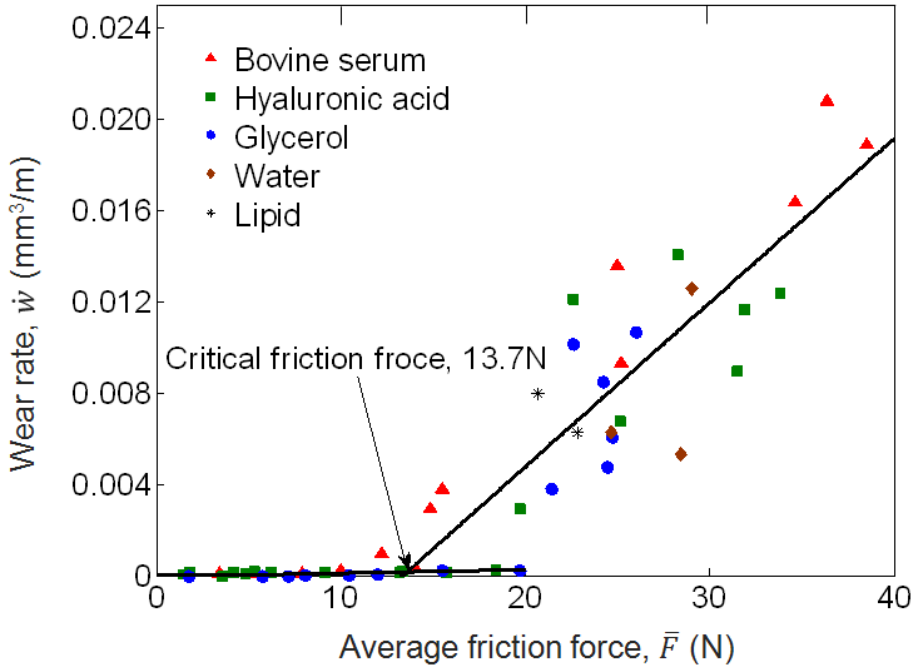

Figure 4.8: Determination of the critical friction force of LDPE.

4.3.2. Wear and friction of UHMWPE

To exam whether a similar correlation of the wear rate and average friction force exists for UHMWPE, wear tests are performed under various lubricated conditions, and the results are shown in Figure 4.9. Water, hyaluronic acid, lipid, bovine serum, and combinations of lubricants are used in the wear tests. Due to the superior wear resistance of UHMWPE, it takes much longer duration to generate any detectable wear of the material. Similarly, two different regimes, labeled in Regime I and Regime II, can be classified, corresponding to sliding wear mode and shaving wear mode, respectively. The slopes of the fitted curves in Regime I (K_I) and Regime II (K_{II}) are found to be 6.05×10^{-7} and 2.29×10^{-4}, respectively. The SEE of each fitted curve are enclosed in between two parallel dashed lines. The critical friction force that marks the transition from Regime I to Regime II is found to be 21 N.

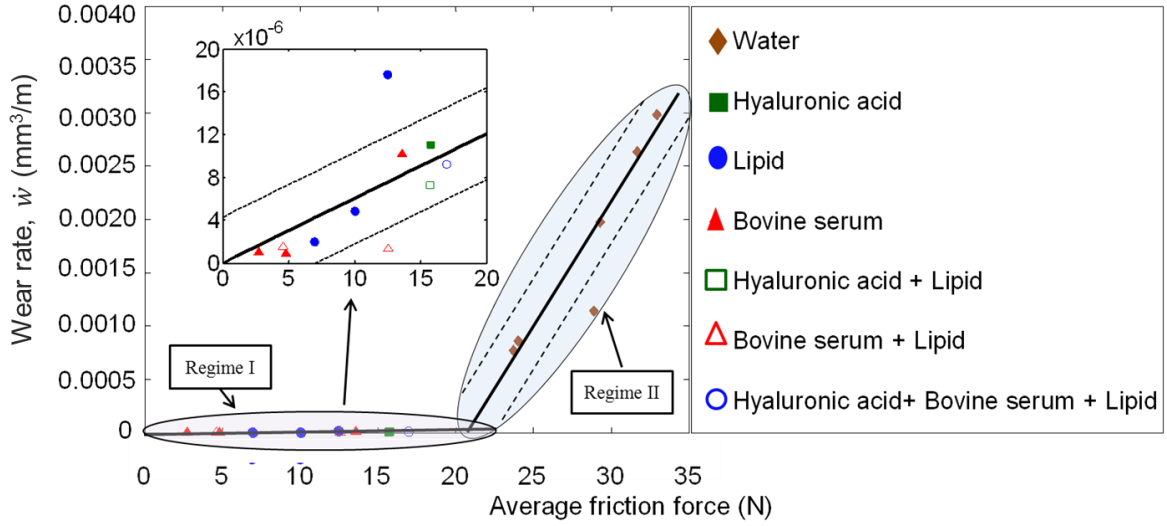

Figure 4.9: Wear rate of UHMWPE vs. the average friction force under lubricated conditions; the fitted curve in Regime I has the slope of 6.05×10^{-7} and SEE of 4.29×10^{-6}; the fitted curve in Regime II has the slope of 2.29×10^{-4} and SEE of 3.83×10^{-4}.

To compare the wear rate vs. average friction force relationships between LDPE and UHMWPE, the fitted curves of the two materials in both regimes are plotted in Figure 4.10.

The curves of LDPE have higher slopes in both regimes, indicating higher specific wear volumes (K) and lower wear resistance. Since the physical explanation of specific wear volume, K(m^3/J), is the volumetric material loss per unit of friction energy, under the same wear mode, LDPE produces more wear than UHMWPE with the same amount of energy consumption. Furthermore, the critical friction force of LDPE is also lower than that of UHMWPE, suggesting that in the wear of LDPE, more severe wear will start to take place at lower friction force compared to UHMWPE.

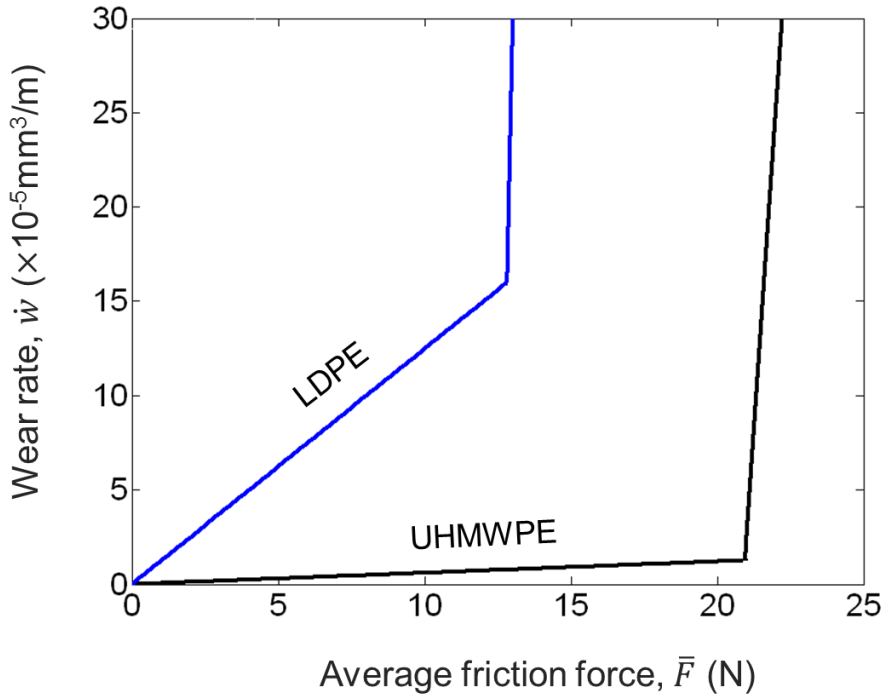

Figure 4.10: Comparison of the wear rate vs. average friction force between LDPE and UHMWPE.

It should be noted that the specific wear volume and critical friction force are both material properties and independent of the lubricants, normal load, and sliding distance. For example, Figure 4.11 shows that although the wear tests of UHMWPE or LDPE have various lubricants, normal load, and sliding distance, similar wear rates are approached in term of the similar undergoing friction force. For a new material, the wear rate vs. friction force

relationship can be obtained through a sufficient number of wear tests. Once it is known, the mass loss of the material under a certain condition (certain lubrication, normal load, and sliding distance) can be easily predicted with a friction force. This friction force may simply be measured from a very short wear test under the certain lubrication and normal load.

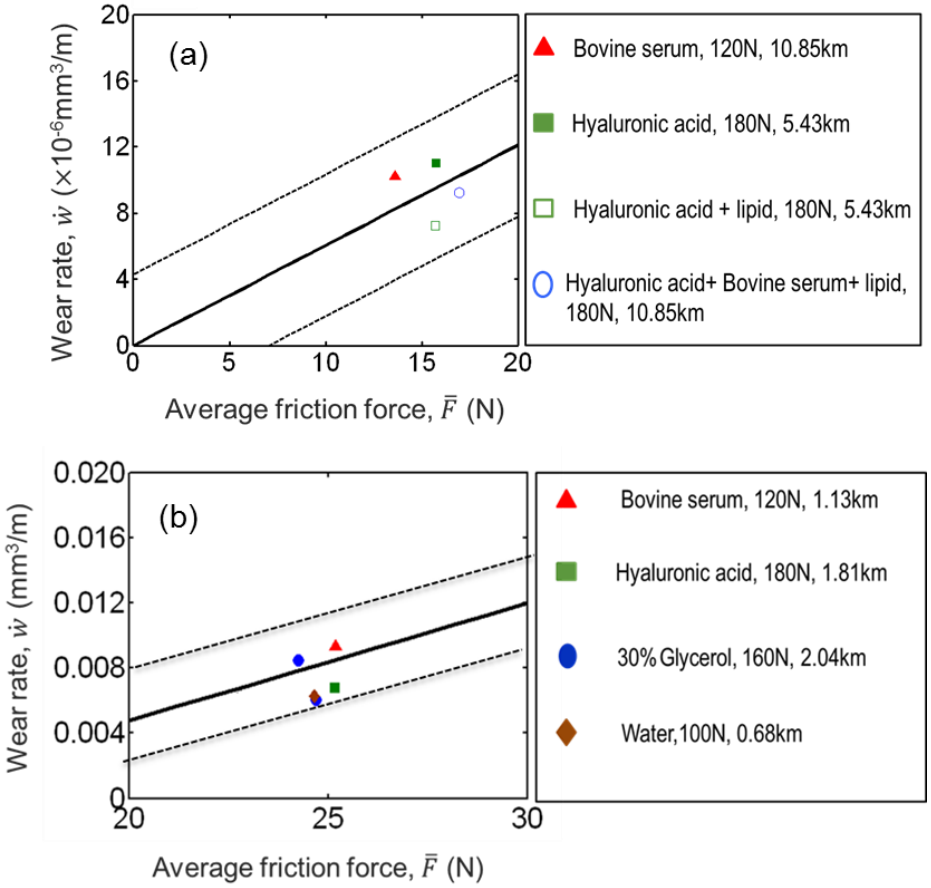

Figure 4.11: The wear rates of UHMWPE in Regime I (a) and LDPE in Regime II (b) under various experimental conditions (different lubricant, normal load, and sliding distance).

It is worthwhile mentioning that compared to the average clinical wear rate the wear rate of UHMWPE in the hip simulator under bovine serum lubricated conditions was consistently underestimated due to the protein precipitation of bovine serum protecting the UHMWPE cup from direct contact with the metal ball [112, 115]. Therefore, such precipitates should be minimized during the wear test [24]. Liao et al. [115] demonstrated that the amount

of protein precipitation increased with the time duration of the wear test. If this wear rate vs. average friction force relationship is applied to predict the wear rate of UHMWPE in the bovine serum lubricated wear test, a friction force of UHMWPE can be measured in a very short wear test. The influence of protein precipitation would be significantly minimized. Therefore, the wear rate predicted from such friction force may be much closer to the clinical relevance.

4.4. Conclusion

This chapter discusses the correlation of the wear rate of LDPE under lubricated conditions with the friction force. The experimental results indicate two distinguishable regimes due to the different wear modes, namely, the sliding mode and the shaving mode. A transition between these two regimes occurs at a critical friction force, which is found to be 13.7 N for LDPE. When the friction force is below this critical value, the wear rate varies little with the friction force under the sliding wear mode, regardless of the lubricant. Beyond the critical friction force value, the wear rate increases rapidly under the shaving mode and large strip-shaped wear debris is produced. Similar wear and friction behaviors are found in the case of lubricated wear of UHMWPE, and the critical friction force is determined to be 21 N. Since the specific wear volume (i.e. volumetric material loss per unit of friction energy) and critical friction force are both material properties and independent of the lubricant, it is hypothesized that similar wear modes, sliding and shaving, and transition from the former to the latter may also exist for other polymeric materials under lubricated conditions.

A wear rate vs. average friction force relationship of a material is very helpful to predict the wear rate of the materials. Once a friction force of the material under a certain lubrication and normal load is measured in a short wear test, the wear rate of the material (wear volume per unit sliding distance) can be calculated in terms of the friction force. Therefore, the time-consumption of the wear test will be significantly reduced. This method may also be desirable

to determine the wear rate of UHMWPE under bovine serum lubricated condition, because a friction force from a short wear test minimizing the influence of protein precipitation of bovine serum may result in a much closer value of wear rate to the clinical relevance.

CHAPTER 5. AN ENERGY-BASED MODEL FOR THE WEAR OF HDPE/CNF NANOCOMPOSITES IN DRY SLIDING CONTACT WITH A STEEL BALL

When two loaded bodies are in relative sliding contact, friction occurs at the interface. Most of the frictional work is transformed into heat, which is responsible for the increasing in the temperature of the sliding bodies. This chapter reports a thermal analysis that is derived to use an experimentally determined temperature increasing and the thermal conductivity of the nanocomposites to achieve the friction energy consumption on heat. Assuming the remaining friction energy is responsible for wear particles generation, the correlation of the wear and the thermal conductivity are studied and a new wear resistance is defined to predict the wear loss.

5.1. Introduction

Wear is defined as a progressive loss of surface material due to relative sliding of two loaded contacting surfaces [10]. When two complying materials slide against each other, a tangential friction force will be experienced at the interface. Ramalho [9] concluded that the friction energy in the sliding contact can be dissipated mainly through three processes: heat, wear particle generation, and other entropy changes associated with material transformation at the interface, in which the major portion of friction energy will be transformed into thermal energy for a metal-to-metal friction pair [116]. If the wear mechanism of a material remains stable, one may stipulate that the relative ratio of the different parts of the energy consumption could be constant. There were many attempts to establish relationships between wear and friction energy dissipation during sliding. Colaco [117] showed that a linear correlation between the wear rate of the UHMWPE and the dissipated energy existed. The correlation was independent of the lubricant, the material of the counterbody, and the surface roughness of both materials. Michael [118] treated friction and wear as a production of irreversible entropy by

interfacial dissipative processes and links friction and wear at dry sliding interfaces based on fundamental principles of thermodynamics.

As mentioned in Chapter 1, HDPE has been widely applied as a bearing material and the addition of CNFs are found to effectively enhance the thermal conductivity of the nanocomposites compared to the neat HDPE in Chapter 2. However, currently the contribution of thermal conductivity to wear has not been clearly understood. The aim of the present work is to explore the possible relationship between the wear behavior and the improved thermal conductivity of HDPE/CNF nanocomposites and establish an energy-based wear model to correlate the wear loss of the nanocomposites with the dissipated friction energy and thermal response of the wearing surface.

5.2. Experiments

The wear and friction testing was performed on a pin-on-disc tribometer (UMT-2). The schematic of pin-on-disc tribometer is illustrated in Figure 5.1. The pins used were stainless steel balls (SS440 Grade 25) from Salem Specialty Ball, Inc. with a diameter of 4.762 mm. The tribological parameters were set as 30 N, 8 hours and 60 rpm for the normal load, test duration, and rotating speed, respectively. Only five materials (Neat, P-05, P-3, T1-05, and T1-3) were selected in this chapter. The thermal conductivities of the five materials are given in Section 2.3.3. The polymeric samples with sizes of 25.4 × 25.4 × 4.9 mm were cut from the compression-molded plates. The radius of the wear track (R) was 5 mm. The tangential friction force (F_x) was continuously monitored by the pin-on-disc tribometer directly. The mass loss of each specimen was measured using a digital scale with an accuracy of 0.1 mg.

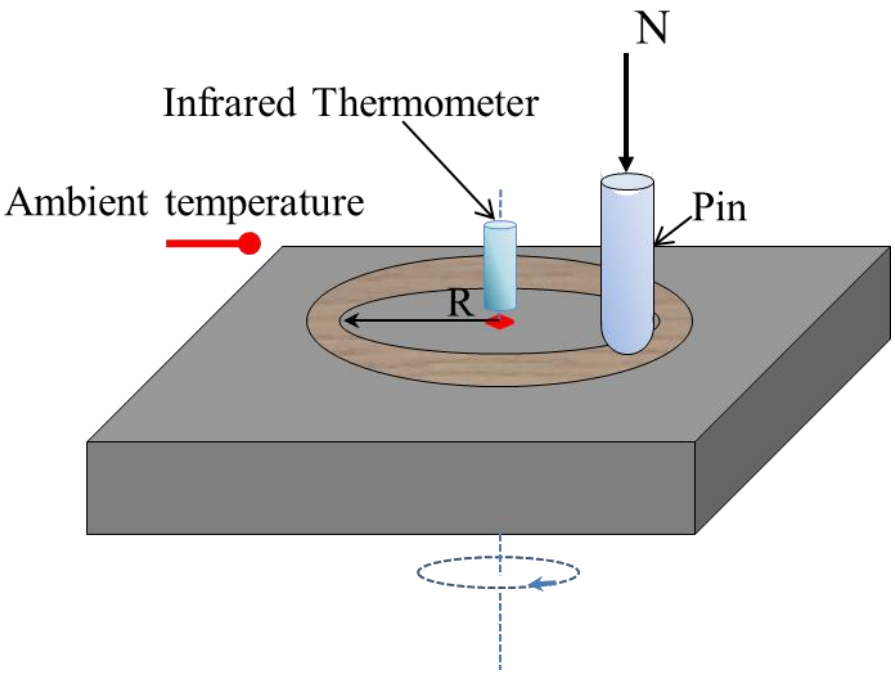

Figure 5.1: Schematic of the pin-on-disc wear testing and temperature measurement apparatus.

During the dry sliding wear test, the temperature on wear track was recorded using a non-contact infrared thermometer with the measured surface area 2.5 × 2.5 mm. With same infrared thermometer the temperature at the center of the wear track for each materials was also measured repeatedly as shown in Figure 5.1. Another digital thermometer measured the ambient temperature during the testing in order to determine the temperature change on the wear track.

5.3. Results and discussion

5.3.1. Friction and friction energy

Friction is the force resisting the relative motion between two contacting surfaces. The COF, which describes the ratio of the friction force between two rubbing bodies and the normal force pressing them together, is generally used to characterize the friction properties of materials in sliding contact with a counterbody. Figure 5.2 depicts the COF of the five materials

(Neat, P-05, P-3, T1-05, and T1-3) as a function of time. The wear damage of materials in sliding was believed to be resulted from friction energy (ΔE) due to friction between the contacting materials [119]. The definition and application of friction energy during sliding systems were reported in [9, 120-122] for different testing conditions and were introduced in Section 1.1.1. in this dissertation. For simplification, the calculation of ΔE can be approximately determined as:

$$\Delta E = \int_0^L F(x)dx = \bar{F}L = \bar{\mu}Nvt \tag{5.1}$$

where F and L are friction force and sliding distance, respectively; $\bar{F}$ and $\bar{\mu}$ are average friction force and average COF during the duration of wear test, respectively; v is the sliding speed; N is the normal load; and t is time. The amount of friction energy during the total dry sliding between the five materials and the steel ball is summarized in Table 5.1.

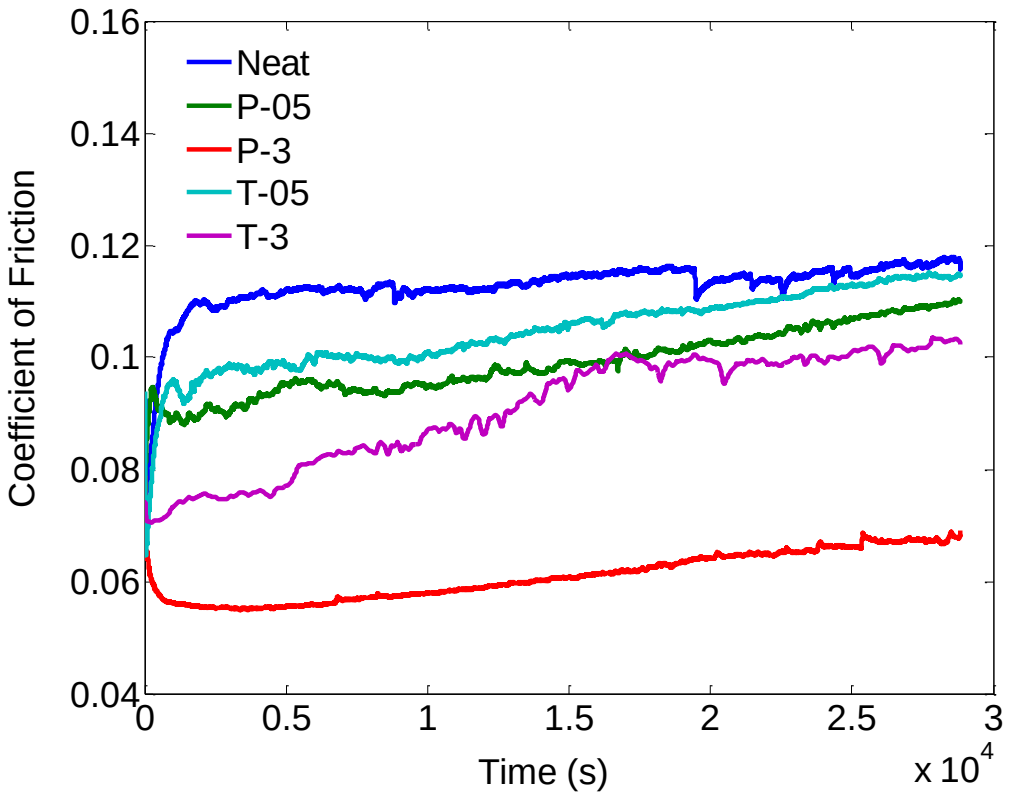

Figure 5.2: Variations of COFs of HDPE and HDPE/CNF nanocomposites with time.

Table 5.1: Friction energy and its apportion for HDPE and HDPE/CNF nanocomposites during dry sliding wear test.

Samples	ΔE (J)	ΔT (℃)	n	m	W_h (J)	W_w (J)
Neat	3464.4	3.25	7.2	62.3%	2158.4	1306.1
P-05	2987.0	2.12	7.0	47.2%	1410.7	1576.3
P-3	1847.5	1.56	6.7	57.9%	1069.4	778.1
T1-05	3225.7	3.73	6.9	82.0%	2645.9	579.8
T1-3	2797.1	2.86	6.8	75.9%	2123.9	673.1

5.3.2. Thermal analysis

Part of the friction energy is converted into heat (W_h), which dissipates into both the upper (stainless steel pin) and lower (polymeric sample) solids, illustrated in Figure 5.3. The total heat energy can be expressed as:

$$W_h = W_U + W_L \tag{5.2}$$

where W_U and W_L are the heat that dissipates into the upper and lower solids, respectively.

or

$$W_h = A_c K_U \left|\frac{\partial T_s}{\partial z}\right|_U + A_c K_L \left|\frac{\partial T_s}{\partial z}\right|_L \tag{5.3}$$

where A_c is the contact area, K_U and $K_L$are the thermal conductivity of the upper and lower solids, z is the distance, and T_s is the temperature at the interface.

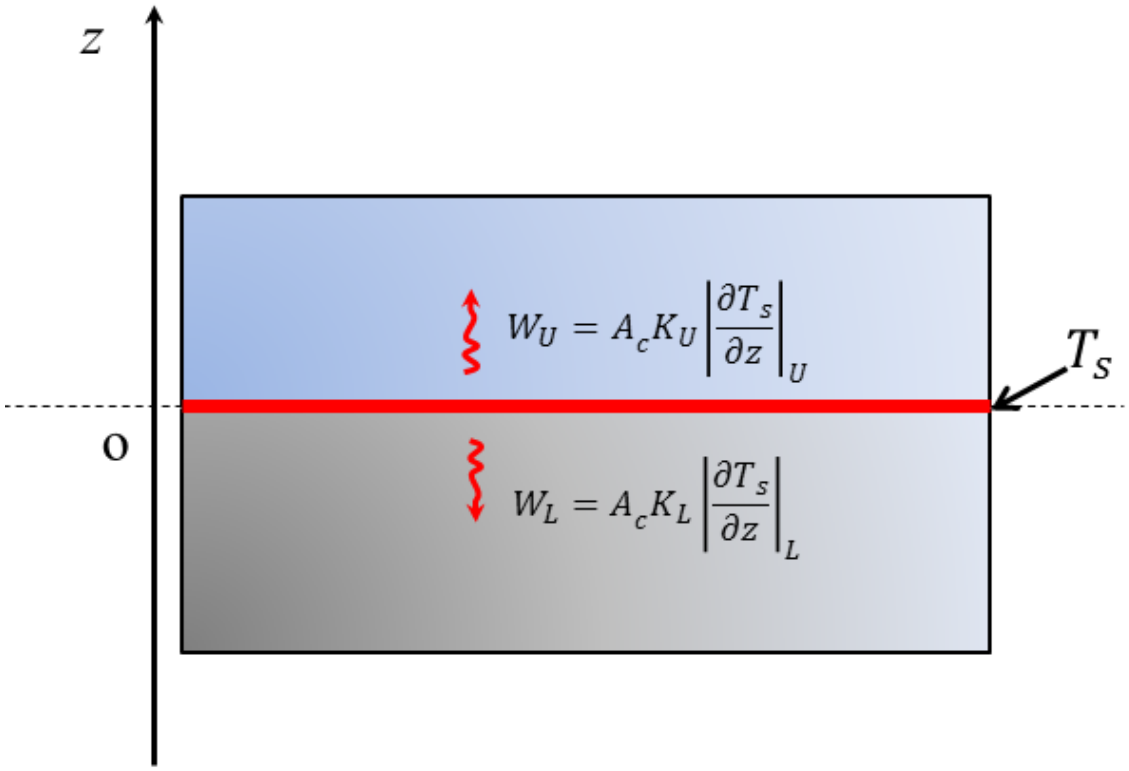

Figure 5.3: Schematic of heat transfer from the contact area.

The heat conducted into the upper solids is calculated by:

$$W_U = A_c K_U \left|\frac{\partial T_s}{\partial z}\right|_U \cong \frac{K_U A_C}{\sqrt{3\alpha_U t}}(T_s - T_0)$$

$$= \sqrt{\frac{\rho_U C_U K_U}{3t}}(T_s - T_0) \tag{5.4}$$

with

$$\alpha_U = \frac{K_U}{\rho_U C_U} \tag{5.5}$$

where α_U, ρ_U, and C_U are the thermal diffusivity, density, and specific heat capacity of the upper solid, respectively; t is the contact time; and T_0 is the ambient temperature [123]. In addition, the heat conducted into the lower solids can be expressed by similar equations. Therefore, the ratio of heat energy conducted into the upper and lower solids (n) may be given by:

$$n = \frac{W_U}{W_L} = \sqrt{\frac{\rho_U C_U K_U}{\rho_L C_L K_L}} \tag{5.6}$$

where C_L, ρ_L, and K_L are the specific heat capacity, density, and thermal conductivity of the lower solid, respectively. To calculate the ratio *n*, the density and specific heat capacity of the nanocomposites is calculated based on the weight fraction of CNFs. The density of CNFs and HDPE is respectively taken as 1.95 g/cm^3 and 0.954 g/cm^3 and the specific heat capacity of CNFs and HDPE as 2.48 J/g·K and 1.075 J/g·K [124, 125], respectively. The thermal conductivity and specific heat capacity of the stainless steel pin were taken as 16 W/m·K and 0.45 J/g·K, respectively. The ratio *n* for each material is calculated and listed in Table 5.1.

During the wear test, the sample was rotated at a speed of 60 rpm. Therefore, it is assumed that the heat generated from the transient frictional interaction have a relatively uniform distribution on the wear track during the sliding. Wear tracks with radius of 5 mm, can be treated as a stationary circular heat source.

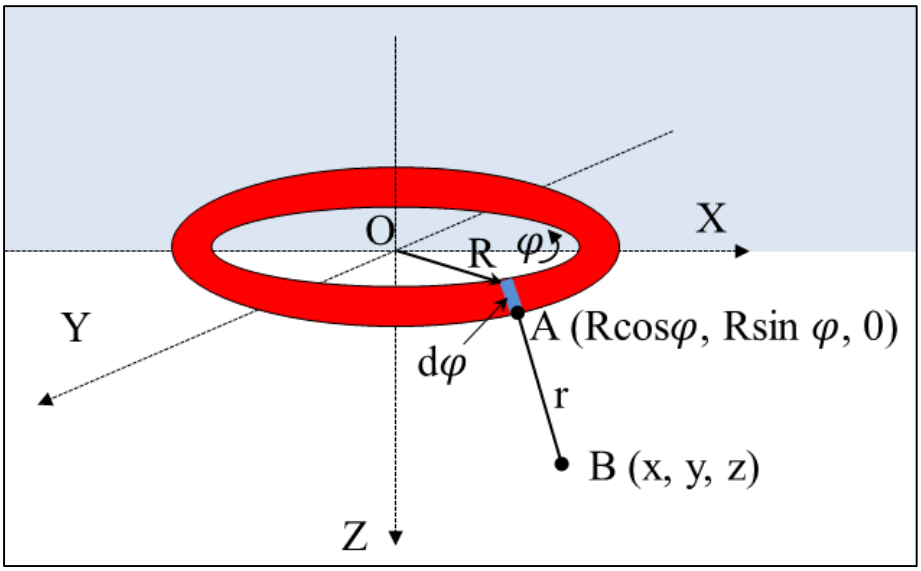

Figure 5.4: The idealized geometrical relation between a circular heat source and a location B (x,y,z) in a half space.

Figure 5.4 illustrates a half-space subjected to a circular heat source which simulates the wear track. The heat rate per unit of length, $\dot{Q}_L$ corresponding to a small piece of the heat source $d\varphi$ can be expressed as:

$$\dot{Q}_L = \frac{\dot{Q}_s}{2\pi R} \tag{5.7}$$

where $\dot{Q}_s$ is the heat rate of the circular heat source from friction energy and R is the radius of the circular heat source. The temperature rise at location B (x, y, z) caused by the heat flux over dφ at A ($R\cos\varphi$, $R\sin\varphi$, 0) can be determined from:

$$-4\pi r^2 K_L \frac{dT}{dr} = \dot{Q}_L R d\varphi \tag{5.8}$$

where K_L is the thermal conductivity of the material, r is the distance between point B and the outer circumference,

$$r = \sqrt{(x - R\cos\varphi)^2 + (y - R\sin\varphi)^2 + z^2} \tag{5.9}$$

The temperature at B due to the heat flux over dφ is therefore

$$T(r) = -\frac{\dot{Q}_L \cdot R \cdot d\varphi}{4K_L\pi} \cdot \frac{1}{r} + \tilde{c} \tag{5.10}$$

where $\tilde{c}$ is a constant. Therefore, the temperature at location B due to the entire circular heat source can be calculated from

$$T_B(x, y, z) = \int_0^{2\pi} T(r) d\varphi + \tilde{C} \tag{5.11}$$

Then from Equation (5.9) and (5.10), Equation (5.11) can be rewritten in the form of:

$$T_B(x, y, z) = \frac{\dot{Q}_L \cdot R}{4K_L\pi} \int_0^{2\pi} \frac{1}{\sqrt{(x - R\cos\varphi)^2 + (y - R\sin\varphi)^2 + z^2}} d\varphi + \tilde{C} \tag{5.12}$$

Combined with Equation (5.7), Equation (5.12) can be reformed into:

$$T_B(x, y, z) = \frac{\dot{Q}_s}{8K_L\pi^2} \int_0^{2\pi} \frac{1}{\sqrt{(x - R\cos\varphi)^2 + (y - R\sin\varphi)^2 + z^2}} d\varphi + \tilde{C} \tag{5.13}$$

When the distance between B and wear track is an infinity, the integral part in Equation (5.13), noted as D(x,y,z), is zero and T_B is equal to T_0. Therefore, $\tilde{C}$ is actually T_0 and Equation (5.13) is changed to:

$$T_B(x,y,z) = \frac{\dot{Q}_s}{8K_L\pi^2} D(x,y,z) + T_0 \tag{5.14}$$

Then,

$$\dot{Q}_s = \frac{8K_L\pi^2}{D(x,y,z)}(T_B(x,y,z) - T_0) = \frac{8K_L\pi^2}{D(x,y,z)}\Delta T(x,y,z) \tag{5.15}$$

where ΔT, thus, is the temperature increasing at a point *B (x, y, z).* However, in reality a temperature at a point cannot be detected. Almost all the thermometers actually measure the average temperature in a snapshot area of the surface. The measurement area of the infrared thermometer used in this work is a 2.5 × 2.5 mm. Therefore, *D(x, y, z)* used in Equation (5.15) have to be the average value of *D(x, y, z)* for the thermometer measured surface area, noted $\overline{D}(x,\ y,\ z)$. In this work, we measured the temperature increase at the center of the wear track and $\overline{D}(0,\ 0,\ 0)$ thus was calculated to be 1.02 (mm^{-1}). The calculation method can be found in Appendix A in the end of the dissertation.

We also assume that the heat is only conducted into the lower space of the (X, Y, Z) coordinate system without any conduction into the upper space of air. The heat generation conducted to the lower solid is calculated by:

$$W_L = \dot{Q} \cdot t_m \tag{5.16}$$

where $\dot{Q}$ is the modified heat flux of wear track, and $t_m$is the sliding duration.

$$\dot{Q} = 2\dot{Q}_s, \tag{5.17}$$

because the upper space in coordinate system (X, Y, Z) is air which have a very lower thermal conductivity compared to the solid sample and can be considered to an insulation without dissipation of heat. The values of the heat energy for all the five materials are listed in Table 5.1.

A heat weight factor, defined as the ratio between heat energy (W_h) and total dissipated friction energy (ΔE), thus, can be determined by:

$$m = \frac{W_h}{\Delta E} = \frac{W_L + W_U}{\Delta E} = \frac{W_L(1+n)}{\Delta E} = \frac{2\dot{Q}_s t}{\bar{\mu} N v t}(1+n)$$

$$= \frac{16\pi^2 K_L}{\bar{\mu} N v} \frac{\Delta T}{D} \left(1 + \sqrt{\frac{\rho_U \cdot C_U \cdot K_U}{\rho_L \cdot C_L \cdot K_L}}\right). \quad (5.18)$$

Equation 5.18 thus provides us with a way to analyze the apportion of dissipated friction energy as long as we access these parameters in the equation. It can be found that the increased thermal conductivity of lower solid materials positively contributed to the energy dissipated as heat.

5.3.4. Energy-based wear modelling

We assume that the total friction energy is dissipated mainly through the heat energy (W_h) and wear generation (W_w). The energy balance can be written as:

$$W_w = \Delta E - W_h \quad (5.19)$$

where ΔE and W_h are now accessible from Section 3.1. Specific wear volume (SWV) was proposed to relate the wear volume and the dissipated friction energy in a recent study [84]. SWV, as a new parameter for the characterization of wear resistance, was defined as the volumetric material loss per unit of dissipated friction energy [122] :

$$\dot{w}_{SWV} = \frac{\Delta V}{\Delta E} \quad (5.20)$$

where $\dot{w}_{SWV}$ is specific wear volume and ΔE is the dissipated friction energy during the sliding distance. However, the dissipated friction is not only dissipated into wear generation, but also into heat generation or temperature rising. Therefore, a modified specific wear volume can be determined as:

$$\dot{w}_m = \frac{\Delta V}{W_w} \quad (5.21)$$

Here the modified specific wear volume is defined as the volumetric material loss per unit of energy (mm^3/J).

The modified specific wear volumes of HDPE and various HDPE/CNF nanocomposites are reported in Figure 5.5. To validate the modified wear rate, the traditional specific wear rate (wear volume per unit of normal load per sliding distance) is used to compared with the modified wear rate for the five materials (Figure 5.6). It showed that they have a similar trends

and are consistent with each other. Only P-3 nanocomposite has a lower specific wear rate than that of the neat HDPE in Figure 5.6, but shows a higher modified specific wear volume than that of the neat HDPE. This is because that the modified specific wear volume considers two more new parameters (thermal conductivity and COF) compared to the specific wear rate. It should be noticed that the modified specific wear volume is a material property which is expected to be regardless the sliding speed, normal load, and the counterface material. However, it needs more experiments to verify the claims in future.

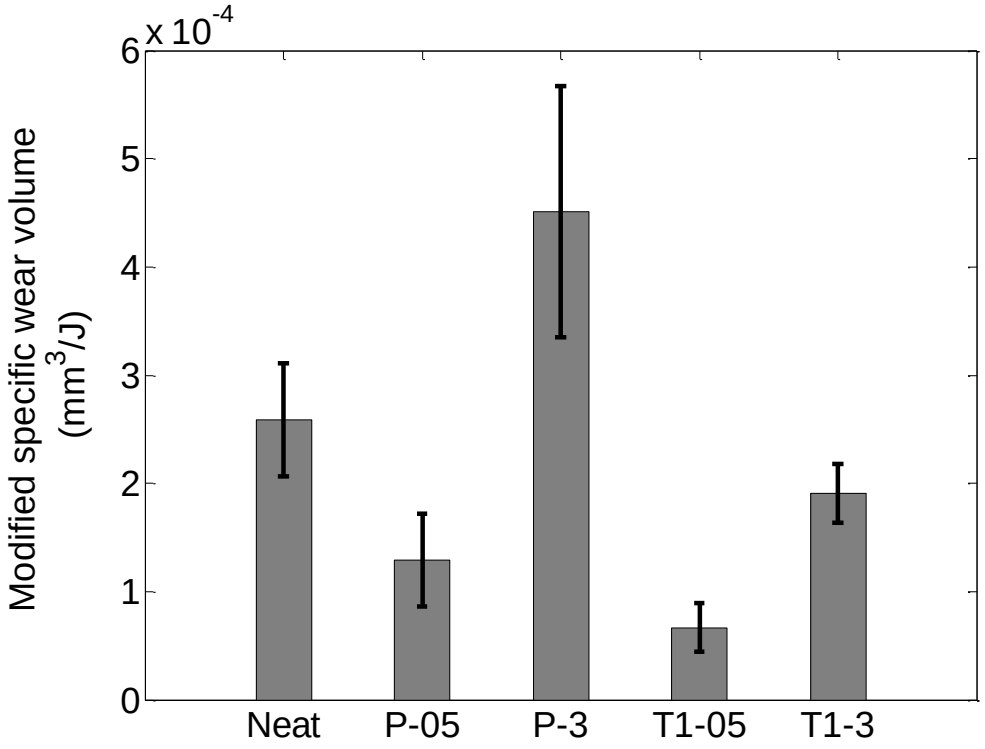

Figure 5.5: Comparison of the modified specific wear volume of the five materials.

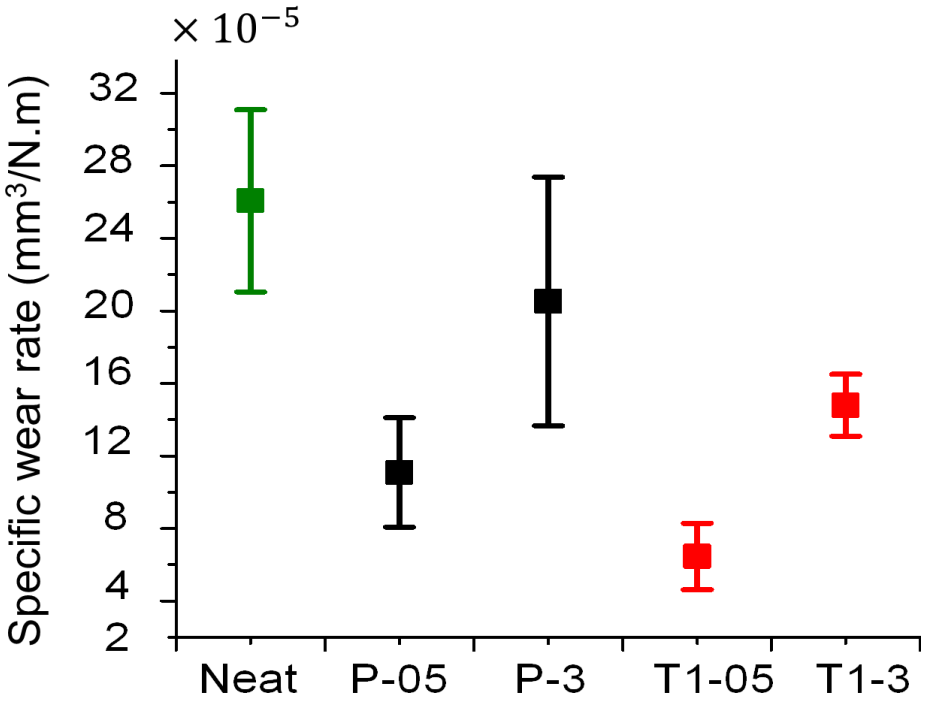

Figure 5.6: The traditional specific wear rate for the five materials.

The variation of the wear volume (ΔV) of a material with time can be expressed as:

$$\Delta V = \dot{w}_m W_w = \dot{w}_m(\Delta E - W_h) = \dot{w}_m(\Delta E - m\Delta E) = \dot{w}_m \Delta E(1-m)$$

$$= [\bar{\mu} N v - \frac{8\pi^2 K_L \Delta T}{D}(1 + \sqrt{\frac{\rho_U \cdot C_U \cdot K_U}{\rho_L \cdot C_L \cdot K_L}})]\, \dot{w}_m \mathrm{t}. \qquad (5.22)$$

In this equation, $\dot{w}_m$ and $\bar{\mu}$ are tribological properties of the materials. Normal load (N), sliding speed (v), the integral number (D) are operational parameters for the wear test. Some physical properties includes the density, thermal capacity, and thermal conductivity of the rubbing materials. The temperature increase (ΔT) at the center of the wear track can be obtained in dry sliding wear test. Therefore, the wear of HDPE and HDPE/CNF nanocomposites can be modelled as a function of time.

The thermal conductivity (K_L) in Equation (5.22) can also be treated as a variable parameter. a relationship between the wear volume and thermal conductivity of a material, for example, HDPE, can be plotted in Figure 5.7. It shows that the wear volume decreases with the

increasing of thermal conductivity, which indicates that with the increasing in thermal conductivity, more friction energy is dissipated with the heat instead of the wear.

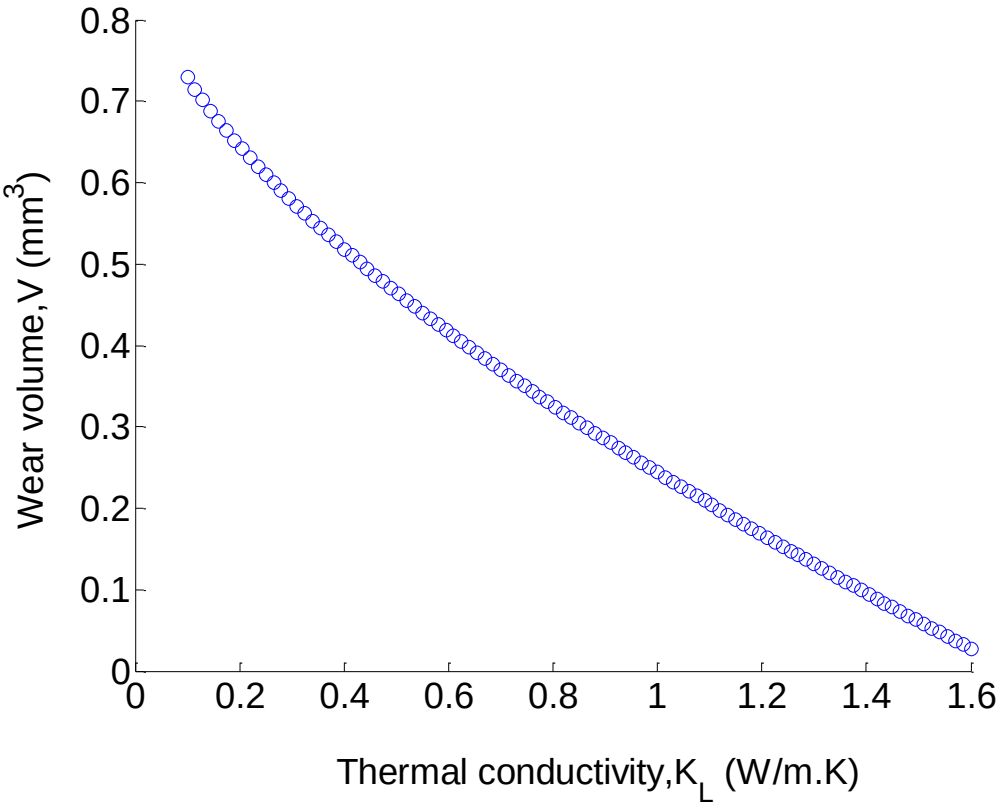

Figure 5.7: Wear volume vs. thermal conductivity.

5.4. Conclusion

In this study, the total friction energy in a pin-on-disc tribological system is analyzed. The study provides with a method to determine the friction energy consumption on heat. Assuming the remaining friction energy is responsible for wear particles generation, a modified specific wear volume is defined to reflect the wear resistance of materials and predict wear loss with time. In addition, it is found that the increased thermal conductivity of lower solid materials can result in more energy dissipated as heat and therefore decreases its wear loss. The wear model can contribute to the understanding of the physics of the wear process from the perspective of friction energy and may be used to predict the long term wear with time.

CHAPTER 6. WEAR MODELING OF HDPE/CNF NANOCOMPOSITES FOR LUBRICATED CONDITIONS

Generally, the wear test of HDPE or UHMWPE under lubricated conditions needs a long time duration to obtain a detectable wear loss, because of their low wear rates. In this chapter, a theoretical model which couples elastohydrodynamic lubrication theory and Reye's wear model is proposed to predict the long term wear of HDPE and HDPE/CNF nanocomposites under lubricated conditions. Dependency of the wear on parameters including viscosity of lubricants, sliding velocity, roughness, coefficient of friction, and normal load are determined. This model is expected to reduce the time consumption of the long term wear test and may provide a helpful support for the biomedical application of the nanocomposites.

6.1. Introduction

The wear modeling of polymeric materials under lubricated conditions is more complicated than that of dry sliding conditions, due to the complex nature of lubrication and the various affecting factors of the wear. However, as mentioned in Chapter 1, the major cause of the revision of total joint replacements is the wear of the polyethylene component. A healthy natural joint works under effective lubricated condition with the synovial liquid as a lubricant resulting in very low friction (COF ranges from 0.003-0.024) [103, 126]. This value of COF is much lower than the values yielded using any artificial bearing materials in equivalent conditions. Therefore, lubrication is an important factor to estimate the wear of the potential bearing material in artificial joints. In addition, Archard's law probably is not appropriate to be used in the wear of polymers under lubricated conditions. However, most of the published studies either neglected the lubrication or applied Archard's law to estimate the wear of UHMWPE component in artificial joints. For example, Wang et al. [127] proposed a wear law for the UHMWPE under lubricated multi-directional sliding conditions without considering

the influence of lubrication. Archard's law was used in the wear modeling in the Ref. [103, 128, 129]. As proven in Chapter 4, instead of Archard's law, Reye's model, which may be more suitable to represent the wear behavior of PE family's material, probably can be applied in the wear modeling of the PE family's materials under lubrication conditions. In this chapter, a wear modeling which coupled Reye's wear model and elastohydrodynamic lubrication theory is built up to predict the long term wear for lubrication conditions.

6.2. Elasto-hydrodynamic lubrication modelling

6.2.1. Formulation and governing equation

The contact between the sliding ball and polymeric disc is three-dimensional which makes it more complex to simulate and investigate the wear behavior of a material. Therefore, some simplifications are necessary. Instead of a ball, we consider a line contact problem with a cylinder sliding against a metal substrate as shown in Figure 6.1. As we do consider the change of the substrate along Z direction in Figure 6.1 are same, the problem is actually transferred into a 2D problem as shown in Figure 6.2. As the cylinder is immersed into lubricants, there is a layer of liquid film between the stainless steel cylinder and the polymeric substrate. The stainless steel cylinder is fixed. At the same time, the polymeric substrate slides along X direction with a constant velocity, *U*, and a normal load, *N*, is applied on the cylinder in Y direction. A pressure in lubricants, therefore, is built up to support the normal load. The pressure distribution thus is different with that of dry sliding wear conditions due to the formation of the liquid film between the cylinder and the polymeric substrate. The film thickness and the pressure distribution are dependent on various parameters, including normal load, viscosity of lubricants, sliding velocity, roughness, and the Young's modulus of two rubbing materials.

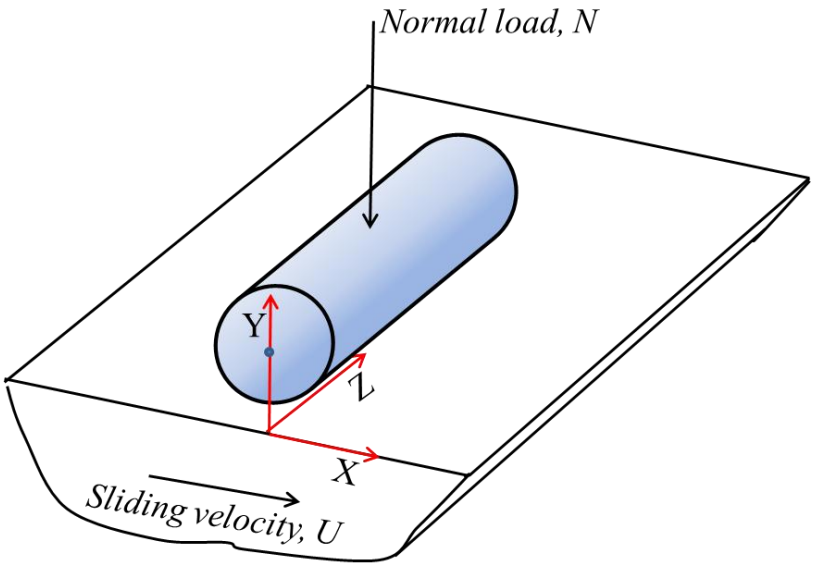

Figure 6.1: Scheme of the 3D line contact problem.

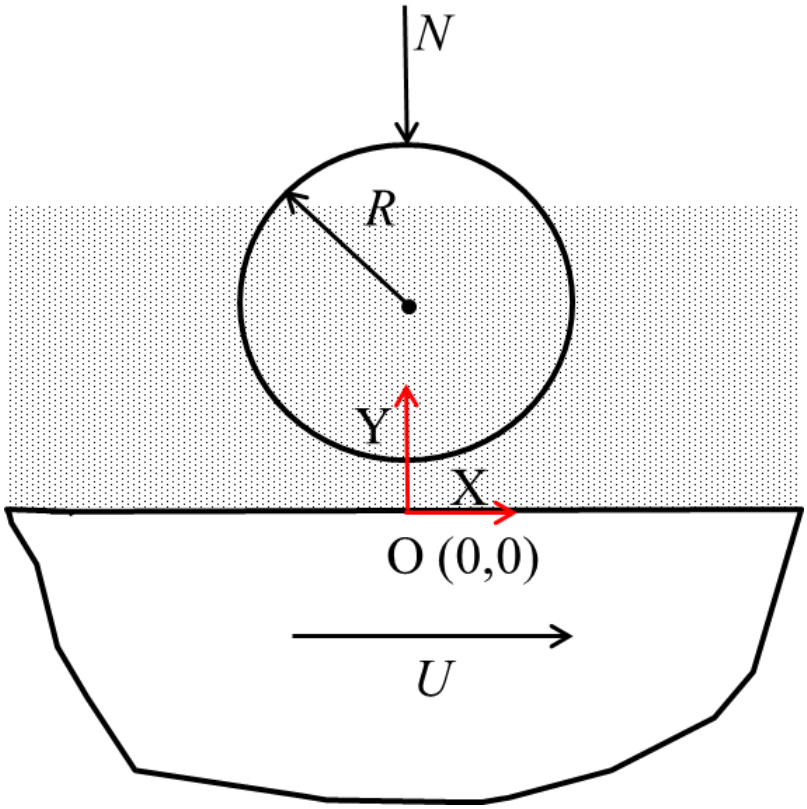

Figure 6.2: Schematic of the simplified 2D line contact problem.

To determine the film thickness and pressure distribution, elastohydrodynamic lubrication (EHL) theory is applied. EHL assumes the elastic deformation of the lubricated surfaces has a substantial influence on the film thickness, which is especially appropriate to the metal-polymer contact due to the low elastic modulus of the polymer compared to metal. In addition, EHL theory also assumes the increase of the lubricant's viscosity due to the high pressure in elastic contacts. Therefore, both the elastic deformation and viscosity changes have a positive influence on the film thickness. Reyonds equation currently is widely employed in EHL theory. Reyonlds equation is, in fact, a simplification of the Navier-stokes equations, assuming that the inertia force can be neglected and lubricants are Newtonian with constant viscosity. The full Reyonds equation in a Cartesian coordinate can be written as:

$$\underbrace{\frac{\partial}{\partial x}\left(\frac{\rho h^3}{\eta}\frac{\partial p}{\partial x}\right)+\frac{\partial}{\partial z}\left(\frac{\rho h^3}{\eta}\frac{\partial p}{\partial z}\right)}_{Poisseuille\ pressure}=\underbrace{6u\frac{\partial(\rho h)}{\partial x}}_{wedge}+\underbrace{6\rho h\frac{\partial u}{\partial x}}_{stretch}+\underbrace{12\frac{\partial(\rho h)}{\partial t}}_{squeeze} \tag{6.1}$$

where

ρ : density of lubricants;

h : film thickness;

p : pressure;

η : viscosity of lubricants

x, z : spatial Cartesian coordinates, in which z refers to dimensions in Z direction in Figure 6.2;

u : the sum velocity of the two rubbing surface;

t : time.

For a line contact problem, the second term in left side of Equation (6.1) can be ignored, as we assume that along Z direction in Figure 6.2, nothing is different. The three terms on the right side of Equation (6.1) represents three potential factors that generate pressure. It should be noted that the second term, the stretch term, referring to the change of the sum velocity on time, can be omitted in this work, as the sliding velocity is a constant here. The third term,

squeeze term, is for the non-steady–flow problems, for example, at the starting up and shutting down stages of the motion or a motion applied a vibration or shock load. However, in a steadily running of a motion, of course, $\frac{\partial h}{\partial t}$ is zero. In this work, as only steady-flow case is considered, the squeeze term can thus be left out and the remaining equation can be given:

$$\frac{\partial}{\partial x}\left(\frac{\rho h^3}{12\eta}\frac{\partial p}{\partial x}\right) = u_m \frac{\partial(\rho h)}{\partial x} \tag{6.2}$$

where $u_m = \frac{u}{2}$.

To solve Reynolds equation, boundary conditions are still needed. It is assumed that the pressure is defined as zero on the left ledges of the pressure influenced domain, then the calculated pressure in the domain is in fact the pressure difference with the ambient pressure. Therefore, one of the boundary conditions is given as:

$$p(x_a) = 0 \tag{6.3}$$

where x_a is a boundary at the inlet of the pressure domain.

Another boundary condition is set at the outlet ($x = x_b$) of the pressure domain, where

$$\frac{\partial p}{\partial x_b} = 0 \tag{6.4}$$

The load balance, therefore, can be given by

$$N = \int_{x_a}^{x_b} p(x)\, dx \tag{6.5}$$

Because of a parabolic profile of the cross-section of the cylinder, a geometrical thickness at a known X location (for example, A(x,0) in Figure 6.3) is given as:

$$h_g = R(1 - (1 - (\frac{x}{R})^2)^{1/2}) \approx \frac{x^2}{2R} \tag{6.6}$$

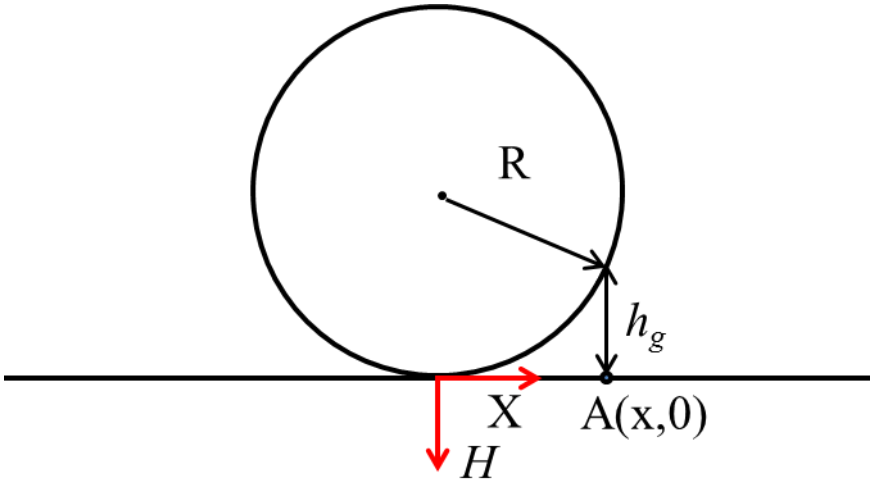

Figure 6.3: Scheme of the geometrical thickness (h_g) of a cylinder in contact with a substrate.

Furthermore, as we know a layer of film is between the two surfaces, a minimum film thickness (h_0) is induced as shown in Figure 6.4.

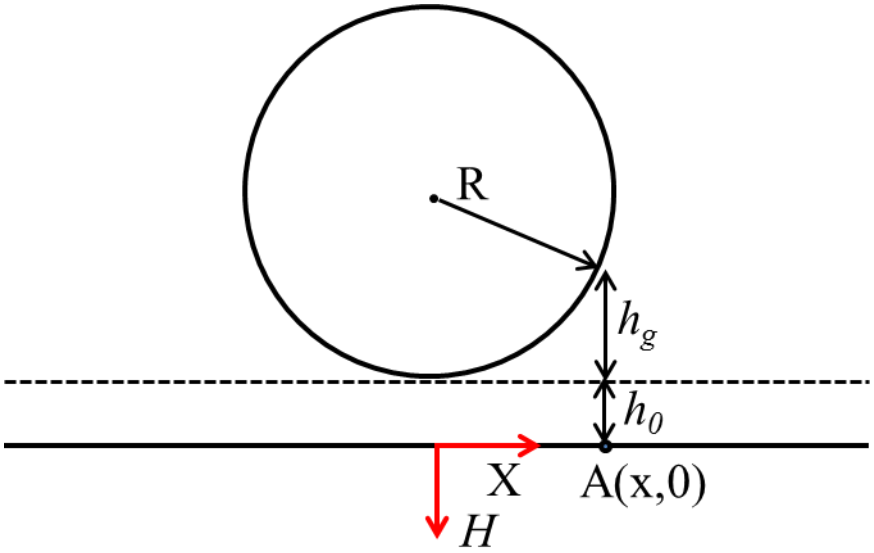

Figure 6.4: Scheme of the minimum thickness (h_0) of a cylinder in contact with a substrate.

When a pressure is applied on a substrate, the surface of the substrate will be deformed. The deformation of the surface is generally determined by its elastic modulus E. The deformation of a surface contacting with a cylinder can be given as in the following [130]:

$$h_e = -\frac{4}{\pi E'}\int_{-\infty}^{\infty} p(s) ln(x-s) ds \tag{6.7}$$

where h_e is the elastic deformation and E' is the reduced elastic modulus, defined as:

$$\frac{1}{E'} = \frac{1}{2}\left(\frac{1-{v_1}^2}{E_1} + \frac{1-{v_2}^2}{E_2}\right) \tag{6.8}$$

with E_1, E_2, the elastic modulus, and v_1 and v_2 Poission's ratio of the two rubbing surfaces, respectively. The elastic deformation is shown in Figure 6.5, where the bottom dashed curve is the profile of the substrate after deformation.

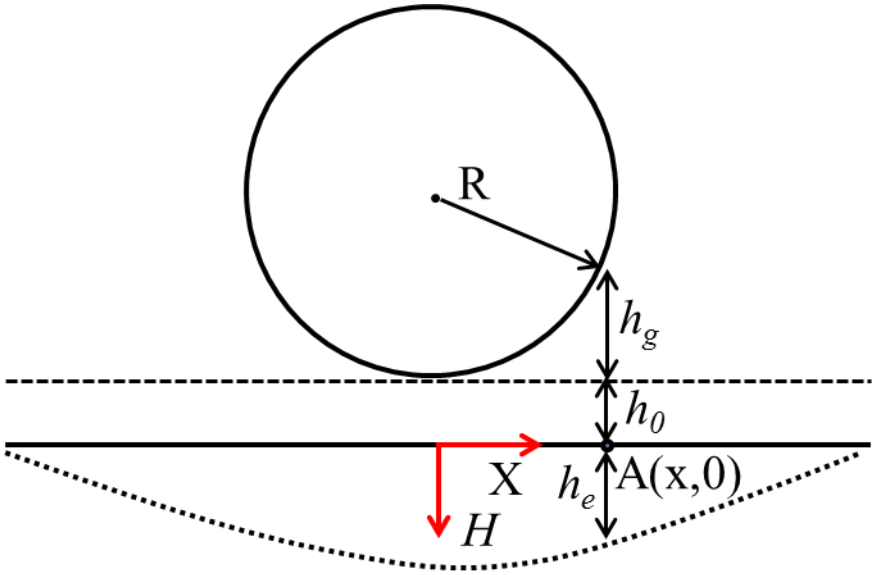

Figure 6.5: Scheme of the elastic deformation (h_e) of a substrate.

In addition, the effect of roughness is also considered in this work, as the substrate is not ideally flat and wear actually begins at the rough asperities. The profile of the deformed rough substrate is shown in Figure 6.5. The roughness of the substrate surface can be measured by a profilometer or atomic force microscopy. In this work, for the mathematical simplification, the surface profile before the elastic deformation is expressed as in the following function:

$$h_r = h_m \sin\left(\frac{2\pi}{\lambda}x\right) \tag{6.9}$$

where h_m is an amplitude of the asperities and λ is the wavelength of the substrate profile. As shown in Figure 6.6, the h_m is in the opposite direction of H. Therefore, total film thickness at a point A(x, 0) can be given as:

$$h(x) = h_0 + h_g + h_e - h_r$$

$$= h_0 + \frac{x^2}{2R} - \frac{4}{\pi E'}\int_{x_a}^{x_b} p(s) ln(x-s) ds - h_m \sin(\frac{2\pi}{\lambda}x) \qquad (6.10)$$

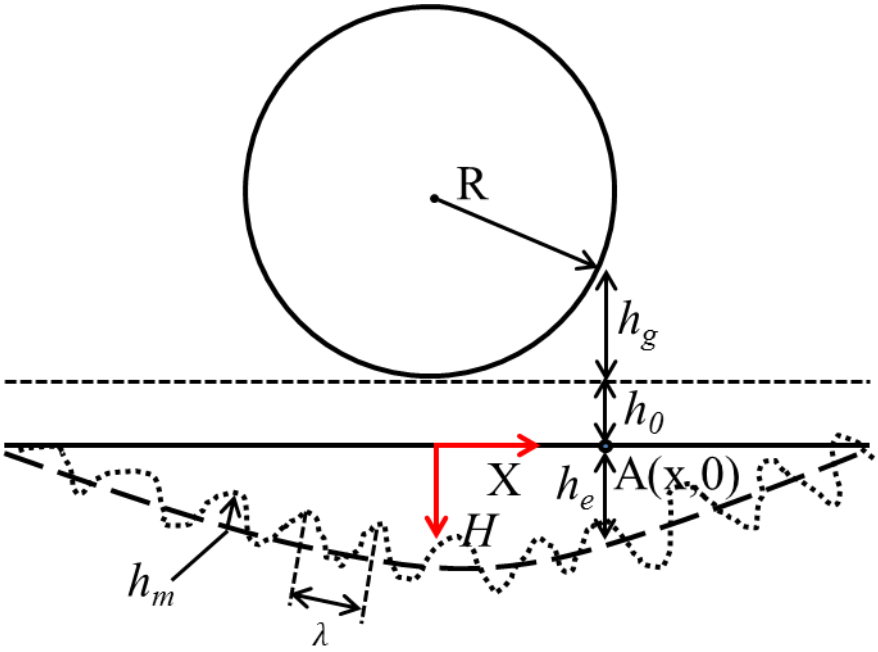

Figure 6.6: Scheme of the elastic deformed substrate surface with consideration of the roughness.

As the viscosity and density of the lubricants are dependent on the pressure, it is necessary to couple the viscosity and density with pressure in Equation (6.11) and (6.12). The Dowson-Higginson density vs. pressure model is given by:

$$\rho(p) = \rho_0 \frac{0.59\times10^9+1.34p}{0.59\times10^9+p} \qquad (6.11)$$

where ρ_0 is the atmospheric density of the lubricant.

The Barus viscosity vs. pressure model is given by:

$$\eta(p) = \eta_0 e^{\alpha p} \qquad (6.12)$$

where η_0 is the viscosity of the lubricant under atmospheric pressure and α is the pressure viscosity coefficient.

Thereafter, the full system of Reylonds equations can be written as:

$$\begin{cases} \frac{\partial}{\partial x}\left(\frac{\rho h^3}{12\eta}\frac{\partial p}{\partial x}\right) = u_m \frac{\partial(\rho h)}{\partial x} \\ h(x) = h_0 + \frac{x^2}{2R} - \frac{4}{\pi E'}\int_{x_a}^{x_b} p(s) ln(x-s) ds - h_m \sin\left(\frac{2\pi}{\lambda}x\right) \\ N = \int_{x_a}^{x_b} p(x)\, dx \\ \rho(p) = \rho_0 \frac{0.59\times10^9 + 1.34p}{0.59\times10^9 + p} \\ \eta(p) = \eta_0 e^{\alpha p} \end{cases} \tag{6.13}$$

with the boundary conditions:

$$\begin{cases} p(x_a) = 0 \\ \frac{\partial p}{\partial x_b} = 0 \end{cases} \tag{6.14}$$

As dimensionless parameters are convenient for mathematical calculation, the dimensional forms of Equation (6.13) and (6.14) are derived with the following dimensionless variables:

$$\begin{aligned} H &= \frac{hR}{b^2} & \bar{N} &= \frac{N}{E'R} \\ U &= \frac{\eta_0 u_m}{E'R} & G &= \alpha E' \\ X &= \frac{x}{b} & P &= \frac{p}{p_H} \\ \bar{\eta} &= \frac{\eta}{\eta_0} & \bar{\rho} &= \frac{\rho}{\rho_0} \end{aligned} \tag{6.15}$$

where $b = (\frac{8}{\pi}\frac{NR}{E'})^{1/2}$, is the radius of the Hertzian contact area, and $p_H = \frac{E'b}{4R}$, is maximum Hertzian pressure.

Then Equation (6.13) and (6.14) can be rewritten as:

$$\begin{cases} \frac{\partial}{\partial X}\left(\frac{\bar{\rho}H^3}{\bar{\eta}}\frac{\partial P}{\partial X}\right) = A_1\frac{\partial(\bar{\rho}H)}{\partial X} \\ H = H_0 + A_2X^2 + A_3\int_{X_a}^{X_b} P(S)ln(X-S)dS - A_4\,\overline{\mathrm{Hm}}\,\sin\left(\bar{\lambda}X\right) \\ A_5 = \int_{X_a}^{X_n} PdX \end{cases} \tag{6.16}$$

where

$$A_1 = \frac{3}{4}\frac{\pi^2U}{\bar{N}^2}, \quad A_2 = -\frac{1}{2\pi}, \quad A_3 = \frac{1}{2}, \quad A_4 = 1, \quad A_5 = \frac{\pi}{2}. \tag{6.17}$$

The boundary conditions are:

$$\begin{cases} P(X_a) = 0 \\ \frac{\partial P}{\partial X_b} = 0 \end{cases} \tag{6.18}$$

6.2.2. Numerical solution of a line contact problem

In numerical analysis, Newton-Raphson method is an efficient method for solving nonlinear problems. To apply Newton's method to the Reynolds equation, Equation (6.16) can be rewritten as:

$$\begin{cases} F_1(P,H_0) = \frac{d}{dX}\left(\frac{\bar{\rho}H^3}{\bar{\eta}}\frac{\partial P}{\partial X}\right) - A_1\frac{d(\bar{\rho}H)}{dX} = 0 \\ F_2(P,H_0) = \int_{X_a}^{X_n} PdX - A_5 = 0 \end{cases} \tag{6.19}$$

where $\bar{\eta} = \bar{\eta}(P)$, $\bar{\rho} = \bar{\rho}(P)$ and $H = H_0 + A_2X^2 + A_3\Pi(P) - A_4\sin(\lambda X)$; $\Pi(P)$is an integral operator, $\Pi(P) = \int_{X_a}^{X_b} P(S)ln(X-S)dS$. The boundary conditions are the same with Equation (6.18). After expanding the functions $F_1(P,H_0)$ and $F_2(P,H_0)$ into Taylor's series about a guess solution (P_{00},H_{00}), the values of $F_1(P,H_0)$ and $F_2(P,H_0)$ function can be expressed as:

$$\begin{cases} F_1(P,H_0) = F_1(P_{00},H_{00}) + \frac{d\,F_1}{\partial P}(P_{00},H_{00})\Delta P + \frac{d\,F_1}{\partial H_0}(P_{00},H_{00})\Delta H_0 = 0 \\ F_2(P,H_0) = F_2(P_{00},H_{00}) + \frac{d\,F_2}{dP}(P_{00},H_{00})\Delta P + \frac{d\,F_2}{dH_0}(P_{00},H_{00})\Delta H_0 = 0 \end{cases} \tag{6.20}$$

Combining Equation (6.19) with Equation (6.20), we obtain:

$$\frac{d}{dX}\left[\frac{\bar{\rho}H^3}{\bar{\eta}}\frac{d(\Delta P)}{dX}\right]+\frac{d}{dX}\left[\left(-\frac{1}{\bar{\eta}^2}\frac{d\bar{\eta}}{dP}\bar{\rho}H^3\frac{dP_{00}}{dX}+\frac{\partial\bar{\rho}}{\partial P}\frac{H^3}{\bar{\eta}}\frac{dP_{00}}{dX}-A_1\frac{d\bar{\rho}}{dP}\right)\Delta P\right]$$

$$+\frac{d}{dX}\left[(3\frac{\bar{\rho}H^3}{\bar{\eta}}\frac{dP_{00}}{dX}-A_1\bar{\rho})\Pi(\Delta P)\right]+\frac{d}{dX}\left[(3\frac{\bar{\rho}H^2}{\bar{\eta}}\frac{dP_{00}}{dX}-A_1\bar{\rho})\Delta H_0\right]$$

$$=\frac{d}{dX}\left[-\frac{\bar{\rho}H^3}{\bar{\eta}}\frac{dP_{00}}{dX}+A_1\bar{\rho}H\right] \tag{6.21}$$

and

In Equation (6.21) and (6.22), when a guess value of P_{00} and H_{00} are known, $\bar{\rho}$, $\bar{\eta}$, H,

$$\int_{x_a}^{x_b}\Delta P dx=A_5-\int_{x_a}^{x_b}P_{00}dx \tag{6.22}$$

and $\frac{dP_{00}}{dX}$ can be directly calculated. Thereafter, based on the viscosity vs. pressure and density vs. pressure relationship in Equation (6.11) and (6.12), $\frac{d\bar{\eta}}{dP}$ and $\frac{d\bar{\rho}}{dP}$ can be determined also. The only unknown parameters are ΔP and ΔH_0. The pressure domain at $[x_a, x_b]$ can be divided into n elements and each element with 2 nodes. The ΔP on the i[th] element is ΔP_i $(i=0,1,2,\dots,n)$. Pulsing ΔH_0, we can obtain a system of equation:

$$[J]_{(n+2)\times(n+2)}\begin{Bmatrix}\Delta P_i\\ \Delta H_0\end{Bmatrix}=\{F_i\} \tag{6.23}$$

In Equation (6.23), ΔP and ΔH_0 at each X node can be determined. The above method is called finite element Newton's method. The detailed procedures can be referred to in the Ref. [131]

After ΔP and ΔH_0 are known, new P and H_0 are updated as:

$$\begin{cases}P(X_i)=P_{00}\,(X_i)+\Delta P(X_i)\\ H_0(X_i)=H_{00}(X_i)+\Delta H_0(X_i)\end{cases} \tag{6.24}$$

The new obtained P and H_0, then are used as the new guess value of P_{00} and H_{00} in Equation (6.23) and the loop repeats several times until $\|\Delta P\|\to 0$ and $\|\Delta H_0\|\to 0$. This method has very short computation time. The error can be reduced an order of magnitude in each loop and generally only 6-10 loops may reach the required error range.

6.3. Wear modeling under lubricated conditions

6.3.1. Wear law

The ability to predict wear and lifespan of a material is essential for its tribological application, because the eventual purpose of tribological study is to protect surface against wear. The lubrication itself is a just a method to decrease wear. Archard's law is very frequently used in the wear modelling and can be expressed as:

$$\frac{\mathrm{V}}{L} = K_a \frac{N}{H} \tag{6.25}$$

where V is the volume of the worn off material, L is sliding distance, K_a is a constant, N is the normal load, and H is the hardness of the softer material in the two rubbing bodies. The hardness, H, is usually bundled up into a single coefficient K_a. Both sides of the equation are divided by the contact area, then Equation (6.25) is:

$$\frac{\mathrm{h}}{L} = K_a \mathrm{p} \tag{6.26}$$

The wear process is considered as dynamic and the wear depth change with respect to each distance increment, therefore, the first order differential form of Equation (6.26) is:

$$\frac{\Delta \mathrm{h}}{\Delta \mathrm{L}} = K_a \mathrm{p}(\Delta \mathrm{L}) \tag{6.27}$$

Here the contact pressure is a function of the sliding distance which is considered as the time in the dynamic process of wear.

However, as discussed in Chapter 4, Archad's law may not be appropriate for the wear of polymer under lubricated conditions. A new proposed wear law is given in Chapter 4 as:

$$\frac{V}{L} = K\bar{F} \tag{6.28}$$

where K is a constant and $\bar{F}$ is the average friction force. As $\bar{F}$ can be expressed as a product of the COF (μ) and the normal load (N) based on the definition of COF, Equation (6.28) is rewritten as:

$$\frac{V}{L} = K\bar{\mu}N \tag{6.29}$$

Similar with Equation (6.27), the change of wear depth can be determined as:

$$\frac{\Delta \mathrm{h}}{\Delta \mathrm{L}} = K\bar{\mu}p(\Delta \mathrm{L}) \tag{6.30}$$

Although Equation (6.27) and (6.30) seem very similar with only difference of $\bar{\mu}$ term, they represent two distinct methods. Equation (6.30) is believed to be appropriate to be used in lubricated conditions, as K in Equation (6.30) only represents the material properties. The different lubricants have significant influence on the COF which can be represented by the average COF. The COF under a specific lubricant is easily obtained or even measured in a very short wear test duration. If using Equation (6.25) in lubricated conditions, even with the same material, a specific K_a has to be given for a certain lubricated condition. Therefore, in this work, Equation (6.30) is used to the wear modeling under lubricated condition.

6.3.2. Wear simulation

From Equation (6.30), a numerical solution can be derived with a finite difference of the wear depth as following:

$$h_j - h_{j-1} = K\bar{\mu}p_j(\Delta \mathrm{L})\Delta \mathrm{L}_j \tag{6.31}$$

where h_j is the wear depth at jth iteration while $h_{j-1}$is the wear depth at the pervious iteration. $K\bar{\mu}p_j(\mathrm{L})\Delta \mathrm{L}_j$ refers to the incremental wear depth, which is a function of the incremental sliding distance, the contact pressure at the corresponding sliding distance and the average COF. The term of $p_j(\mathrm{L})\Delta \mathrm{L}_j$ can be already determined from the lubrication modelling in Section 6.2. For each increment of $\Delta \mathrm{L}_j$, $p_j(\mathrm{L})\Delta \mathrm{L}_j$ is actually the integral of $p(x)$ with x. It can be expressed as following:

$$p_j(\mathrm{L})\Delta \mathrm{L}_j = \int_{x_a}^{x_b} p(x)dx \tag{6.32}$$

After the incremental wear depth is known, the incremental wear volume is calculated by multiplying the incremental wear depth with the length (l) of the cylinder in Figure 6.1. Therefore, an accumulation of the incremental wear volume for all iterations (n) can be given as:

$$V = \sum_{j=1}^{n} \Delta V_j = l \sum_{j=1}^{n} \Delta h_j \, \Delta L_j = l \sum_{j=1}^{n} (h_j - h_{j-1}) \Delta L_j \tag{6.33}$$

where b is the radius of the Hertzian contact area.

With the wear depth accumulated in each iteration, the sliding distance is also an accumulation of the incremental sliding distance for all iterations (n) and is given as:

$$L = \sum_{j=1}^{n} \Delta L_j \tag{6.34}$$

Therefore, the wear depth on a contact surface for a specified sliding distance L can be estimated. It is noted that Equation (6.33) is appropriate for the case that the soft material is continuously worn off. For example, in the tribology system in Chapter 4, the polymer pin is stationary and continuously worn against the sliding metal disk. However, in Chapter 3 and this Chapter, the polymer disk is rotated against the stainless steel pin, which means in each rotation period, an asperity only contacts with the stainless steel pin once. Therefore, for the tribology system in this Chapter, the accumulation of the incremental sliding distance can be calculated as following:

$$L = 2\pi r \sum_{j=1}^{n} j \tag{6.35}$$

where r is the radius of wear track. In future wear modelling, Equation (6.35) will be used.

As we know, in each rotation, only a very tiny wear depth is generated resulting in a very small geometric change. For shortening the computation time, the incremental wear depth

in Equation (6.30) can be defined as the incremental wear depth in every N rotations period, and then Equation (6.30) can be rewritten as:

$$h_j - h_{j-1} = NK\theta\bar{\mu}p_j(\Delta \mathrm{L})\Delta \mathrm{L}_j \tag{6.36}$$

where θ is the frequency of a rotation with unit of Hz.

Thereafter, the accumulation of the incremental sliding distance (Equation (6.35)) can be reformed as:

$$L = 2\pi r\theta Nj \ (j = 1,2,3,\dots,n) \tag{6.37}$$

If we let N=3600, the incremental wear depth ($h_j - h_{j-1}$) is actually the wear depth change in an hour. n is therefore the duration hours of the wear test.

The accumulation of the incremental wear volume for all iterations (n) can be given as:

$$V = \sum_{j=1}^{n} \Delta \mathrm{V}_j = \begin{cases} \sum_{j=1}^{n} (h_j - h_{j-1}) \cdot \left(2\pi r.\frac{h_j}{2h_m}\right) \cdot \left(2R.\frac{h_j}{2h_m}\right) & h_j < 2h_m \quad (6.38a) \\ \sum_{j=1}^{n} (h_j - h_{j-1}) \cdot (2\pi r) \cdot (2R) & h_j > 2h_m \quad (6.38b) \end{cases}$$

The induced term of $\left(2\pi r.\frac{h_j}{2h_m}\right)$ in Equation (6.38) refers to the real worn-off distance. As the wear track has a length of $2\pi r$, there are M number of asperities along this wear track, where M is :

$$M = \frac{2\pi r}{\lambda} \tag{6.39}$$

The λ is the wavelength of a asperity. Then the real worn off distance for each asperity at the j^{th} iteration, d_j shown in Figure 6.7, can be given as:

$$d_j = \frac{h_j}{2h_m}\lambda \tag{6.40}$$

where h_m is the average height of the asperities. Therefore, the real worn-off distance (s_j) along the wear track at the j^{th} iteration is:

$$s_j = Md_j = \frac{2\pi r}{\lambda}\frac{h_j}{2h_m}\lambda = 2\pi r.\frac{h_j}{2h_m} \tag{6.41}$$

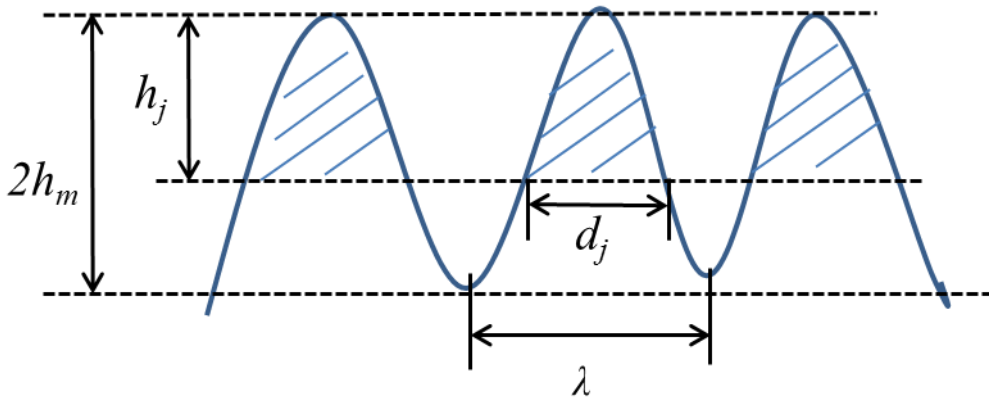

Figure 6.7: Scheme of the geometry of asperities.

Similarly the real worn-off distance on the direction of the arc of the contact ball also needs to be multiplied with $\frac{h_j}{2h_m}$. However, when $h_j > 2h_m$, the real worn surface will equal to $2\pi r$, as shown in Equation (6.38). At each iteration, the geometry of asperity is updated in the lubrication modeling to compute a new pressure distribution and thereafter a new cycle commences. To update the geometry of asperity, the film thickness equation in the lubrication modelling at each iteration is given as:

$$h(x) = \begin{cases} h_0 + \frac{x^2}{2R} - \frac{4}{\pi E'}\int_{x_a}^{x_b} p(s)ln(x-s)ds - \frac{2h_m - h_j}{2}\sin(\lambda x) & h_j < 2h_m \quad (6.42a) \\ h_0 + \frac{x^2}{2R} - \frac{4}{\pi E'}\int_{x_a}^{x_b} p(s)ln(x-s)ds & h_j > 2h_m \quad (6.42b) \end{cases}$$

The flow chart for the wear simulation is shown in Figure 6.8.

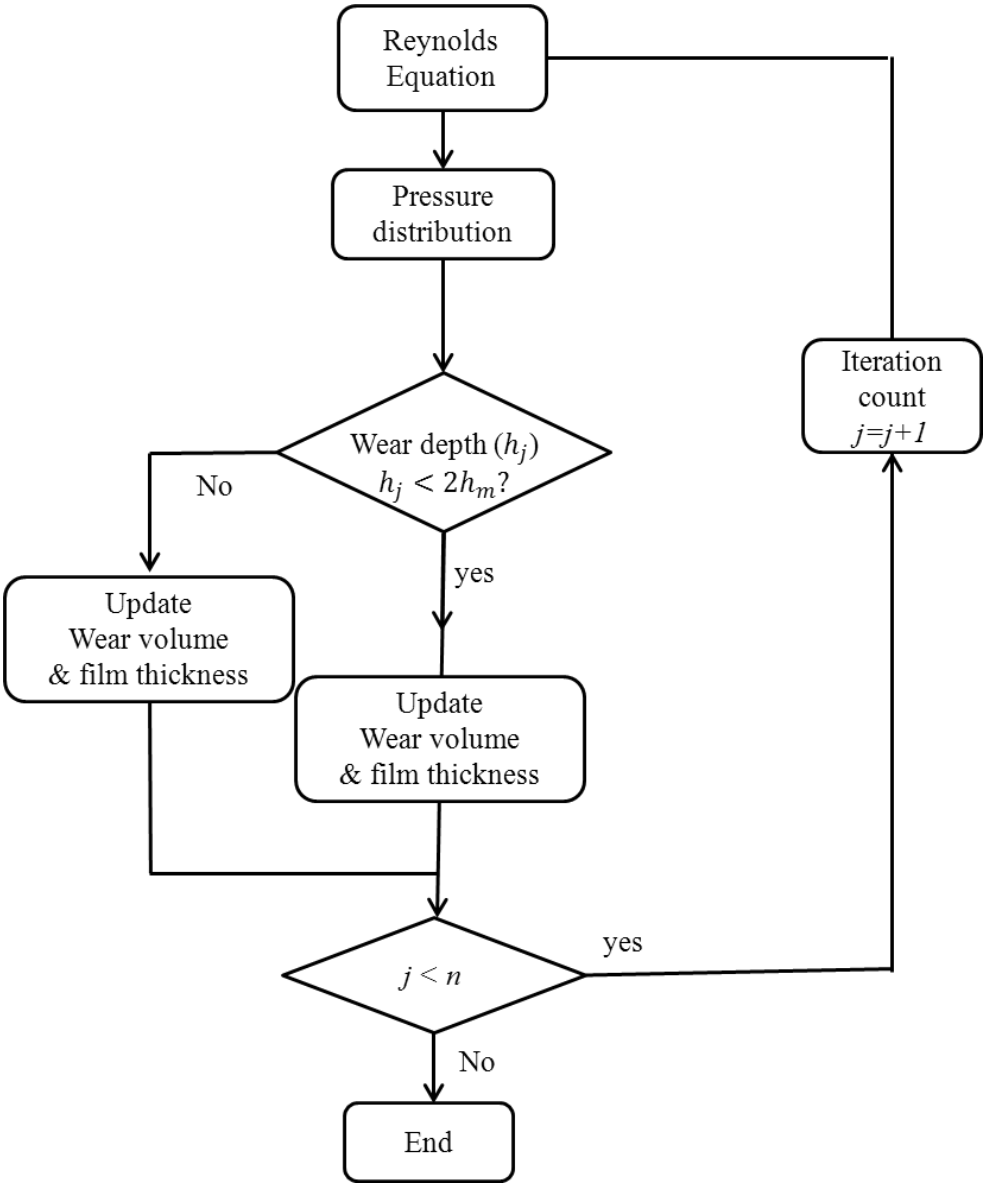

Figure 6.8: Wear simulation flow chart.

6.3.3. Experimental measurements

To determine the specific wear volume of HDPE (K), a pin-on-disk (polymer pin sliding on stainless steel disk) wear test was performed under the 95% glycerol/water lubricated condition. The wear test apparatus is the same with the one used in Chapter 4 as shown in Figure 4.1. The diameter of the HDPE and T1-05 pin is 6.35mm. Normal load and sliding

speed were set as 100N and 31.4mm/s. The mass loss after 24, 48, 72, and 96 hours of wear testing were measured. As proven in Chapter4, the relationship between wear rate and average friction force under lubricated conditions can be expressed as:

$$\Delta V = K\bar{\mu}N\Delta L \tag{6.43}$$

The fitting curves of the pin-on-disk wear test data are determined to find the specific wear volume (the slope of the fitting curves) for HDPE and T1-05 in Figure 6.9. The results show that the specific wear volume (K) of HDPE and T1-05 are 9.8×10^{-6} mm^3/m and 4.2×10^{-6} mm^3/m, respectively.

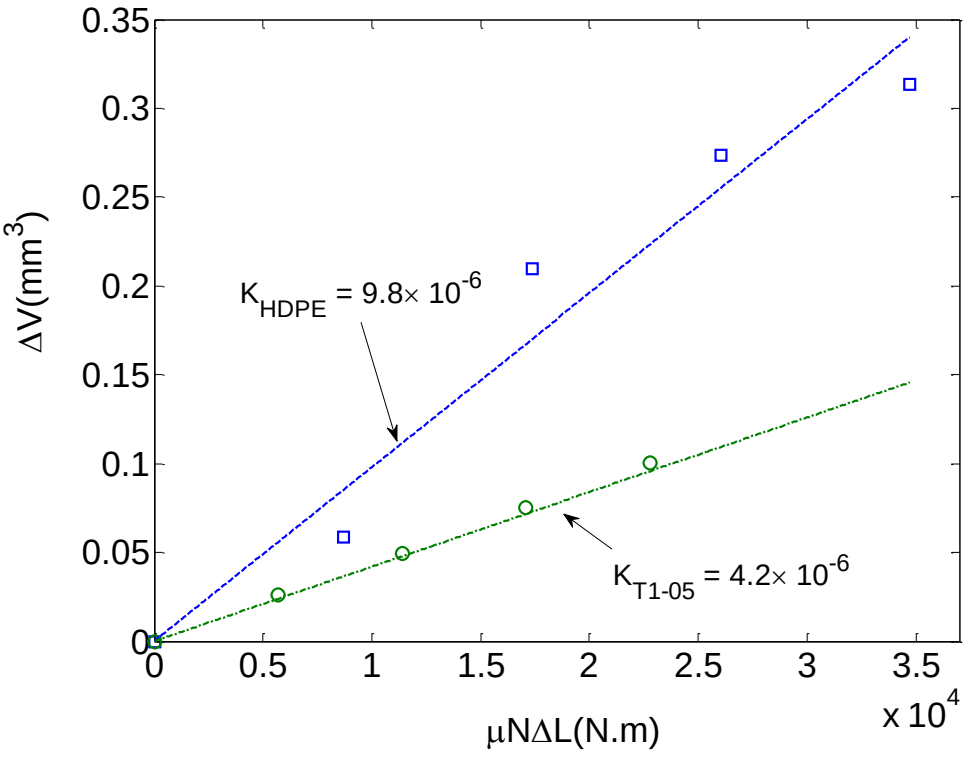

Figure 6.9: The input specific wear volume (K) of HDPE and T1-05 materials.

To validate the wear modeling for the line contact problem, another pin-on-disk (a stainless steel cylinder sliding against a HDPE disk) wear test is also performed under 95%

glycerol/water lubricated conditions as shown in Figure 6.10. The stainless steel cylinder with length of 4.76 ±0.002mm has a circular cross-section with a radius of 2.38±0.001mm. The radius of wear track is 5 mm. The mass loss of the polymer disk is measured in every 2 hours. The COF is monitored continuously during the wear test. In addition, the normal load, rotation frequency and average initial asperity height is varied for different samples in Table 6.1. COFs of HDPE under various operating parameters are measured in a 1-hour wear tests and also listed in Table 6.1.

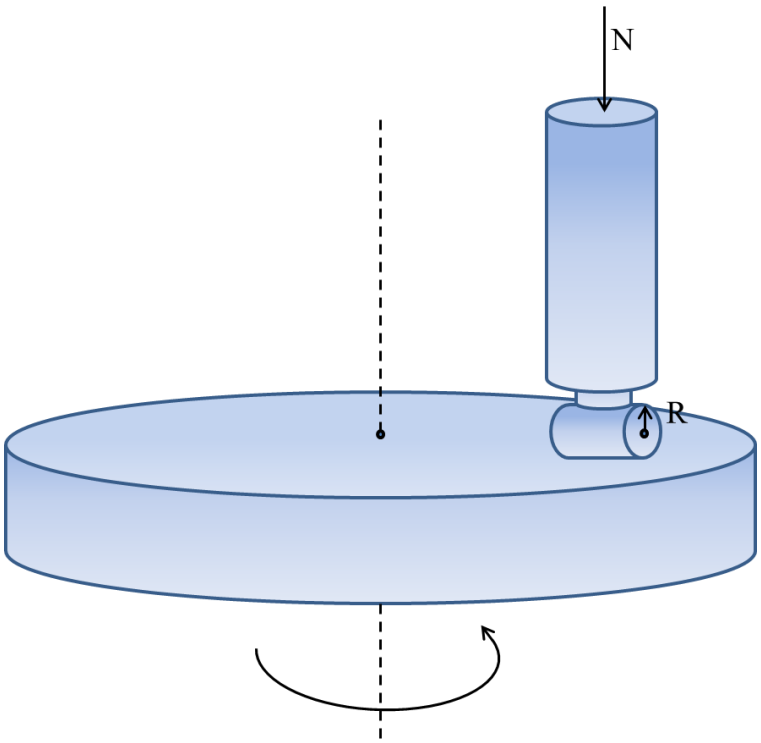

Figure 6.10: Scheme of a line-contact pin-on-disk wear test.

Table 6.1: The wear simulation data set-ups.

Simulation data set No.	Lubricants	Viscosity of lubricants, η (Pa.s)	Rotation frequency, θ (Hz)	Normal load, N (N)	Average asperity height of polymer disk, h_m (μm)	Average COF, μ
1	50% Glycerol	0.00496	1	50	0.24	0.042
2	50% Glycerol	0.00496	2	50	0.24	0.043
3	50% Glycerol	0.00496	1	100	0.24	0.030
4	50% Glycerol	0.00496	1	50	0.50	0.042
5	95%Glycero	0.36440	1	50	0.24	0.031
6	Water	0.00089	1	50	0.24	0.072

6.3.4. Results and disscussion

As shown in Figure 6.11, the experimental mass loss measurements are compared to the simulated results. The parameters in both experiments and simulation are set up as Set No. 1 as shown in Table 6.1. Both experimental and simulated curves have similar parabolic shape. The simulated results have a good agreement with the test data. At the first stage (about 0-24 hours), the mass loss slowly increases with time due to the wear of the asperities. After around 24 hours, the mass loss of HDPE steeply increases and the curve in this second stage becomes a basic straight line with a constant slope. The transition time from the first stage to the second stable stage represents the moment at which the asperity is entirely worn off. The first stage difference of the mass loss between the experimental and simulated curves is small. However, after around 24 hours, the difference becomes larger and larger due to the different slope of the straight lines in the second stage. This may be due to our ideal assumption that after the asperities are worn off, the work surface of the polymer will become prefect smooth surface.

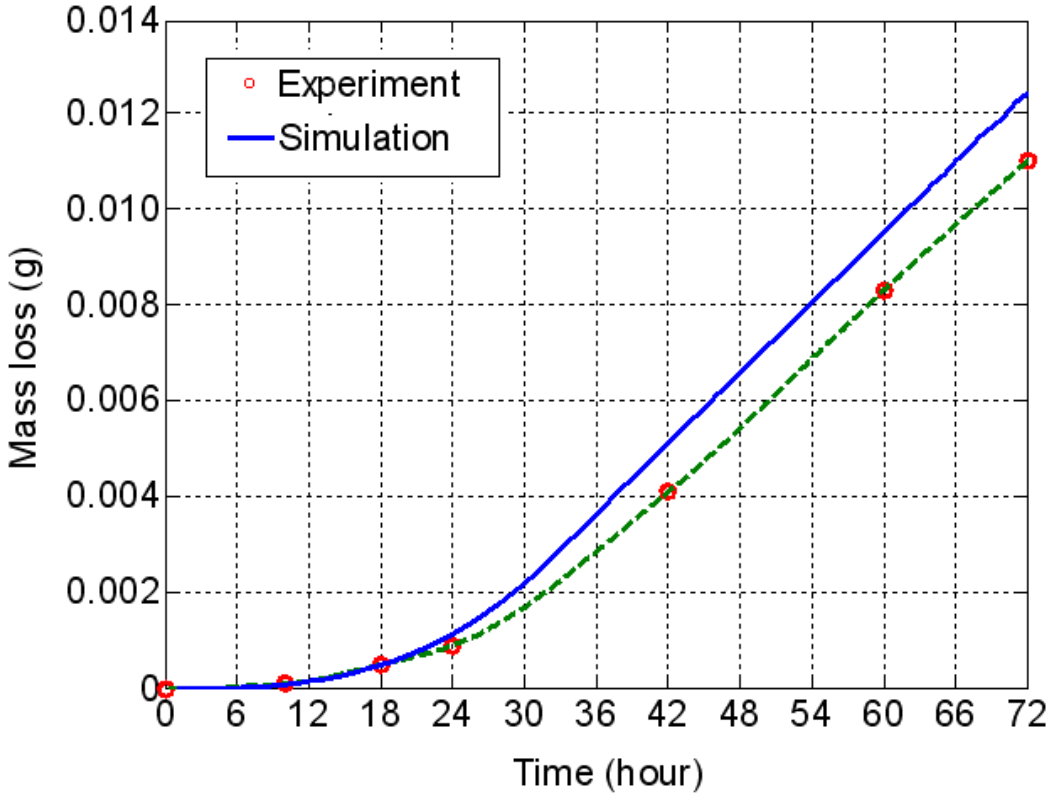

Figure 6.11: Comparison of experimental wear measurements with simulation results (Parameters were set as Set No.1 as shown in Table 6.1).

The dependence of the mass loss of HDPE on the rotation frequency, normal load, average asperity height and lubricants are illustrated in Figure 6.12. The increasing rotation frequency, which results in a corresponding increase in sliding speed, significantly increases the generation of mass loss (Figure 6.12 (a)). If the rotation frequency is doubled, the contact possibility between an asperity of the substrate and the stainless steel pin is improved twice and results in a significant increase of the mass loss. In addition, it also considerably shortens the transition time from the first stage to the second stage. As shown in Figure 6.12, the mass loss of HDPE increases with the increasing of the normal load from 50N to 100 N. This is mainly due to the fact that the more the normal load, the higher the pressure. Compared to the two curves in Figure 6.12(c), the increased asperity height seems to significantly prolong the transition time from the beginning stage to the second stage and lower the mass loss. This is

because of the geometry assumption of the asperity and the influence of the asperity height on pressure distribution. However, it should be noted that after the transition from the beginning stage to the second stage occur and the asperities are entirely worn off, the slopes of the two curves in Figure 6.12(c) are the same as each other. In Figure 6.12(c), the mass loss vs. time curves under different lubricants are plotted. Because the different lubricants have various viscosity and result in different COFs, the significantly different mass loss curves were obtained. It can be seen that compared to the other two lubricated conditions, the HDPE under the water lubricated condition yields the highest mass loss over time and has the shortest transition time from the beginning stage to the stable stage. Thus, it is concluded that the wear of a material under lubricated conditions is significantly influenced by the sliding speed, normal load, roughness, and lubricants properties. The present computational modeling taking all the above parameters into consideration has good capability to model the wear of a polymeric material.

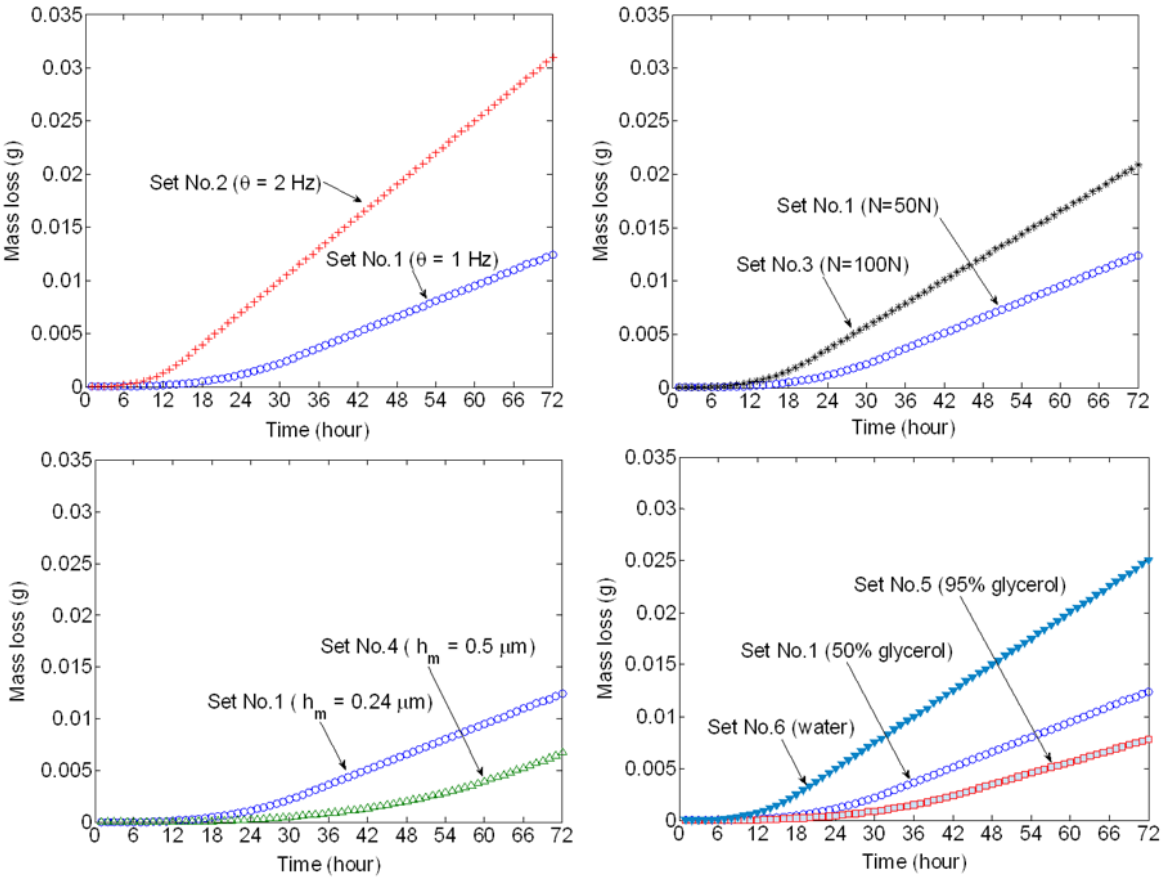

Figure 6.12: Dependence of the mass loss of HDPE on various parameters: (a) rotation frequency; (b) normal load; (c) average asperity height; and (d) lubricants.

The specific wear volume, COF under the 50% glycerol lubricated condition and Young's modulus of HDPE and T1-05 nanocomposite are applied in the wear simulation of each material. The simulated results of two materials are shown in Figure 6.13. It can be seen that the proposed wear model can successfully predict the mass loss of different materials during the long term wear. Because the specific wear volume of T1-05 is reduced significantly (Figure 6.9) due to the reinforcement of thicker-silane treated CNFs, with the same time the mass loss of T1-05 generally is lower than that of HDPE.

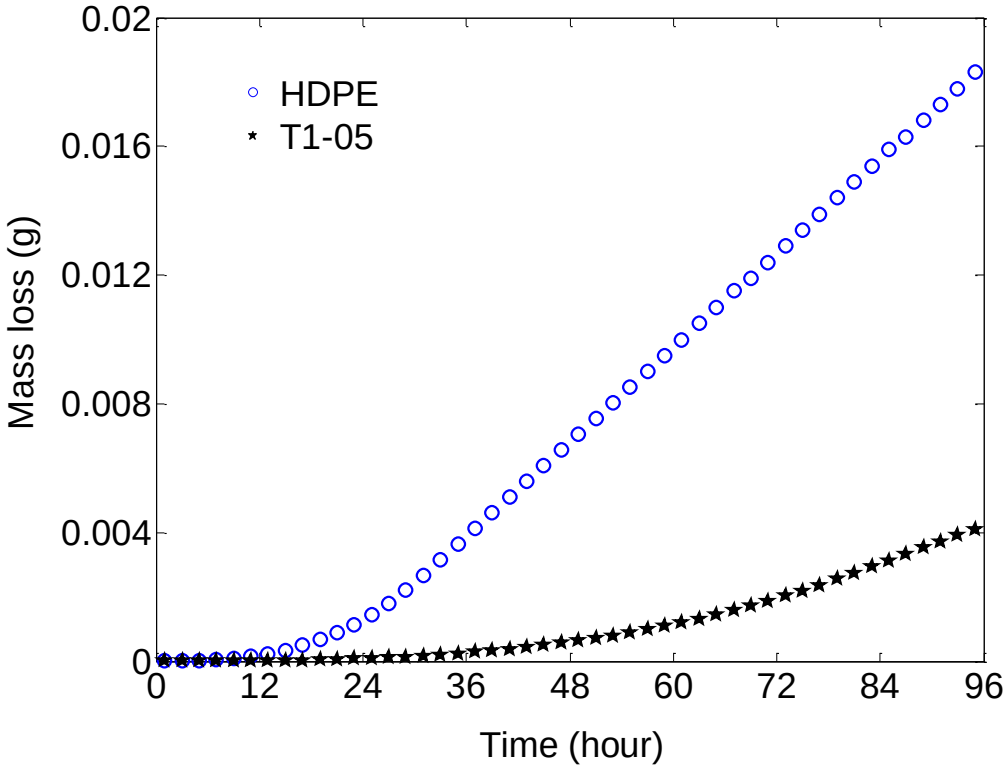

Figure 6.13: Comparison of the mass loss of the HDPE and thick-silane treated CNF reinforced HDPE at 0.5 wt% loading (T1-05) over time.

6.4. Conclusion

In this work, a wear model under lubricated conditions is developed with incorporation of elastohydrodynamic lubrication theory and Reye's wear model. Various affecting factors on wear are considered including lubricants' property (viscosity), material properties (Young's modulus, asperity height, specific wear volume, and coefficient of friction), and operating parameters (normal load and sliding speed). The Newton-Raphson method is used to solve the line contact lubrication problem with time consumption of several seconds which proves that the numerical solver is robust and has a high convergence rate. The wear simulation shows that the wear of HDPE is increased with the increasing of the sliding speed and normal load, but decreased with the increasing of the asperity height and lubricant's viscosity. The wear model

can be used to predict the long term wear under lubricated condition and may reduce the time consumption of the wear test.

CHAPTER 7. SUMMARY AND RECOMMENDATIONS FOR FUTURE WORK

7.1. Summary

This dissertation focused on the tribological studies of HDPE/CNF nanocomposites. In particular, three types of CNFs have been added into the HDPE polymer matrix, including pristine CNFs and silane coated CNFs at different loading levels (0.5 wt.%, 1 wt.% and 3 wt.%). Silane coatings of thicknesses of 2.8 nm (thin) and 46 nm (thick) were applied on the surfaces of CNFs to improve the interaction between the CNFs and the matrix.

The mechanical and thermal properties of the nanocomposites were measured. It was found that the addition of CNFs led to an enhancement of the ultimate stress, fracture strain, and hardness compared with the neat HDPE. Thermal conductivity measurements reflected an 18% improvement in the nanocomposite reinforced with thick-silane treated CNFs at 3 wt.% loading. The tribological behaviors of the nanocomposites under dry sliding, saline water lubricated, and bovine serum lubricated conditions were investigated. Compared with the neat HDPE, the friction coefficients of the nanocomposites were reduced in all samples under all test conditions. CNFs with thicker-silane coatings at lower concentration levels, yielding the lowest wear rate in all three conditions, have the potential to serve as promising reinforcements for HDPE to achieve improved tribological property of the nanocomposites.

The correlations of the wear with friction, hardness, work of fracture, thermal conductivity of a polymeric material were explored. The wear rate of the nanocomposite was found to have a weak correlation with the microhardness, but linearly relate to the work of fracture or the product of ultimate strength and strain at fracture. The increase of thermal conductivity of a material positively contributed to the reduction of its wear volume. In addition, two distinguished linear relationships were found between the wear rates of LDPE, as well as UHMWPE, and their respective friction forces, possibly due to the different wear modes. The relationship between the wear rate and the friction force of a polymeric material

can be used to predict the long term wear of the material under lubricated conditions in terms of a measured friction force from a short wear test.

A thermal analysis method was proposed to determine the friction energy consumption on heat for a pin-on-disk tribo-system in dry sliding condition. A modified specific wear volume was defined to reflect the wear resistance of materials and predict the long term wear with time. In addition, a wear model for lubricated condition was developed with the incorporation of elastohydrodynamic lubrication theory and Reye's wear model. The wear was increased with increasing sliding speed and normal load, but decreased with the increase in roughness and lubricant's viscosity. These wear models contribute to the understanding of the physics of wear and the reduction of time consumption of the wear test in order to predict the long-term wear behavior.

7.2. Recommendations for future work

This work can be viewed as a preliminary study of the HDPE/CNF nanocomposites for tribological applications. Many new areas have not been explored and some points from this dissertation need to be further clarified. Some suggestions for future research are presented below:

(1)*Wear test.* Various pin-on-disk tribo-systems were selected to characterize the wear rate of a polymer against a metal in this dissertation, including a metal pin with a sphere end against a polymeric disk (Figure 7.1(a)), a metal pin with a cylinder end against a polymeric disk (Figure 7.1(b)), and a polymer pin with a flat end against a metal disk (Figure 7.1(c)). The tribo-systems in Figure 7.1(a) and Figure 7.1(b) correspond to the point contact solution and line contact solution respectively in the elastohydrodynamic lubrication theory. However, the third tribo-system to characterize the wear rate of the polymers in Figure 7.1(c) is recommended for the future work.

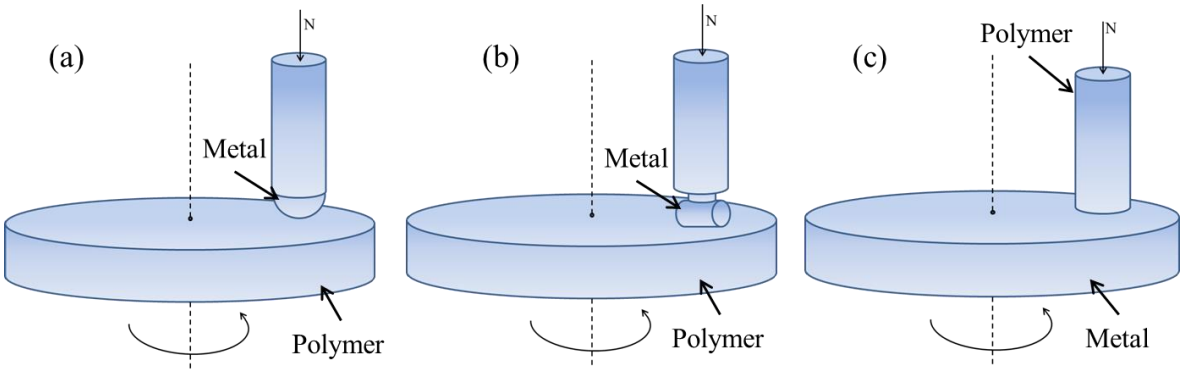

Figure 7.1: Various tribo-systems in the pin-on-disk wear test.

The third one has several advantages: First, the flat end shape of the polymer pin is easy to approach. Second, in the third tribo-system, the entire contact surface of the polymer pin is continuously worn off during the wear test which may speed up the wear test to obtain a detectable wear volume. However, in the first two tribo-systems only a portion of the polymer disk contacts the metal pin. Third, because of the flat end, the contact surface of the polymer pin experiences a uniform normal pressure. The volume-based wear rate (wear volume per unit sliding distance) in this tribo-system can be translated into a depth-based wear rate (wear depth per unit sliding distance). The latter one is very important in the wear simulation of the complex contact problems (for example, the area contact and line contact problem in Figure 7.1(a) and Figure 7.1(b), respectively) to update the geometry change in each rotational period. In addition, the volume-based wear rate of Figure 7.1(c) can also be translated into normalized wear rate with respect to the normal load, N, which makes the experimental results comparable with the reported data in literature. However, the experimental results in the first two tribo-systems, strongly associated to the geometry of the end shape of the pin, cannot be compared to other researcher's results.

(2) *Bio-medical applications*. One of the purposes of this study is to test new nanocomposites for improving the longevity of UHMWPE hip joint replacement. HDPE has a similar chemical structure as UHMWPE. Therefore, the study of HDPE/CNF nanocomposite

can be viewed as a preliminary investigation on UHMWPE/CNF nanocomposite. HDPE, having a lower viscosity in melt compared to UHMWPE, is much easier to process. The results in HDPE/CNF nanocomposites may have potential implications and contributions to the study of UHMWPE/CNF nanocomposites. Therefore, the future work may be developed into the field of UHMWPE/CNF nanocomposites or UHMWPE/HDPE/CNF nanocomposites. UHMWPE/HDPE/CNF nanocomposite may be desirable because the addition of HDPE can lower the viscosity of UHMWPE and improve the dispersion of CNF in the polymer matrix. To apply these new composites in artificial joints, the multidirectional sliding motion is necessary in the wear test, for example, the hip simulator and finite element analysis may be useful for the wear modeling. The biocompatibility problem of the nanocomposites in bio-medical applications is still in controversy, and needs to be explored further.

(3) *Wear of polymers under lubricated condition*. The traditional studies on wear were generally for the metal under unlubricated condition, for example, the famous Archard's wear law. Only a few studies experimentally characterized the wear rate of HDPE or UHMWPE materials under water or bovine serum lubricated condition because the wear test of UHMWPE under lubricated conditions produce very low wear rate and it takes as long as a month to test one sample. The wear of HDPE or UHMWPE under lubricated conditions is rarely simulated, possibly due to the complexity of the lubrication theory. The dissertation has proposed to use Reye's wear model to predict the wear of polymer under lubricated condition. However, the experimental data are limited in the UHMWPE and LDPE materials. More experimental clarifications are necessary for validating this model's application in other polymers or polymer composites. The wear of HDPE as a line contact problem was simulated in this work. In the future, the solutions for an area contact problem or, furthermore, ball-on-socket contact problem can be developed. In addition, to elongate the longevity of UHMWPE hip joint replacement, another direction is to apply more effective artificial lubricants to hip joints.

Therefore, the wear of UHMWPE under different combinations of bio-lubricants may be addressed in the future.

REFERENCES

[1] Szeri, A. Z., 1998, Fluid film lubrication: theory and desgin, Cambridge University Press, Cambridge, UK.

[2] Zoo, Y., An, J., Lim, D., and Lim, D., 2004, "Effect of carbon nanotube addition on tribological behavior of UHMWPE," Tribology Letters, 16(4), pp. 305-309.

[3] Bae, J., Kim, K., Hattori, M., Hasegawa, K., Yoshinari, M., Kawada, E., and Oda, Y., 2004, "Fatigue strengths of particulate filler composites reinforced with fibers," Dental Materials Journal, 23(2), pp. 166-174.

[4] Xiong, D., 2005, "Friction and wear properties of UHMWPE composites reinforced with carbon fiber," Materials Letters, 59(2-3), pp. 175-179.

[5] Wood, W., Maguire, R., and Zhong, W., 2011, "Improved wear and mechanical properties of UHMWPE-carbon nanofiber composites through an optimized paraffin-assisted melt-mixing process," Composites Part B-Engineering, 42(3), pp. 584-591.

[6] Liu, T., Wood, W., and Zhong, W., 2011, "Sensitivity of dielectric properties to wear process on carbon nanofiber/high-density polyethylene composites," Nanoscale Research Letters, pp.6.

[7] Amontons, G., 1699, De la resistance casusee dan les machines, Royal Society, Paris.

[8] Coulomb, C. A., 1785, "Theorie des machines simples," Mémoires de mathématique et de physique Académie royale des sciences, 10, pp. 161.

[9] Ramalho, A., and Miranda, J., 2006, "The relationship between wear and dissipated energy in sliding systems," Wear, 260(4-5), pp. 361-367.

[10] Rodkiewicz, C., and Wang, Y., 1994, "A dry wear model-based on energy consideration," Tribology International, 27(3), pp. 145-151.

[11] Zhang, S., 1998, "State-of-the-art of polymer tribology," Tribology International, 31(1-3), pp. 49-60.

[12] Archard, J., 1953, "Contact and rubbing of flat surfaces," Journal of Applied Physics, 24(8), pp. 981-988.

[13] Rhee, S., and Ludema, K., 1978, "Mechanisms of formation of polymeric transfer films," Wear, 46(1), pp. 231-240.

[14] Friedrich, K., Reinicke, R., and Zhang, Z., 2002, "Wear of polymer composites," Proceedings of the Institution of Mechanical Engineers Part J-Journal of Engineering Tribology, 216(J6), pp. 415-426.

[15] Briscoe, B., and Sinha, S., 2002, "Wear of polymers," Proceedings of the Institution of Mechanical Engineers Part J-Journal of Engineering Tribology, 216(J6), pp. 401-413.

[16] Baechler, C., DeVuono, M., and Pearce, J., 2013, "Distributed recycling of waste polymer into RepRap feedstock," Rapid Prototyping Journal, 19(2), pp. 118-125.

[17] https://www.plasticsintl.com/datasheets/LDPE.pdf.

[18] http://catalog.wshampshire.com/Asset/psg_uhmw_polyethylene.pdf.

[19] Edidin, A., and Kurtz, S., 2000, "Influence of mechanical behavior on the wear of 4 clinically relevant polymeric biomaterials in a hip simulator," Journal of Arthroplasty, 15(3), pp. 321-331.

[20] Suh, N., Mosleh, M., and Arinez, J., 1998, "Tribology of polyethylene homocomposites," Wear, 214(2), pp. 231-236.

[21] Sahebian, S., Zebarjad, S., Sajjadi, S., Sherafat, Z., and Lazzeri, A., 2007, "Effect of both uncoated and coated calcium carbonate on fracture toughness of HDPE/$CaCO_3$ nanocomposites," Journal of Applied Polymer Science, 104(6), pp. 3688-3694.

[22] Guermazi, N., Elleuch, K., Ayedi, H., Fridrici, V., and Kapsa, P., 2009, "Tribological behaviour of pipe coating in dry sliding contact with steel," Materials & Design, 30(8), pp. 3094-3104.

[23] Anderson, J., 1982, "High density and ultrahigh molecular weight polyethylene-their wear properties and bearing applications," Tribology International, 15(1), pp. 43-47.

[24] Kurtz, S. M., 2009, UHMWPE Biomaterials Handbook, Academic Press, Burlington, USA.

[25]http://www.made-in-china.com/China-Hdpe-Small-Gears.html.

[26] http://www.diytrade.com/china/ Plastic_bearing.html.

[27] http://www.hnaycg.cn.alibaba.com.

[28] Wood, W., 2012, "Processing, wear, and mechanical properteis of polyethylene composites prepared with pristine and organosilane-treated carbon nanofibers," Ph.D, Washington State University, Pullma.

[29] Akchurin, A., 2012, "Lubrication and wear at metal/HDPE contacts," Master, North Dakota State University, Fargo.

[30] Havelin, L., Fenstad, A., Salomonsson, R., Mehnert, F., Furnes, O., Overgaard, S., Pedersen, A., Herberts, P., Karrholm, J., and Garellick, G., 2009, "The Nordic Arthroplasty Register Association A unique collaboration between 3 national hip arthroplasty registries with 280,201 THRs," Acta Orthopaedica, 80(4), pp. 393-401.

[31] Ingham, E., and Fisher, J., 2000, "Biological reactions to wear debris in total joint replacement," Proceeding Institute of Mechanical Engineering, 214, pp. 21-36.

[32] Vermes, C., Roebuck, K., Chandrasekaran, R., Dobai, J., Jacobs, J., and Glant, T., 2000, "Particulate wear debris activates protein tyrosine kinases and nuclear factor kappa Beta, which down-regulates type I collagen synthesis in human osteoblasts," Journal of Bone and Mineral Research, 15(9), pp. 1756-1765.

[33] Wroblewski, B., Lynch, M., Atkinson, J., Dowson, D., and Isaac, G., 1987, "External wear of the polyethylene socket in cemented total hip arthroplasty," Journal of Bone and Joint Surgery-British Volume, 69(1), pp. 61-63.

[34] Isaac, G., Atkinson, J., Dowson, D., and Wroblewski, B., 1986, "The role of cement in long-term performance and premature failure of Charnley low friction arthroplasties," Engineering in Medicine, 15, pp. 19-22.

[35] Fouad, H., Elleithy, R., Al-Zahrani, S., and Ali, M., 2011, "Characterization and processing of High Density Polyethylene/carbon nano-composites," Materials & Design, 32(4), pp. 1974-1980.

[36] Fouad, H., and Elleithy, R., 2011, "High density polyethylene/graphite nano-composites for total hip joint replacements: Processing and in vitro characterization," Journal of the Mechanical Behavior of Biomedical Materials, 4(7), pp. 1376-1383.

[37] Johnson, B., Santare, M., Novotny, J., and Advani, S., 2009, "Wear behavior of Carbon Nanotube/High Density Polyethylene composites," Mechanics of Materials, 41(10), pp. 1108-1115.

[38] Sauer, W. L., and Anthony, M. E., 1997, "Predicting the clinical wear performance of orthopaedic bearing surfaces.," Proceedings of the Symposium on Alternative Bearing Surfaces in Total Joint Replacement, ASTM InternationalSan Digo, USA, pp. 2-6.

[39] Ajayan, P., Schadler, L., and Braun, P., 2003, Nanocomposite science and technology, Wiley, New York.

[40] Galetz, M., Blass, T., Ruckdaschel, H., Sandler, J., Altstadt, V., and Glatzel, U., 2007, "Carbon nanofibre-reinforced ultrahigh molecular weight polyethylene for tribological applications," Journal of Applied Polymer Science, 104(6), pp. 4173-4181.

[41] Wright, T., Astion, D., Bansal, M., Rimnac, C., Green, T., Insall, J., and Robinson, R., 1988, "Failure of carbon fiber-reinforced polyethylene total knee-replacement components-a report of 2 cases," Journal of Bone and Joint Surgery-American Volume, 70A(6), pp. 926-932.

[42] Wright, T., Rimac, C., Faris, P., and Bansal, M., 1988, "Analysis of surface Damage in retrieved carbon fiber-reinforced and plain polyethylene tibial components from posterior stabilized total knee replacements," Journal of Bone and Joint Surgery-American Volume, 70A(9), pp. 1312-1319.

[43] Ruan, S., Gao, P., Yang, X., and Yu, T., 2003, "Toughening high performance ultrahigh molecular weight polyethylene using multiwalled carbon nanotubes," Polymer, 44(19), pp. 5643-5654.

[44] Shah, D., Maiti, P., Jiang, D., Batt, C., and Giannelis, E., 2005, "Effect of nanoparticle mobility on toughness of polymer nanocomposites," Advanced Materials, 17(5), pp. 525.

[45] Chan, C., Wu, J., Li, J., and Cheung, Y., 2002, "Polypropylene/calcium carbonate nanocomposites," Polymer, 43(10), pp. 2981-2992.

[46] Dasari, A., Yu, Z., and Mai, Y., 2009, "Fundamental aspects and recent progress on wear/scratch damage in polymer nanocomposites," Materials Science & Engineering R-Reports, 63(2), pp. 31-80.

[47] Xiong, D., Lin, J., and Fan, D., 2006, "Wear properties of nano-Al2O3/UHMWPE composites irradiated by gamma ray against a CoCrMo alloy," Biomedical Materials, 1(3), pp. 175-179.

[48] Liu, S., and Xu, J., 2011, "Characterization and mechanical properties of high density polyethylene/silane montmorillonite nanocomposites," International Communications in Heat and Mass Transfer, 38(6), pp. 734-741.

[49] Xiong, L., Xiong, D., and Jin, J., 2009, "Study on Tribological Properties of Irradiated Crosslinking UHMWPE Nano-Composite," Journal of Bionic Engineering, 6(1), pp. 7-13.

[50] Xiong, L., Xiong, D., Yang, Y., and Jin, J., 2011, "Friction, wear, and tensile properties of vacuum hot pressing crosslinked UHMWPE/nano-HAP composites," Journal of Biomedical Materials Research Part B-Applied Biomaterials, 98B(1), pp. 127-138.

[51] Kanagaraj, S., Varanda, F., Zhil'tsova, T., Oliveira, M., and Simoes, J., 2007, "Mechanical properties of high density polyethylene/carbon nanotube composites," Composites Science and Technology, 67(15-16), pp. 3071-3077.

[52] Zhil'tsova, T., Oliveira, M., and Ferreira, J., 2009, "Relative influence of injection molding processing conditions on HDPE acetabular cups dimensional stability," Journal of Materials Processing Technology, 209(8), pp. 3894-3904.

[53] Colaco, R., and Vilar, R., 2003, "A model for the abrasive wear of metallic matrix particle-reinforced materials," Wear, 254(7-8), pp. 625-634.

[54] Wen, J., Yin, P., and Zhen, M., 2008, "Friction and wear properties of UHMWPE/nan-MMT composites under oilfield sewage condition," Materials Letters, 62, pp. 4161-4163.

[55] Strawhecker, K., and Manias, E., 2000, "Structure and properties of poly(vinyl alcohol)/Na+ montmorillonite nanocomposites," Chemistry of Materials, 12(10), pp. 2943-2949.

[56] William, G. E., Aldo, B. A., and Jinwen, Z., 2005, "Polymer nanocomposites: Synthetic and natural fillers-A review," Maderas Ciencia y tecnología, 7, pp. 159-178.

[57] Das, A., Stockelhuber, K., Jurk, R., Saphiannikova, M., Fritzsche, J., Lorenz, H., Kluppel, M., and Heinrich, G., 2008, "Modified and unmodified multiwalled carbon nanotubes in high performance solution-styrene-butadiene and butadiene rubber blends," Polymer, 49(24), pp. 5276-5283.

[58] Xue, Y., Wu, W., Jacobs, O., and Schadel, B., 2006, "Tribological behaviour of UHMWPE/HDPE blends reinforced with multi-wall carbon nanotubes," Polymer Testing, 25(2), pp. 221-229.

[59] Lakshminarayanan, P., Toghiani, H., and Pittman, C., 2004, "Nitric acid oxidation of vapor grown carbon nanofibers," Carbon, 42(12-13), pp. 2433-2442.

[60] Jimenez, G., and Jana, S., 2007, "Oxidized carbon nanofiber/polymer composites prepared by chaotic mixing," Carbon, 45(10), pp. 2079-2091.

[61] Lee, J., Kathi, J., Rhee, K., and Lee, J., 2010, "Wear Properties of 3-Aminopropyltriethoxysilane-Functionalized Carbon Nanotubes Reinforced Ultra High Molecular Weight Polyethylene Nanocomposites," Polymer Engineering and Science, 50(7), pp. 1433-1439.

[62] Sui, G., Zhong, W., Ren, X., Wang, X., and Yang, X., 2009, "Structure, mechanical properties and friction behavior of UHMWPE/HDPE/carbon nanofibers," Materials Chemistry and Physics, 115(1), pp. 404-412.

[63] Xiong, D., Lin, J., Fan, D., and Jin, Z., 2007, "Wear of nano-TiO2/UHMWPE composites radiated by gamma ray under physiological saline water lubrication," Journal of Materials Science-Materials in Medicine, 18(11), pp. 2131-2135.

[64] Rabinowicz, E., 1995, Friction and Wear of Materials, John Wiley & Sons Inc., New York,USA.

[65] ASME, 1987, "Annual Book of Standards," Standard Terminology Relating to Wear and Erosion.

[66] Axén, N., Jacobson, S., and Hogmark, S., 1994, "Influence of hardness of the counterbody in three-body abrasive wear — an overlooked hardness effect," Tribology International, 27, pp. 233–241.

[67] Chairman, C. A., Babu, S. P. K., DuraiSelvam, M., and Balasubramanian, K. R., 2011, "Investigation on two-body abrasive wear behavior of titanium carbide filled glass fabric-epoxy composites- a Box-Behnken approach C.," International Journal of Engineering, Science and Technology, 3, pp. 119-129.

[100] Briscoe, B., Stuart, B., Sebastian, S., and Tweedale, P., 1993, "The failure of poly(ether ether ketone) in high-speed contacts," Wear, 162, pp. 407-417.

[69] Wood, W., Li, B., and Zhong, W., 2010, "Influence of phase morphology on the sliding wear of polyethylene blends filled with carbon nanofibers," Polymer Engineering and Science, 50(3), pp. 613-623.

[70] Pesetskii, S. S., Bogdanovich, S. P., and Myshkin, N. K., 2007, "Tribological behavior of nanocomposites produced by the dispersion of nanofillers in polymer Melts," Journal of Friction and Wear, 28, pp. 457-475.

[71] Ge, S., Wang, S., and Huang, X., 2009, "Increasing the wear resistance of UHMWPE acetabular cups by adding natural biocompatible particles," Wear, 267(5-8), pp. 770-776.

[72] Blunn, G., Walker, P., Joshi, A., and Hardinge, K., 1991, "The dominance of cyclic sliding in producing wear in total knee replacements," Clinical Orthopaedics and Related Research(273), pp. 253-260.

[73] Tulp, N., 1992, "Polyethylene delamination in the PCA total knee-material analysis in 2 failed cases," Acta Orthopaedica Scandinavica, 63(3), pp. 263-266.

[74] Suh, N., 1977, "Overview of delamination theory of wear," Wear, 44(1), pp. 1-16.

[75] Archard, J., and Hirsth, W., 1956, "The wear of metals under unlubricated conditions," Proceedings of the Royal Society of London Series A-Mathematical and Physical Sciences, 236(1206), pp. 397.

[76] K.C., L., 1996, Friction, Wear, Lubrication: a textbook in Tribology, Ann Arbor: CRC Press, Inc, Boca Raton.

[77] Khruschov, M. M., 1957, "Resistance of metal to wear by abrsion as related to hardness," Proceddings of the conference on lubrication and wear, pp. 655-659.

[78] Lancaste, JK, 1969, "Abrasive wear of polymers," Wear, 14(4), pp. 223

[79] Lu, H., Wang, B., Ma, J., Huang, G., and Viswanathan, H., 2003, "Measurement of creep compliance of solid polymers by nanoindentation," Mechanics of Time-dependent materials, 7, pp. 189-207.

[80] Zeng, H., 2013, Polymer, adhension, friction, and lubrication.

[81] Lancaster, J. K., 1973, "Basic mechanisms of friction and wear of polymers," Plastic Polymer, 41, pp. 297–306.

[82] Briscoe, B., 1981, "Wear of polymers-an essay on fundamental aspects," Tribology International, 14(4), pp. 231-243.

[83] Reye, T., 1860, "Zur theorie der zapfenreibung," Der Civilingenieur, 4, pp. 235–255.

[84] M. Jahangiri M. Hashempour H. Razavizadeh, H. R. R., 2011, "A new method to investigate the sliding wear behaviour of materials based on energy dissipation: W–25 wt%Cu composite," Wear, 274-275, pp. 175-182.

[85] Tan, E., and Lim, C., 2006, "Mechanical characterization of nanofibers - A review," Composites Science and Technology, 66(9), pp. 1102-1111.

[86] Wood, W., Kumar, S., and Zhong, W., 2010, "Synthesis of Organosilane-Modified Carbon Nanofibers and Influence of Silane Coating Thickness on the Performance of Polyethylene Nanocomposites," Macromolecular Materials and Engineering, 295(12), pp. 1125-1135.

[87] Moore, A., Cummings, A., Jensen, J., Shi, L., and Koo, J., 2009, "Thermal conductivity measurements of nylon 11-carbon nanofiber nanocomposites," Journal of Heat Transfer-Transactions of the ASME, 131(9).

[88] Ma, P., Kim, J., and Tang, B., 2007, "Effects of silane functionalization on the properties of carbon nanotube/epoxy nanocomposites," Composites Science and Technology, 67(14), pp. 2965-2972.

[89] Tan, J., Chao, Y., Van Zee, J., Li, X., Wang, X., and Yang, M., 2008, "Assessment of mechanical properties of fluoroelastomer and EPDM in a simulated PEM fuel cell environment

by micro indentation test," Materials Science and Engineering a-Structural Materials Properties Microstructure and Processing, 496(1-2), pp. 464-470.

[90] Madhukar, M., and Drzal, L., 1992, "Fiber-matrix adhesion and its effect on composite mechanical properties.3. Longitudinal (0-Degrees) compressive properties of graphite epoxy composites," Journal of Composite Materials, 26(3), pp. 310-333.

[91] Drzal, L., and Madhukar, M., 1993, "Fiber matrix adhesion and its relationship to composite mechanical properties," Journal of Materials Science, 28(3), pp. 569-610.

[92] Liu, T., 2011, "Dlelectric sensityivity to wear and thermal processes on carbon nanofiber/high density polyethylene composites," Master of Science, Washington State University, Pullma.

[93] Zhou, W., 2011, "Thermal and dielectric properties of the AlN particles reinforced linear low-density polyethylene composites," Thermochimica Acta, 512(1-2), pp. 183-188.

[94] Firkowska, I., Boden, A., Vogt, A., and Reich, S., 2011, "Effect of carbon nanotube surface modification on thermal properties of copper-CNT composites," Journal of Materials Chemistry, 21(43), pp. 17541-17546.

[95] Nan, C., Liu, G., Lin, Y., and Li, M., 2004, "Interface effect on thermal conductivity of carbon nanotube composites," Applied Physics Letters, 85(16), pp. 3549-3551.

[96] Singh, I., Tanaka, M., and Endo, M., 2007, "Effect of interface on the thermal conductivity of carbon nanotube composites," International Journal of Thermal Sciences, 46(9), pp. 842-847.

[97] Davis, L., and Artz, B., 1995, "Thermal conductivity of metal matrix composites," Journal of Applied Physics, 77(10), pp. 4954-4960.

[98] He, Y., Moreira, B., Overson, A., Nakamura, S., Bider, C., and Briscoe, J., 2000, "Thermal characterization of an epoxy-based underfill material for flip chip packaging," Thermochimica Acta, 357, pp. 1-8.

[99] Gharagozloo-hubmann, k., Boden, A., Czempiel, G. J. F., Firkowska, L., and Reich, S., 2013, "Filler geometry and interface resistance of carbon nnofibers: key parameters in thermally conductive polymer nanocompoistes.," Applied Physical Letter, 102, p. 213103.

[100] Macedo, F., and Ferreira, J., 2003, "Thermal contact resistance evaluation in polymer-based carbon fiber composites," Review of Scientific Instruments, 74(1), pp. 828-830.

[101] Cayer-Barrioz, J., Mazuyer, D., Tonck, A., Kapsa, P., and Chateauminois, A., 2006, "Nanoscratch and friction: An innovative approach to understand the tribological behaviour of poly(amide) fibres," Tribology International, 39(2), pp. 62-69.

[102] Pettarin, V., Churruca, M., Felhos, D., Karger-Kocsis, J., and Frontini, P., 2010, "Changes in tribological performance of high molecular weight high density polyethylene induced by the addition of molybdenum disulphide particles," Wear, 269(1-2), pp. 31-45.

[103] Kennedy, F., Van Citters, D., Wongseedakaew, K., and Mongkolwongrojn, M., 2007, "Lubrication and wear of artificial knee joint materials in a rolling/sliding tribotester," Journal of Tribology-Transactions of the ASME, 129(2), pp. 326-335.

[104] Bhushan, B., 2001, Modern tribology handbook, volume 1, CRC press LLC, USA.

[105] Lavrakas, V., 1957, "Textbook errors: Guest column. XII: The lubricating properties of graphite," Journal of Chemical Education, 34, p. 240.

[106] Ho, S., Carpick, R., Boland, T., and LaBerge, M., 2002, "Nanotribology of CoCr-UHMWPE TJR prosthesis using atomic force microscopy," Wear, 253(11-12), pp. 1145-1155.

[107] Chen, Y., and Qiao, P., 2011, "Crack growth resistance of hybrid fiber-reinforced cement matrix composites," Journal of Aerospace Engineering, 24(2), pp. 154-161.

[108] Zhang, X., Pei, X., and Wang, Q., 2009, "Friction and wear studies of polyimide composites filled with short carbon fibers and graphite and micro SiO2," Materials & Design, 30(10), pp. 4414-4420.

[109] Wang, Y., Cheng, R., Liang, L., and Wang, Y., 2005, "Study on the preparation and characterization of ultra-high molecular weight polyethylene-carbon nanotubes composite fiber," Composites Science and Technology, 65(5), pp. 793-797.

[110] Wang, A., Sun, D., Stark, C., and Dumbleton, J., 1995, "Wear mechanisms of UHMWPE in total joint replacements," Wear, 181, pp. 241-249.

[111] Barbour, P., Stone, M., and Fisher, J., 1999, "A study of the wear resistance of three types of clinically applied UHMWPE for total replacement hip prostheses," Biomaterials, 20(22), pp. 2101-2106.

[112] Brown, S., and Clarke, I., 2006, "A review of lubrication conditions for wear simulation in artificial hip replacements," Tribology Transactions, 49(1), pp. 72-78.

[113] Kanagaraj, S., Mathew, M. T., Fonseca, A., Oliveira, M. S. A., Simoes, J. A. O., and Rocha, L. A., 2010, "Tribological characterisation of carbon nanotubes/ultrahigh molecular weight polyethylene composites: the effect of sliding distance," International Journal of Surface Science and Engineering, 4(4-6), pp. 305-321.

[114] ASTM, 2006, " Standard Test Method for Wear Testing of Polymeric Materials for Use in Total Joint Prostheses."

[115] Liao, Y., Benya, P., and McKellop, H., 1999, "Effect of protein lubrication on the wear properties of materials for prosthetic joints," Journal of Biomedical Materials Research, 48(4), pp. 465-473.

[116] Abdel-Aal, H., 2003, "On the interdependence between kinetics of friction-released thermal energy and the transition in wear mechanisms during sliding of metallic pairs," Wear, 254(9), pp. 884-900.

[117] Colaco, R., Gispert, M., Serro, A., and Saramago, B., 2007, "An energy-based model for the wear of UHMWPE," Tribology Letters, 26(2), pp. 119-124.

[118] D.Bryant, M., 2009, "Entropy and dissipative processes of friction and wear," FME transactions, 37, pp. 55-60.

[119] Huq, M., and Celis, J., 2002, "Expressing wear rate in sliding contacts based on dissipated energy," Wear, 252(5-6), pp. 375-383.

[120] Huq, M., and Celis, J., 1997, "Reproducibility of friction and wear results in ball-on-disc unidirectional sliding tests of TiN-alumina pairings," Wear, 212(2), pp. 151-159.

[121] Mohrbacher, H., Celis, J., and Roos, J., 1995, "Laboratory testing of displacement and load-induced fretting," Tribology International, 28(5), pp. 269-278.

[122] Jahangiria, M., Hashempourb, M., Razavizadehb, H., and Rezaieb, H. R., 2012, "Application and conceptual explanation of an energy-based approach for the modelling and prediction of sliding wear," wear, 274-275, pp. 168-174.

[123] Shakhvorostov, D., Pohlmann, K., and Scherge, M., 2004, "An energetic approach to friction, wear and temperature," Wear, 257(1-2), pp. 124-130.

[124] Li, X., Tabil, L., Oguocha, I., and Panigrahi, S., 2008, "Thermal diffusivity, thermal conductivity, and specific heat of flax fiber-HDPE biocomposites at processing temperatures," Composites Science and Technology, 68(7-8), pp. 1753-1758.

[125] Lafdi, K., 2003, "Carbon nanofibers as a Nano-reinforcement for polymeric nanocomposites," 48th International SAMPE Symposium ProceedingsLong Beach, USA.

[126] Charnley, J., 1960, "Anchorage of the femoral head prosthesis to the shaft of the femur," Journal of Bone and Joint Surgery-British Volume, 42(1), pp. 28-30.

[127] Wang, A., 2001, "A unified theory of wear for ultra-high molecular weight polyethylene in multi-directional sliding," Wear, 248(1-2), pp. 38-47.

[128] Bevill, S., Bevill, G., Penmetsa, J., Petrella, A., and Rullkoetter, P., 2005, "Finite element simulation of early creep and wear in total hip arthroplasty," Journal of Biomechanics, 38(12), pp. 2365-2374.

[129] Van Citters, D., Kennedy, F., and Collier, J., 2007, "Rolling sliding wear of UHMWPE for knee bearing applications," Wear, 263, pp. 1087-1094.

[130] Timoshenko, S., and Goodier, J. N., 1951, Theory of Elasticity, McGraw-Hill Book Company, Inc., New York.

[131] Wen, S., 1992, Elastohydrodynamic Lubrication, Tsinghua University press, Beijing.

[132] Abramowitz, M., and Stegun, I. A., 1972, Handbook of Mathematical Functions with Formulas, Graphs, and Mathematical Tables, Dover Publications, New York.

[133] Hertz, H. R., 1895, Ueber die Beruehrung elastischer Koerper (On Contact Between. Elastic Bodies), Gesammelte Werke, Leipzig, Germany.

APPENDIX A. INTEGRATION

In Chapter 5, the integration of the integral term *D* in Equation 5.14 needs the following mathematic treatments:

$$D = \int_0^{2\pi} \frac{1}{\sqrt{(x - Rcos\varphi)^2 + (y - Rsin\varphi)^2 + z^2}} d\varphi$$

$$= \int_0^{2\pi} \frac{1}{\sqrt{x^2 + y^2 + z^2 + R^2 - 2R(xcos\varphi + ysin\varphi)}} d\varphi$$

$$= \int_0^{2\pi} \frac{1}{\sqrt{x^2 + y^2 + z^2 + R^2 - 2R\sqrt{x^2 + y^2}\cos(\varphi - \alpha)}} d\varphi \qquad tan\alpha = \frac{y}{x}$$

$$= \int_0^{2\pi} \frac{1}{\sqrt{k_1 - k_2 cos(\varphi - \alpha)}} d\varphi$$

$$= \int_{-\alpha}^{2\pi-\alpha} \frac{1}{\sqrt{k_1 - k_2 cos\emptyset}} d\emptyset \qquad \varphi - \alpha = \emptyset$$

$$= \int_0^{2\pi} \frac{1}{\sqrt{k_1 - k_2 cos\emptyset}} d\emptyset \qquad \text{(D.1)}$$

where $k_1 = x^2 + y^2 + z^2 + R^2 \geq 0$; $k_2 = 2R\sqrt{x^2 + y^2} \geq 0$.

We know that when $f \geq 0$, $\frac{1}{f} + f \geq 2$; let $f = \frac{\sqrt{x^2+y^2}}{R}$

$$\frac{\sqrt{x^2 + y^2}}{R} + \frac{R}{\sqrt{x^2 + y^2}} \geq 2$$

$$R\sqrt{x^2 + y^2} \cdot \left(\frac{\sqrt{x^2 + y^2}}{R} + \frac{R}{\sqrt{x^2 + y^2}}\right) \geq 2R\sqrt{x^2 + y^2}$$

$$x^2 + y^2 + z^2 + R^2 \geq 2R\sqrt{x^2 + y^2} \qquad \text{(D.2)}$$

Therefore, $k_1 \geq k_2$ and $k_1 - k_2 cos\emptyset \geq 0$

$$D = \int_0^{2\pi} \frac{1}{\sqrt{k_1 - k_2 cos\emptyset}} d\emptyset \tag{D.3}$$

$$= \frac{1}{\sqrt{2k_2}} \int_0^{2\pi} \frac{1}{\sqrt{\frac{k_1 - k_2}{2k_2} + sin^2 \frac{\emptyset}{2}}} d\emptyset \qquad cos\emptyset = 1 - 2sin^2 \frac{\emptyset}{2}$$

$$= \frac{2}{\sqrt{2k_2}} \int_0^{\pi} \frac{1}{\sqrt{\frac{k_1 - k_2}{2k_2} + sin^2\theta}} d\theta \qquad \theta = \frac{\emptyset}{2}$$

$$= \frac{2}{\sqrt{2k_2}} \int_0^{\pi} \frac{cos\theta}{cos\theta \sqrt{\frac{k_1 - k_2}{2k_2} + sin^2\theta}} d\theta$$

$$= \frac{2}{\sqrt{2k_2}} \int_0^{\pi} \frac{d(sin\theta)}{\left(\pm\sqrt{1 - sin^2\theta}\right) \sqrt{\frac{k_1 - k_2}{2k_2} + sin^2\theta}}$$

$$= \frac{2}{\sqrt{2k_2}} \left[\int_0^{\frac{\pi}{2}} \frac{d(sin\theta)}{\left(\sqrt{1 - sin^2\theta}\right) \sqrt{\frac{k_1 - k_2}{2k_2} + sin^2\theta}} + \int_{-\frac{\pi}{2}}^{\pi} \frac{d(sin\theta)}{\left(-\sqrt{1 - sin^2\theta}\right) \sqrt{\frac{k_1 - k_2}{2k_2} + sin^2\theta}} \right]$$

$$= \frac{2}{\sqrt{2k_2}} \left[\int_0^1 \frac{dt}{\left(\sqrt{1 - t^2}\right) \sqrt{\frac{k_1 - k_2}{2k_2} + t^2}} - \int_1^0 \frac{dt}{\left(\sqrt{1 - t^2}\right) \sqrt{\frac{k_1 - k_2}{2k_2} + t^2}} \right] \qquad sin\theta = t$$

$$= \frac{4}{\sqrt{2k_2}} \int_0^1 \frac{dt}{\left(\sqrt{1 - t^2}\right) \sqrt{\frac{k_1 - k_2}{2k_2} + t^2}}$$

$$= \frac{4}{\sqrt{2k_2}} \int_0^1 \frac{dt}{\sqrt{(t^2 + a^2)(b^2 - t^2)}} \qquad a = \sqrt{\frac{k_1 - k_2}{2k_2}};\ b = 1$$

$$= \frac{4}{\sqrt{2k_2}} \cdot \frac{1}{\sqrt{a^2+b^2}} \cdot \sqrt{a^2+b^2} \cdot \int_0^1 \frac{dt}{\sqrt{(t^2+a^2)(b^2-t^2)}}$$

$$= \frac{4}{\sqrt{2k_2}} \cdot \frac{1}{\sqrt{a^2+b^2}} \cdot F(\frac{\pi}{2}|m) \qquad m = \frac{b^2}{a^2+b^2}$$

$$= \frac{4}{\sqrt{k_1+k_2}} F(\frac{\pi}{2}|m) \qquad m = \frac{2k_2}{k_1+k_2}$$

Because $k_1 \geq k_2 \geq 0,\ 0 \leq m \leq 1$.

It needs to be noted that $\int_0^1 \frac{dt}{\sqrt{(t^2+a^2)(b^2-t^2)}}$ can be transferred into a complete integral of the first kind as $F(\frac{\pi}{2}|m)$, where $m = \frac{b^2}{a^2+b^2}$. It has been proven that $0 \leq m \leq 1$ which satisfies the requirement of the complete integrals of the first kind. The detailed transformation for this type of integration is referred to in Equation 17.4.51 in the Ref. [132]. The complete integrals of the first kind, $F(\frac{\pi}{2}|m)$, can be obtained either with Matlab function of ellipke(m) or with Table 17.5 in the Ref. [132].

For example, if $x \in [0,10]$, y=0, z=0, and R=5, the integral term of D can be dimensionless treated as following:

$$D = \int_0^{2\pi} \frac{1}{\sqrt{(x-Rcos\varphi)^2+(y-Rsin\varphi)^2+z^2}} d\varphi$$

$$\frac{D}{R} = \int_0^{2\pi} \frac{1}{\sqrt{(\frac{x}{R})^2 - 2\frac{x}{R}cos\varphi + 1}} d\varphi \qquad \tilde{X} = \frac{x}{R}$$

$$\widetilde{D} = \frac{D}{R}$$

$$\widetilde{D} = \int_0^{2\pi} \frac{1}{\sqrt{\tilde{X}^2 - 2\tilde{X}cos\varphi + 1}} d\varphi \qquad \text{(D.5)}$$

$$\widetilde{D} = \frac{4}{\sqrt{\tilde{X}^2+2\tilde{X}+1}} = \frac{4}{\tilde{X}+1} F(\frac{\pi}{2}|\frac{4\tilde{X}}{\tilde{X}^2+2\tilde{X}+1}) \qquad \text{(D.6)}$$

The relationship between $\widetilde{D}$ and $\tilde{X}$ can be plotted as shown in Figure A.1. It showed that the integral term D goes towards infinity when X is close to R. Value of D obtains the maximum when X=0. When $X > R$, the integral D decreases with the increase in R.

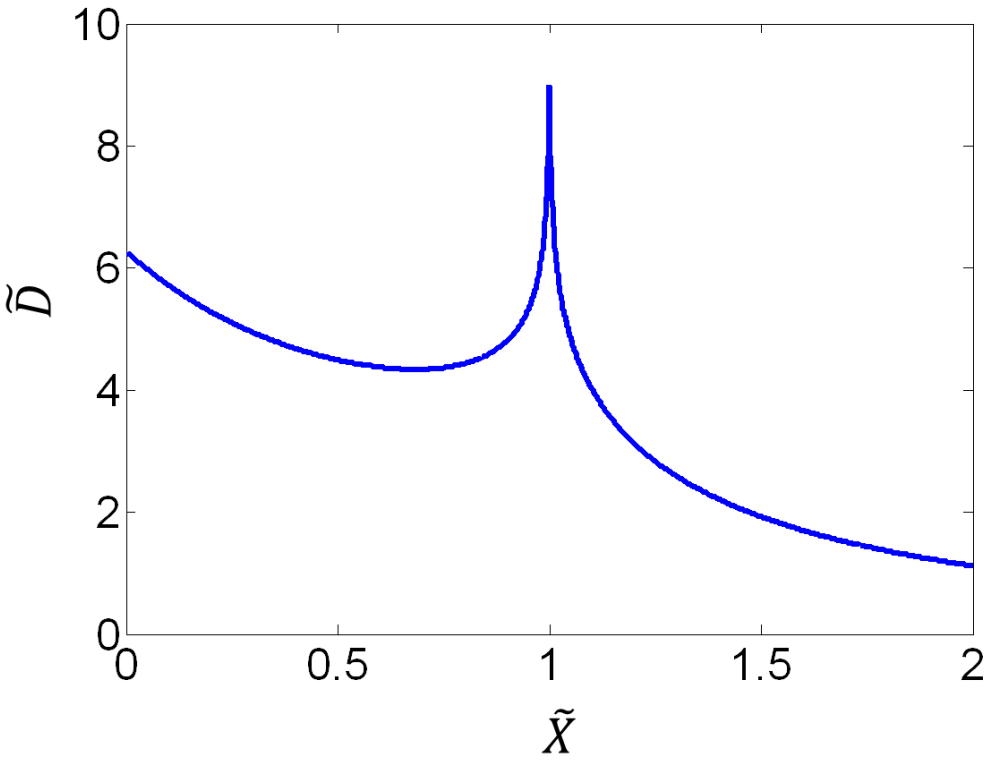

Figure A.1: The relationship between $\widetilde{D}$ and $\tilde{X}$.

APPENDIX B. HERTZIAN CONTACT THEORY

In Chapter 6, the dimensionless treatment for the parameters in the Reylond's equations used the Hertzian parameters, which are given in the following Hertzian Theory[133].

In the Hertzian contact theory, the line contact problem under a normal load, N, between two cylinders with parallel axes is reduced into a 2D problem shown in Figure AB-1. The two circles in Figure B-1 with the radius of R_1 and R_2 represent the cross-sections of the two contact cylinders, respectively. The normal load, W, in Figure B.1, is the normal load per unit of length:

$$W = \frac{N}{L} \tag{B.1}$$

where L is the length of two cylinders.

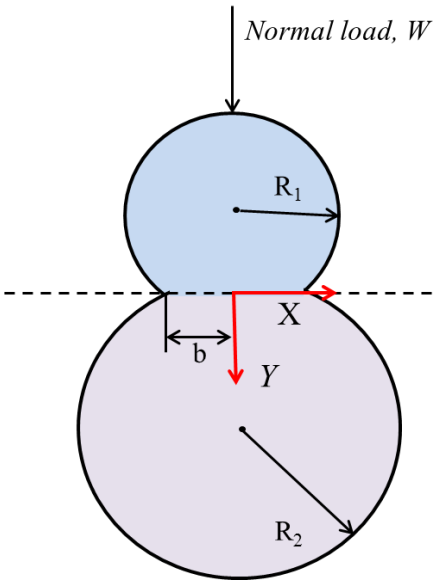

Figure B.1: 2D schematic of the line contact problem between two cylinders with parallel axes.

The half Hertzian width (b) of the contact line between the two circles in Figure B.1 is calculated as:

$$b = \sqrt{\frac{8}{\pi}\frac{WR}{E'}} \tag{B.2}$$

where E' and R are the reduced elastic modulus and reduced radius, respectively. The value of the reduced elastic modulus is defined by:

$$\frac{1}{E'} = \frac{1}{2}\left(\frac{1-{v_1}^2}{E_1} + \frac{1-{v_2}^2}{E_2}\right) \tag{B.3}$$

with E_1 and E_2 as the elastic modulus, and v_1 and v_2 as Poission's ratio of the two cylinders, respectively. The reduced radius is given by:

$$\frac{1}{R} = \left(\frac{1}{R_1} + \frac{1}{R_2}\right) \tag{B.4}$$

with R_1 and R_2 as the radius of the two cylinders, respectively. It should note that if the bottom cylinder is a plane, the radius of R_2 can be regarded as an infinity. The reduced radius, R, therefore equals R_1.

The maximum Hertzain pressure is at the center of the contact line and can be obtained by:

$$p_H = \frac{2W}{\pi b} = \sqrt{\frac{WE'}{2\pi R}} = \frac{E'b}{4R} \tag{B.5}$$

The distribution of contact pressure in the contact line as a function of distance from the center of the circle is:

$$p = p_H\sqrt{1-\frac{x^2}{b^2}} \tag{B.6}$$

APPENDIX C. PROGRAMING

The main Matlab codes for solving the Reylond's equation and wear simulation under lubricated conditions are presented here.

Function 1: main.m

```
N=100;                              %Number of Nodes
P0=linspace(0,0,N+1);               %Initial pressure
P=linspace(0,0,N+1);                %Pressure
DP=linspace(0,0,N+1);               %dot_P
XP=linspace(0,0,N+1);               %X at nodes
H=linspace(0,0,N+1);                %film thickness
F=linspace(0,0,N+1);                %F_matrix
B=linspace(0,0,N+1);                %B_matrix
DF=linspace(0,0,N+1);               %dot_F
DL=linspace(0,0,N+1);               %Middle matrix to get CIJ
MIDU=linspace(0,0,N+1);             %DENSITY
NIANDU=linspace(0,0,N+1);           %VISCOSITY
CIJ=zeros(N+1,N+1);                 %C_matrix
KK=zeros(N,N);                      %Finial Kmatrix N*N
KK1=zeros(N+1,N+1);                 %Finial K1_matrix
KK2=zeros(N+1,N+1);                 %Finial K2_matrix
LNODS=zeros(N+1,2);                 %Middle matrix

initialization;          %initialization
for i=1:N+1
    if(XP(i)^2<=1)
        P0(i)=sqrt(1-XP(i)^2);
    end
end
P=P0;
DH0=1; %%erro
MAXIT=100; %%maxmium iteration
ITER=0;
while (abs(DH0)>0.01&&ITER<=MAXIT)
    ITER=ITER+1;
    IT=0;
    EP=1;
    while (EP>0.01&&IT<=MAXIT)
        IT=IT+1;
        film_thick;              %film thickness
        matrix_final;            %Jacob matrix
       DP(2:N+1)=KK\DF(2:N+1)'; %newton method
       DH0=DP(N+1);
       DP(N+1)=0;
       sum2=0;
       sum3=0;
```

```
        for i=1:N
            sum2=sum2+abs(DP(i));
            sum3=sum3+P(i);
        end
        EP=sum2/sum3;
        P=P+0.4*DP;
    end
     H0=H0+0.3*DH0;
End

Plot (XP,H,XP,P)
```

Function 2: initialization.m

```
NIANDU0=0.00496;                    % initial viscosity
R=0.0025;                           % radius of cylinder
E0=1.27*10^9;                       % Reduced Elastic, where
HDPE E=0.526*10^9 Pa, Poisson ratio=0.35,E0=2*1.05*10^9/(1-
0.35^2);
uuu=10*pi*10^(-3)/2;                % Actual speed
U=uuu*NIANDU0/E0/R;                 % dimensionless speed

Normal=50;                          % Normal load, N
w=Normal/(2*R);                     % Normal load in unit length
W=w/E0/R;                          % Dimensionless load

A0=5.9*10^(-9);                    % Pressure-viscosity
coefficient
G=A0*E0;                           % Dimensionless Material
properties

B=(sqrt(8.0*W/pi))*R;              % Radius of contact line, b
bbb=(sqrt(8.0*W/pi))*R;
PH=E0*B/(4*R);                     % Maximum pressure, pH
T=3.0*(pi^2)*U/(4*W^2);            % Right constant in Reylond's
equation, A1

HM_INTIAL=0.24*10^(-6);
hmj=0;
HM=R*((2*HM_INTIAL-hmj)/2)*B^2;     %Dimensionless asperity
height

LAMDA=2*pi/(0.5*10^(-2)/B);         %Dimensionless wave length



H0=0;                               % initial film thickness
XP(1)=-2.5;                         % First Node's X
XP(N+1)=2.5;                        % Last Node's X
D=(XP(N+1)-XP(1))/N;                % Dot_X
```

```
for i= 2:N
    XP(i)=XP(1)+(i-1)*D;            % X at i node
end
```

Function 3: film_thick.m

```
for i=1:N+1
    H(i)=H0+XP(i)^2/2-HM*sin(LAMDA*XP(i));
%a part of film thickness without the elastic deformation%
    DH=0;
    for j=2:N+1
        DL(j-1)=XP(j)-XP(j-1);
        if(i==j||i==j-1)
           aa=XP(i);
           bb=XP(j)+0.1*DL(j-1);
           if aa==bb
              CIJ(i,j)=(-0.5/3.14)*DL(j-1)*log(0.01);
           else
             CIJ(i,j)=(-0.5/3.14)*DL(j-1)*log((aa-bb)^2);
           end
        else
           CIJ(i,j)=(-0.5/3.14)*DL(j-1)*log((XP(i)-XP(j))^2);
        end
        DH=DH+CIJ(i,j)*P(j);
% elastic deformation%
   end
    H(i)=H(i)+DH;
% film thickness at each node %
end
```

Function 4: matrix_element.m

```
A=zeros(2,2);      %K1
           AL=zeros(2,N+1);  %K2
           BB=linspace(0,0,2);
           FF=linspace(0,0,2);
           E=linspace(0,0,N+1);
           for i=NEL-1:NEL
               E(i)=MIDU(i)*H(i)^3/NIANDU(i);
           end
           for i=1:N                %K2
               AL(1,i)=T*(MIDU(NEL-1)*CIJ(NEL-
1,i)+MIDU(NEL)*CIJ(NEL,i))/2;       %            %
               AL(2,i)=-AL(1,i);
           end
           A(1,1)=(E(NEL-1)+E(NEL))/(2.0*D);         %K1
           A(1,2)=-A(1,1);
           A(2,1)=A(1,2);
           A(2,2)=A(1,1);
```

```
            FF(1)=-T*(MIDU(NEL-
1)+MIDU(NEL))/2.0*(H0+(XP(NEL)^3-XP(NEL-1)^3)/(6*D));
            FF(2)=-FF(1);
            for i=NEL-1:NEL
                if(i==1||i==N+1)
                    DP(i)=0;
                else
                    DP(i)=(P(i+1)-P(i-1))/(XP(i+1)-XP(i-1));
                end
            end
BB(1)=-3.0*(MIDU(NEL-1)*H(NEL-1)^2/NIANDU(NEL-1)*DP(NEL-
1)+MIDU(NEL);
H(NEL)^2/NIANDU(NEL)*DP(NEL))/2+T*(MIDU(NEL-1)+MIDU(NEL))/2.0;
            BB(2)=-BB(1);
```

Function 5: matrix finial.m

```
NNODZ=2;
       for i=1:N+1
MIDU(i)=1.0+((0.6e-9)*P(i)*PH)/(1.0+(1.7e-9)*P(i)*PH);
%density%
NIANDU(i)=exp(A0*P(i)*PH);
%viscosity%
       end
       KK1=zeros(N+1,N+1);
       KK2=zeros(N+1,N+1);
       F=zeros(1,N+1);
       B=zeros(1,N+1);
       for NEL=2:N+1
           matrix_element;
%get the elements in each matrix%
           for i=1:NNODZ
               LNODS(NEL,i)=NEL+i-2;
           end
           for i=1:NNODZ
               ISTRST=LNODS(NEL,i);
               IELEMT=i;
               for j=1:NNODZ
                   JSTRST=LNODS(NEL,j);
                   JELEMT=j;
KK1(ISTRST,JSTRST)=KK1(ISTRST,JSTRST)+A(IELEMT,JELEMT);
               end
               F(ISTRST)=F(ISTRST)+FF(IELEMT);
               B(ISTRST)=B(ISTRST)+BB(IELEMT);
               for j=1:N
                   KK2(ISTRST,j)=KK2(ISTRST,j)+AL(IELEMT,j);
               end
           end
       end
       sum1=0;
```

```
        for i=2:N
            sum=0;
            for j=2:N
                KK(i-1,j-1)=KK1(i,j)+KK2(i,j);
                sum=sum+KK(i-1,j-1)*P(j);
            end
            DF(i)=F(i)-sum;
            KK(i-1,N)=B(i);
             KK(N,i-1)=(XP(i+1)-XP(i-1))/2;
            sum1=sum1+P(i)*(XP(i+1)-XP(i));
        end
        DF(N+1)=pi/2-sum1;
KK(N,N)=0;
```

Function 6. wear.m

```
main;
XP_ND=XP.*bbb;
P_ND=P.*PH;
for i=2:101
    det_XP_ND(i)=XP_ND(i)-XP_ND(i-1);
end

det_hh=det_XP_ND.*P_ND;

for i=2:101
    det_hh(1,i)=det_hh(1,i-1)+det_hh(1,i);
end


DET_HH=det_hh(1,101);
KR=4.2*10^(-15);
COF=0.039;
DET_H=3600*KR*COF*DET_HH;
DET_V=DET_H*2*pi*0.005*2*0.0025*(DET_HTOTAL/(2*HM_INTIAL))^2;
```

APPENDIX D. LIST OF PUBLICATIONS

Peer-reviewed Journal Publications:

1. **S.Xu**, I.Tarnavchyk, A.Voronov, X.W.Tangpong, I.S.Akhatov, "Wear and friction of LDPE and UHMWPE under lubricated conditions," (In preparation)
2. **S. Xu**, A. Akchurin, T. Liu, W. Wood, X.W. Tangpong, I.S. Akhatov and W.H. Zhong, " Thermal and Wear Analysis of HDPE/CNF Nanocomposites in Dry Sliding Contact with A Steel Ball," (In preparation)
3. **S. Xu**, A. Akchurin, T. Liu, W. Wood, X.W. Tangpong, I.S. Akhatov and W.H. Zhong, 2014, "Mechanical Properties, Tribological Behavior, and Biocompatibility of high-density polyethylene/carbon nanofibers nanocomposites", ***Journal of composite materials***, DOI: 10.1177/0021998314535959
4. **S. Xu**, A. Akchurin, T. Liu, W. Wood, X.W. Tangpong, I.S. Akhatov and W.H. Zhong, 2014, "Thermal Properties of Carbon Nano-fiber Reinforced High-density Polyethylene Nanocomposites," ***Journal of composite materials,*** DOI: 10.1177/0021998314525980
5. **S. Xu**, A. Akchurin, T. Liu, W. Wood, X.W. Tangpong, I.S. Akhatov, and W-H. Zhong, 2013, "Wear of Carbon Nanofiber Reinforced HDPE Nanocomposites under Dry Sliding Condition," ***ASME Journal of Nanotechnology in Engineering and Medicine,*** **3(4)** : article ID 041003
6. **S. Xu**, and X.W. Tangpong, 2013, "Review: Tribological Behavior of Polyethylene-Based Nanocomposites," ***Journal of Materials Science***, **48(2)**: 578-597. DOI: 10.1007/s10853-012-6844-x
7. **S. Xu**, A. Akchurin, T. Liu, W. Wood, X.W. Tangpong, I.S. Akhatov, and W-H. Zhong, 2012, "Wear and Friction of Carbon Nanofiber-Reinforced HDPE Composites," ***ASME Journal of Tribology*****, 134**: article ID 041602

Peer-reviewed Conference Papers:

1. **S. Xu**, T. Liu, X.W. Tangpong, I. S. Akhatov, and W.H. Zhong, 2013, "Microcharacterization of Creep Behavior of Carbon Nanofiber Reinforced HDPE Nanocomposites using a Depth Sensing Method," ***Nanotech 2013 Conference Proceedings***, May 12-16, Washington, DC, USA
2. **S. Xu**, A.Akchurin, X.W. Tangpong, T. Liu, W. Wood and W.H. Zhong, 2012, "Comparison of Tribological Performances of High Density Polyethylene Enhanced with Carbon Nanofibers Under Dry Sliding Condition," ***Proceedings of ASME 2012 International Mechanical Engineering Congress & Exposition***, IMECE2012-86150, November 9-15, Houston, TX, USA
3. A. Akchurin, **S. Xu**, X.W. Tangpong, T.Liu, W. Wood and W.H Zhong, 2012, "Nanoscale Characterization of Wear Particles Produced from CNF- reinforced HDPE Composites," ***Proceedings of ASME 2012 International Mechanical Engineering Congress & Exposition***, IMECE2012-86149, November 9-15, Houston, TX, USA
4. **S. Xu**, A. Akchurin, T. Liu, W. Wood, X.W. Tangpong, I. S. Akhatov, and W.H Zhong, 2011,"Tribological Behavior of High Density Polyethylene Nanocomposites with Silane Treated Carbon Nanofibers", ***Proceedings of ASME 2011 International Mechanical Engineering Congress & Exposition***, IMECE2011-62701, November 11-17, Denver, CO, USA